بسم الله الرحمن الرحيم

# Numerical and Experimental Investigation of Shock wave Propagation in the Open Atmosphere

A thesis submitted to the department of Mechanical and Chemical Engineering (MCE) in partial fulfillment of the requirement for the degree of Master of Science in Mechanical Engineering


**SUBMITTED BY**

**Mohammad Monjurul Ehsan**
MSc. student no-101602

**Department of Mechanical and Chemical Engineering**

**Islamic University of Technology (IUT)**

**The Organization of Islamic Cooperation (OIC)**



**August, 2012**

**Recommendation of the Board of Examiners**

The thesis of title "NUMERICAL AND EXPERIMENTAL INVESTIGATION OF SHOCK WAVE PROPAGATION IN OPEN ATMOSPHERE" submitted by Mohammad Monjurul Ehsan, Student no-101602 of academic year 2011-2012 has been found as satisfactory and accepted on 15.03.2012 as partial fulfillment of the requirement for the degree of Master of Science in Mechanical Engineering.

_____ (Supervisor)

Dr. Mohammad Ali Jinnah
Associate Professor
Department of Mechanical and Chemical Engineering (MCE)
Islamic University of Technology (IUT)

_____ Member

Dr. Faisal Kader
Assistant Professor
Department of Mechanical and Chemical Engineering (MCE)
Islamic University of Technology (IUT)

_____ Member (Ex-Officio)

Prof. Dr. Md. Abdur Razzaq Akhanda
Head
Department of Mechanical and Chemical Engineering (MCE)
Islamic University of Technology (IUT)

Member (External)

_____

Prof. Dr. Mohammad Ali
Professor
Department of Mechanical Engineering
Bangladesh University of Engineering and Technology (BUET)

## Declaration

This is to certify that this thesis paper is a unique work on "Numerical and Experimental investigation of shock wave propagation in open atmosphere", None of its contents are copied or exactly taken from any other researches. The outcome of the research is done by us and neither of this thesis nor has any part thereof been submitted anywhere else for the award of any degree or any diploma.

Signature of the Candidate

_____

Mohammad Monjurul Ehsan
Student no-101602, Session- 2011-2012
Department of Mechanical and Chemical Engineering (MCE)
Islamic University of Technology (IUT)
Organization of Islamic Co-operation (OIC)
Board Bazar, Gazipur-1704
Bangladesh

**Acknowledgement**

I express my heartiest gratefulness to almighty Allah for His countless blessing, which enabled me to complete this thesis successfully. It is my pleasure to express thankful gratitude to my project supervisor Dr. Mohammad Ali Jinnah, Department Of Mechanical and Chemical Engineering, Islamic University of Technology (IUT) for his constant support, guidance, helpful suggestions and untired supervision at all stages of this research work. The supervisor had dedicated his valuable time, even at odd hours, which had ensured completion of this thesis work. I also express my sincere gratefulness to Dr. Md.Abdur Razzaq Akhanda. Head of the department, Mechanical and Chemical Engineering (MCE), IUT for providing us all sorts of support, encouragement and enthusiasms. Special thanks for my beloved parents whose love and inspiration kept me going during this project work and to the instructors, foreman and technicians of fluid mechanics lab of Mechanical and Chemical Engineering Department (MCE), Islamic University of Technology (IUT).I am highly indebted to the above-mentioned persons and without their encouragement, it would have been impossible to complete this dissertation.

# Abstract

Shock wave propagation in the open atmosphere has been investigated both numerically and experimentally. Three-dimensional numerical code has been used to solve the Euler equations for the upstream and downstream parameters during propagation in the open Atmosphere. It is observed that due to decay of the shock strength, all parameters (velocity, pressure and density) are decreased with increasing the travel time of the wave in the open Atmosphere. It is found from the numerical images that the propagation of the shock front in the open Atmosphere is spherical in shape. An experiment has been conducted by a horizontal shock tube to generate subsonic wave as well as supersonic shock wave by rupturing different types of diaphragm. The material properties of diaphragm are the major factor to generate shock wave in a shock tube. It is observed that the material properties like toughness and brittleness are the best properties in the present case. In this experiment, transparent Raksin sheet and used X-ray film earlier are used where X-ray film gives the better performance as compare to Raksin for better rupture. For measuring the wave speed in the open Atmosphere, a time measuring technique has been developed to measure the wave travel time in open Atmosphere and it is simple in use and accurate in measurement as compare to other complicated technique like wave visualization by High Speed Video camera. During wave propagation, the wave speed decreases with increasing the travel time in open Atmosphere. So decreasing the speed indicates that the decay of the wave strength is normal phenomena during propagation in the open Atmosphere. In the present study, both experimental and numerical techniques are applied successfully to determine the decay of the wave strength.

# Table of Contents

Recommendation of the Board of Examiners

Declaration

Acknowledgement

Abstract

**Chapter 1 INTRODUCTUION (1-3)**

**Chapter 2 LITERATURE REVIEW (4-13)**

2.1 Literature on shockwave propagation 4
2.2 Scope of the present work 12
2.3 Objectives of proposed work 13
2.4 Possible outcomes 13

**Chapter 3 THEORY OF WAVE PROPAGATION IN OPEN ATMOSPHERE (14-32)**

3.1 Introduction 14
3.2 Theory 16
3.3 Wave propagation phenomena 22
3.4 Summary 32

**Chapter 4 NUMERICAL SIMULATION ON WAVE PROPAGATION IN OPEN ATMOSPHERE (39-49)**

4.1 Introduction 39

4.2 Numerical Method 40

4.2.1 Governing equations 40

4.2.2 Numerical discretization and grid adaptation 41

4.3 Numerical Setup 43

4.3.1 Problem specifications 43

4.3.2 Boundary conditions 44

4.3.3 Grid convergence study 44

4.4 Results and Discussion 45

4.5 Summary 49

**Chapter 5 EXPERIMENTS ON WAVE PROPAGATION IN OPEN ATMOSPHERE (60-69)**

5.1 Introduction 60

5.2 Experimental Setup 62

5.3 Numerical Setup 65

5.3.1 Problem specifications 65

5.3.2 Boundary conditions 66

4.4 Results and Discussion 66

4.5 Summary 69

**Chapter 6 CONCLUSSIONS (82-84)**

**REFERENCES (85-89)**

**List of Publications**

## LIST OF FIGURES


| Figure No. | Title of the figure | Page No. |
|---|---|---|
| **Figure 3.1** | Steady flow in a tube with sudden small change in velocity, pressure and density. | **33** |
| **Figure 3.2** | Upstream and downstream parameters across shock wave. | **33** |
| **Figure 3.3** | Enthalpy-entropy relation across shock wave where point 'a' connects supersonic flow with subsonic flow. | **33** |
| **Figure 3.4** | Pressure curve P(t): the rise to peak pressure (P+) takes place in a few nanoseconds (ns). The peak pressures reach values of approx. 10 – 150MPa. The pulse lasts approx. 0.3 – 0.5 μs. The relatively low tensile wave component (P–), which is limited to approx. 10% of the peak pressure, is characteristic. | **34** |
| **Figure 3.5** | Schlieren image of the shock waves generated by an F-18 aircraft flying at Mach 1.4. The Mach cone generated by the head and tail shocks can be seen as well as the shocks generated by the leading and trailing edges of the wings. (NASA Dryden Flight Research Center). | **34** |
| **Figure 3.6** | Shock wave generation with expansion wave and compression wave. | **35** |
| **Figure 3.7** | Typical normal shock, oblique shock, and Mach wave pattern in supersonic flow past a blunt body where the curved line parallel to normal and oblique shock waves indicates the end of the velocity vectors. | **35** |
| **Figure 3.8** | The image of the shock wave in front of a blunt object in a wind tunnel during an experiment at NASA Ames Research Center. | **35** |
| **Figure 3.9** | The image of the shock wave in front of a bullet traveling through air at about 1.5 times the speed of sound. | **36** |
| **Figure 3.10** | Relative position of normal shock wave and oblique shock wave with respect to initial velocity. | **36** |
| **Figure 3.11** | Supersonic flow encounters a wedge and is uniformly deflected forming an oblique shock. | **36** |
| **Figure 3.12** | Normal shock wave reflection phenomena. | **37** |
| **Figure 3.13** | Flow Situation Before and After the Reflection of a Shock Wave from a Rigid Wall.Region 5 is behind the Reflected Shock Wave. | **37** |
| **Figure 3.14** | Shadowgraph of shock wave diffraction around a triangular obstacle taken in an air shock tube (Courtesy German-French Research Institute, St. Louis, ISL). | **37** |

| | | |
|---|---|---|
| **Figure 3.15** | CFD image of Shock wave diffraction emerging from a tube. | **38** |
| **Figure 3.16** | Shock wave diffraction over multiple cylinders. | **38** |
| **Figure 3.17** | Interaction of shock waves with obstacles (i) CFD image; (ii) Experimental shaded photograph. | **38** |
| **Figure 4.1** | (i) Three-dimensional cell with six faces; (ii) Each face addresses the center of two neighboring cells, *i* and *j*. | **51** |
| **Figure 4.2** | (i) Primary cell before adaptation where the center of the cell, cc is shown; (ii) Sequence of the eight cells after refinement of the primary cell. | **51** |
| **Figure 4.3** | Sectional view of half numerical domain of grid size 5x5x5 (*mm*) where 3D grid adaptation technique is shown. | **52** |
| **Figure 4.4** | Sectional view of half numerical domain of grid size 10x10x10 (*mm*) where 3D grid adaptation technique is shown. | **52** |
| **Figure 4.5** | 3D numerical domain where the grid size is 5x5x5 (*mm*). | **53** |
| **Figure 4.6** | 3D numerical domain where the grid size is 10x10x10 (*mm*). | **53** |
| **Figure 4.7** | Schematic layout of the shock tube and the relative position of the free space. | **54** |
| **Figure 4.8** | Shock wave position from the end section of the shock tube in the free space after the wave travelled time **(i)** $t$ = 35 $\mu sec$, **(ii)** $t$ = 96 $\mu sec$, **(iii)** $t$ = 121 $\mu sec$, **(iv)** $t$ = 190 $\mu sec$. | **54** |
| **Figure 4.9** | Longitudinal velocity, *U/c* profiles along the centerline of the free space using different grid sizes when the wave travelled time; **(i)** $t$ = 35 $\mu sec$, **(ii)** $t$ = 96 $\mu sec$, **(iii)** $t$ = 121 $\mu sec$, **(iv)** $t$ = 190 $\mu sec$. | **55** |
| **Figure 4.10** | Normalized pressure, $P/P_o$ profiles along the centerline of the free space using different grid sizes when the wave travelled time; **(i)** $t$ = 35 $\mu sec$, **(ii)** $t$ = 96 $\mu sec$, **(iii)** $t$ = 121 $\mu sec$, **(iv)** $t$ = 190 $\mu sec$. | **56** |
| **Figure 4.11** | Normalized density, $\rho/\rho_o$ profiles along the centerline of the free space using different grid sizes when the wave travelled time; **(i)** $t$ = 35 $\mu sec$, **(ii)** $t$ = 96 $\mu sec$, **(iii)** $t$ = 121 $\mu sec$, **(iv)** $t$ = 190 $\mu sec$. | **57** |
| **Figure 4.12** | Lateral velocity, *v/c* profiles along the centerline of the free space using different grid sizes when the wave travelled time; **(i)** $t$ = 35 $\mu sec$, **(ii)** $t$ = 96 $\mu sec$, **(iii)** $t$ = 121 $\mu sec$, **(iv)** $t$ = 190 $\mu sec$. | **58** |
| **Figure 4.13** | Lateral velocity, *w/c* profiles along the centerline of the free space using different grid sizes when the wave travelled time; **(i)** $t$ = 35 $\mu sec$, **(ii)** $t$ = 96 $\mu sec$, **(iii)** $t$ = 121 $\mu sec$, **(iv)** $t$ = 190 $\mu sec$. | **59** |
| **Figure 5.1** | Simple shock tube, constructed in Fluid Mechanics Lab on IUT where driver section and driven section are shown. | **70** |
| **Figure 5.2** | Post-shocked high speed air delivered from end section of the shock tube. | **70** |

| | | |
|---|---|---|
| **Figure 5.3** | Rupturing characteristics of different diaphragms of **(i)** Thick polythene; **(ii)** Raksin; **(iii)** X-ray film. | **72** |
| **Figure 5.4** | A typical diagram *x-t* diagram for the relative direction of the shock wave and expansion wave propagation after the rupture of diaphragm. | **72** |
| **Figure 5.5** | Circuit layout use to construct time measuring device. | **73** |
| **Figure 5.6** | A schematic illustration of the horizontal shock tube where the relative distances between different trigger points are given. | **73** |
| **Figure 5.7** | Schematic diagram of the Shock tube and the position of triggers | **74** |
| **Figure 5.8** | 2D numerical grids of the shock tube and the free space where solid boundaries are taken for shock tube and open boundaries are taken for free space. | **74** |
| **Figure 5.9** | Numerical results of the density contours at different locations of the shock front in the open Atmosphere for moderate shock propagation. | **75** |
| | (i) Near end section of the shock tube, $x = 0$ *cm*, density contours step 0.01. | **75** |
| | (ii) Shock front position at $x = 9.0$ *cm*, density contours step 0.01. | **75** |
| | (iii) Shock front position at x = 13.75 cm, density contours step 0.01. | **75** |
| | (iv) Shock front position at x = 18.5 mm, density contours step 0.01. | **75** |
| | (v) Shock front position at x = 23.5 mm, density contours step 0.01. | **76** |
| | (vi) Shock front position at x = 28.5 mm, density contours step 0.01. | **76** |
| | (vii) Shock front position at x = 33.5 mm, density contour step 0.01. | **76** |
| | (viii) Shock front position at x = 38.5 mm, density contour step 0.01. | **76** |
| **Figure 5.10** | Numerical results of the density fringes at different locations of the shock front in the open Atmosphere for moderate shock propagation. | **77** |
| | (i) Near end section of the shock tube, x = 0.0 cm, density fringes step 0.1. | **77** |
| | (ii) Shock front position at x = 9.0 cm density fringes step 0.1. | **77** |
| | (iii) Shock front position at x = 13.75 cm, density fringes step 0.1. | **77** |

| | | |
|---|---|---|
| | (iv) Shock front position at $x$ = 18.5 *cm*, density fringes step 0.1. | **77** |
| | (v) Shock front position at x = 23.5 cm, density fringes step 0.1. | **78** |
| | (vi) Shock front position at x = 28.5 cm, density fringes step 0.1. | **78** |
| | (vii) Shock front position at x = 33.5 cm, density fringes step 0.1. | **78** |
| | (viii) Shock front position at $x$ = 38.5 *cm*, density fringes step 0.1. | **78** |
| **Figure 5.11** | Captured frequency measured **e**xperimentally during the wave travels between different trigger points in the open Atmosphere (Here 1 sec = 3579540 pulses). | **79** |
| **Figure 5.12** | Experimental results of the average wave speed at different locations of the shock front in the open Atmosphere (Here rupture of Raksin diaphragm generates subsonic wave at the end of shock tube). | **79** |
| **Figure 5.13** | Captured frequency measured **e**xperimentally during the wave travels between different trigger points in the open Atmosphere (Here 1 sec = 3579540 pulses). | **80** |
| **Figure 5.14** | Experimental results of the average wave speed at different locations of the shock front in the open Atmosphere (Here rupture of X-ray film diaphragm generates supersonic wave at the end of shock tube). | **80** |
| **Figure 5.15** | Comparison between Experimental results and Numerical results of the percentage of decay of the wave propagation in the open Atmosphere (Here rupture of Raksin diaphragm generates subsonic wave at the end of shock tube). | **81** |
| **Figure 5.16** | Comparison between Experimental results and Numerical results of the percentage of decay of the wave propagation in the open Atmosphere. (Here rupture of X-ray film diaphragm generates supersonic wave at the end of shock tube). | **81** |

# Chapter 1

## Introduction

The investigation of wave propagation in the open atmosphere is one of the complex works. Experimental investigation is essential to improve the understanding of wave propagation with subsonic or supersonic speed in the open atmosphere. Some optical techniques can able to visualize the wave propagation and the location of the wave. High Speed Video camera is also used for the flow visualization to analyze the structure of the wave as well as to determine the wave speed. The application of some of these techniques to supersonic and hypersonic flows can be highly challenging due to the high velocity, high gradients and restricted optical access generally encountered. Widely used qualitative and semi-quantitative optical flow diagnostics are shadowgraph, schlieren, and interferometry. Schlieren visualizations of weak shock waves from common phenomena include loud trumpet notes, various impact phenomena that compress a bubble of air, bursting a toy balloon, popping a champagne cork, snapping a wooden stick, and snapping a wet towel. The balloon burst, snapping a ruler on a table, and snapping the towel and a leather belt all produced visible shock wave. Doig et al. [1] conducted experiment where direction-indicating color schlieren flow visualization was used to determine optically the general effectiveness of the methods. Multiple images were taken during a single tunnel run, which allowed, to some extent to the confirmation of the general steadiness of the flow. The light source used in the experiments had a flash duration of 200 $\mu s$, which was short enough to 'freeze' any large-scale motions in the flow but long enough to average out small-scale fluctuations such as free-stream turbulence and boundary layer effects on the test section windows.

Laser-based techniques such as laser Doppler anemometry and particle image velocimetry were well established for investigation of supersonic flows, but as yet their use in hypersonic flows had been limited. Other relevant measurement techniques include particle tracking velocimetry, Doppler global velocimetry, laser-two-focus anemometry, background oriented schlieren and laser induced fluorescence methods, molecular tagging velocimetry for velocity measurement and thermo-graphic phosphor thermometry for surface temperature measurement. Laser measurement techniques are becoming more commonly applied to many areas of thermo-fluids and heat transfer. An area of their application, which presents highly challenging requirements, is in the measurement of aerospace flows. In the shock wave research laboratory, Tohoku University Japan, the speed of projectile was measured by Shimadzu's HPV-1 High Speed Video Camera and the time elapsed from recording the first frame up to the $100^{th}$ frame was only about one ten-thousandth of a second. The ability to record dynamic images over short intervals is extremely significant.

In the study of metal-high explosive detonation wave interaction, by the pin technique, it is desirable to obtain time measurements to an accuracy of less than 1 $\mu sec$ over a total time interval of 5 $\mu sec$. Commercial instruments capable of a high degree of time resolution are not available and a special instrument is developed for this purpose. A cathode-ray oscilloscope, displaying deflection type event pulses, is converted into a precise time-measuring instrument by a calibrated zig-zag sweep. The record is obtained by single-shot photography of the cathode-ray tube sweep which is triggered by the event to be measured. Kobiera et al. [2] conducted an experiment on the shock wave propagation through the test section and the shock wave caused a disturbance of the droplets; this process was visualized by a schlieren system and recorded by a high-speed camera. The camera was synchronized with the igniter that was connected to the spark plug mounted in the driver section. The test section was also equipped with a pressure measurement system (two pressure sensors and amplifiers) whose signals were recorded on an oscilloscope. The sensors were located ahead of the test section windows and they could be used to measure the shock velocity and pressure waveform. Pianthong et al. [3] conducted an experiment with the use of the shadowgraph method, showing the projectile traveling inside and leaving the pressure relief section at a

velocity of about 1100 *m/s*. They also visualized the supersonic diesel fuel jets (velocity about 2 *km/s*) by the shadowgraph method.

In the present method, metal to metal touch switches generate pulses for triggering which open and close the gate to allow and stop the crystal frequency for counting. Using the number of pulse counted, the traveling time between the trigger points is measured for the subsonic or supersonic objects. Due to pressure difference across the wave, the trigger is operated by the pressure response to detect the wave position in the open atmosphere. This is one of the easier methods to measure the traveling time of the subsonic or supersonic wave between the two trigger points as compare to other methods. Though visualizations of the wave front or the pressure response from pressure transducers are the familiar methods to measure the strength of the wave or to identify its locations but the present technique is more reliable and accurate to measure the time. Normally the propagation time of the logic gates is not more than 20 nanoseconds, so the accuracy level of the measured time will be less than 0.006%.

# Chapter 2

# Literature review

## 2.1 Literature on Shock wave propagation

Both experimental and numerical investigations on shock wave propagation in the open atmosphere are an important feature due to its complexity to determine the propagation characteristics. Experimental realization of a shock wave generation in the shock tube and its propagation in the open Atmosphere in the laboratory is a difficult task due to generation of normal shock wave by the rupture of diaphragm properly in the shock tube and dangerous sound hazards in the open Atmosphere. Experimentally and numerically many researchers obtained many results on shock wave propagation inside test section but it was observed limited works on shock wave propagation in the open atmosphere. Shock wave propagation in the open Atmosphere is a direct effect of the Rankine-Hugoniot relations. The study of the shock wave propagation in the open Atmosphere is of fundamental importance in engineering applications. For designing aero-mechanism system such as transport aircraft of supersonic and hypersonic speed, the shock wave and its interaction effects with objects are the important phenomena. The shock interaction effects with objects are generally shown in aero-mechanism system and in combustion process as well as high-speed rotor flows.

The study of the interaction shock wave with objects began in the early 1950s with the development of linear theories. Ribner [4]-[6] investigated that how a shock wave was perturbed by an impinging single shear wave. The theory, later on called Ribner's theory, is, in fact, mostly based on the mode theory developed by Kovasznay [7] and extended to the shock problem by focusing mainly on the acoustic field generated by the interaction with the shock wave. Using his general theory of aerodynamic sound

generation, Lighthill [8] estimated the acoustic energy scattered from the interaction of turbulence with a shock wave. Analytical studies of shock-turbulence interaction (Ribner [4]; Moore [9]; Kerrebrock [10]) were performed using a linearized description of the interaction of plane disturbances interacting with a shock wave. These disturbances were represented as waves of vorticity, entropy, or sound (Kovasznay [7]) and these disturbances interacting with the shock wave generated the fluctuations downstream of the shock wave. Ribner [4] investigated the passage of a single vorticity wave through a plane shock and its modification, with simultaneous generation of a sound wave in a reference frame fixed on the shock wave. This analysis was later extended to study turbulence amplification due to a shock wave (Ribner [5]), the flux of acoustic energy emanating from the downstream side of the shock (Ribner [6]), and the one-dimensional power spectra of various fluctuations at downstream of the shock (Ribner [11]). Moore [9] analysed the flow field produced by oblique impingement of weak plane disturbances on a normal shock wave in a reference frame fixed on the mean upstream flow. Anyiwo and Bushnell [12] revisited the linear analysis to identify primary mechanisms of turbulence enhancement–amplification of the vorticity mode, generation of acoustic and entropy modes from the interaction, and turbulence 'pumping' by shock oscillations. The shock/turbulence interaction considerably modifies the fluid field by vorticity and entropy production and transport. Experimental investigation on from shock wave/boundary layer interaction indicates amplification in Reynolds stresses and turbulence intensities across the shock wave. The physics, however, of the phenomena associated with this amplification is not well understood. The first attempt to predict such turbulence amplification across the shock is attributed to Ribner [4]. His predictions were verified by experiments conducted by Sekundov [13] and Donsanjh and Weeks [14]. Several analytical and numerical studies of this phenomenon showed very similar turbulence enhancement. Chu and Kovazsnay [15] indicated that there are three fluctuating modes, which were coupled and were responsible for the turbulence amplification. Acoustic (fluctuating pressure and irrotational velocity mode), turbulence (fluctuating vorticity mode) and entropy (fluctuating temperature mode) are the three fluctuating modes which are nonlinearly coupled and the Rankine-Hugoniot jump conditions across the shock indicate that when any one of the three fluctuation modes is transferred across a shock wave, it not only

generates the other two fluctuation modes, but it may itself also be considerably amplified.

Wave motion can often be modeled as an essentially one-dimensional phenomenon. Wave fronts may certainly be curved, but, in many situations, they still behave as if locally planar with curvature playing only a secondary role. This local one-dimensionality is a clue to much of theoretical understanding of waves. Geometrical optics, for instance, treats high-frequency waves as if they had definite directions of propagation given by "rays." Nonlinear hyperbolic systems and shock waves are also best understood in nearly one-dimensional situations, where simple analytical models like the inviscid Burgers' equation or the Riemann problem and relatively simple experimental setups, such as shock-tubes, are often available. There are many situations, however, in which these one-dimensional models are insufficient. The best known example is the diffraction of light through a crystal or after hitting an obstacle, where the failure of ray theory introduced to the discovery of the wave-like character of light and, in a broader context, to quantum physics. Another is the intersection of two or more fronts, particularly for nonlinear waves. This includes phenomena arising in shock wave crossings, a shock's passage through the interface between two media and its reflection on a rigid wall. Yet another example is the focusing of concave fronts, where transverse effects destroy the nearly one-dimensional picture prior to focusing. All these situations abound in open problems and give rise to apparently paradoxical behaviors.

Most of the previous experimental works were performed on shock wave interaction with objects to determine the characteristics of shock wave/boundary-layer or free shear layer interactions. Another kind of research was performed in a shock tube to observe the pure interaction between a normal traveling shock wave reflected on the end wall of a shock tube and then interacting with the flow induced by the incident shock or by the wake of a perforated plate. All of these experiments showed a strong increase of density fluctuations through the shock but there were few data on the behavior of the velocity field. An experimental work was performed on the interaction of weak shocks ($M_s$=1.007, 1.03 and 1.1) with a random medium of density in homogeneity by Hesselink & Sturtevant [16]. They observed that the pressure histories of the distorted shock waves were both peaked and rounded and explained these

features in terms of the focusing/defocusing of the shock front due to in homogeneity of the medium. The Richtmyer-Meshkov instability (Richtmyer [17] and Meshkov [18]) provided an important example of the interaction of a shock wave and a material interface. This instability is observed when a shock wave passes along normal direction through a perturbed interface between two fluids of different densities. Experiments of such an instability showed that a single shock wave caused the perturbation's amplitude to grow linearly with time. However, interaction of the perturbation with a second shock stimulates the growth of the mixing zone of the gases. One interpretation of the experiments is that mixing is enhanced, i.e. the mixing zone between the two fluids grows by the interaction of the shock wave with the turbulent or random flow field left behind the first shock wave.

The investigation of wave propagation in the open atmosphere is one of the complex experimental works. Experimental investigation is essential to improve the understanding of wave propagation with subsonic or supersonic speed in the free atmosphere. Some optical techniques can able to visualize the propagation and the location of the wave. High speed camera is also used for the flow visualization to analysis the structure of the wave. The application of some of these techniques to supersonic and hypersonic flows can be highly challenging due to the high velocity, high gradients and restricted optical access generally encountered. Widely used qualitative and semi-quantitative optical flow diagnostics are shadowgraph, schlieren, and interferometry. Schlieren visualizations of weak shock waves from common phenomena include loud trumpet notes, various impact phenomena that compress a bubble of air, bursting a toy balloon, popping a champagne cork, snapping a wooden stick, and snapping awet towel. The balloon burst, snapping a ruler on a table, and snapping the towel and a leather belt all produced visible shock wave. Doig et al [19] conducted experiment where direction-indicating colour schlieren flow visualization was used to determine optically the general effectiveness of the methods. Multiple images were taken during a single tunnel run, which allowed, to some extent, confirmation of the general steadiness of the flow. The light source used in the experiments had a flash duration of 200 $\mu s$, which was short enough to 'freeze' any large-scale motions in the flow but long enough to average out small-scale fluctuations such as free-stream turbulence and boundary layer effects on the test section windows.

Craig [20] investigated effects of various area discontinuities and perforations in a tube on the attenuation of weak shock waves. Analytical models of shock wave attenuation over perforated walls were based mostly on the formulation of one-dimensional unsteady compressible flow theory such as those developed by Szumowski [21]. Sugimoto [22] proposed the installation of an array of Helmholtz resonators in high-speed train tunnels. The design was based on nonlinear acoustics. The resonators were found to be effective for preventing the transition from acoustic waves to a shock wave by rendering them dispersive. However, once a shock wave was formed the device failed to counteract it. Onodera and Takayama [23] experimentally determined a mass flow discharge coefficient through perforated walls by considering a two-dimensional flow field.

Takayama et al. [24] installed a porous material on the wall of a real high-speed train tunnel and found that the porous wall indeed decreased the overpressure and smeared the pressure gradient of weak shock waves generated by high-speed trains. However, the level of sonic boom suppressions obtained in the laboratory was not attained in the real train tunnel. Laser-based techniques such as laser Doppler anemometry and particle image velocimetry are well established for investigation of supersonic flows, but as yet their use in hypersonic flows has been limited. Other relevant measurement techniques include particle tracking velocimetry, Doppler global velocimetry, laser-two-focus anemometry, background oriented schlieren and laser induced fluorescence methods, molecular tagging velocimetry for velocity measurement and thermo-graphic phosphor thermometry for surface temperature measurement. Laser measurement techniques are becoming more commonly applied to many areas of thermo-fluids and heat transfer. An area of their application, which presents highly challenging requirements, is in the measurement of aerospace flows. In the shock wave research laboratory, Tohoku University Japan, the speed of projectile was measured by Shimadzu's HPV-1 High Speed Video Camera and the time elapsed from recording the first frame up to the $100^{th}$ frame was only about one ten-thousandth of a second. The ability to record dynamic images over short intervals is extremely significant. In the other technique, the projectile location can be determined by locating the trajectory of an incoming projectile. All supersonic projectiles are accompanied by a bow wave, often referred to as the "Mach Cone" which is virtually attached to the

projectile and which can be detected acoustically. When a distributed array of microphones detect the arrival of this cone, it is possible to calculate the position and angle of the trajectory from the microphone data.

The reflection of oblique shock waves is one of the fundamental research topics of shock wave dynamics. Regarding two-dimensional shock wave reflections, their patterns are classified, in general, as regular reflection or Mach reflection, depending on shock wave Mach numbers, wedge angles, and ratios of specific heats of test gases. A comprehensive classification of the reflection patterns in unsteady and quasi-stationary flows was given. Ben-Dor and Takayama [25] recently up-dated shock wave reflection phenomena in unsteady and quasi-stationary flows in the past. However, in previous studies, reflections over two-dimensional wedges were considered. It became a nearly established tradition in shock wave research that shock tube experiments were performed with straight wedges or two-dimensional concave and convex walls. Shock wave reflection studies were performed only for two-dimensional models and very rarely for three-dimensional cases. Critical transition angles of shock wave reflections over cones, whose configurations differ significantly from wedge shapes but two-dimensional analytical approaches are still valid, are more or less close to those over wedges. Timofeev et al. [26] numerically studied the reflection of planar shock waves over a 30◦ swept back cylinder placed on a shock tube bottom wall and successfully visualized, by using diffuse Double Exposure Holographic Interferometry and adopting the time interval of double exposures at a few microsecond, the spot on the cylinder at which reflected shock wave pattern changed from regular to Mach reflection. The process of focusing of a shock wave in a rarefied noble gas was investigated by a numerical solution of the corresponding two dimensional initial boundary value problem for the Boltzmann equation. They analyzed the development of the shock wave which reflects from a suitably shaped reflector, and studied influence of various factors, involved in the mathematical model of the problem, on the process of focusing. The interaction between a shock wave and a flame occurs frequently in many combustion systems. Due to the academic and practical values, many researchers are interested in shock–flame interactions. Some time ago, Markstein [27] experimentally studied the interactions of planar incident and reflected shock waves with a flame. Batley et al. [28] numerically studied a two-dimensional interaction process between a

planar incident or reflected shock wave and a cylindrical flame based on a one-step chemical reaction. The vorticity and flame distortion induced by baro-clinic effects were discussed. Khokhlov et al. [29] solved the two-dimensional reactive Navier–Stokes equations with a one-step chemical reaction and discussed the interaction of shock waves with a sinusoidal perturbed flame. Ju et al. [30] numerically simulated the interaction between a planar shock wave and a cylindrical flame based on detailed elementary chemical reactions. The mechanism for vorticity generation, flame distortion and effects of shock intensity on flame distortion were discussed in their work. Gelfand et al. [31], Bartenev et al. [32] performed experimental and numerical investigations of deflagration and detonation initiations induced by shock focusing in a reacted medium. The effect of reflector shapes on detonation initiation was discussed. However, few studies have been carried out on interactions between a focusing shock wave and a spherical flame. In 2008, Shinsuke Udagawa et al. [33] investigated Motion analysis of a diaphragmless driver section for a narrow channel shock tube. They set up a diaphragm less driver section as the first step towards developing a shock tube at micro-scale which had high experimental efficiency, independent of tube dimensions or the ratio of driver and driven pressure. They measured the operating time and the velocity of the fast opening valve. Additionally they introduced and calculated the differential equation, by using the Runge–Kutta–Gill method, to understand the motion of the fast opening valve. They finally achieved good agreement between experimental and calculated results for the velocity.

Flow separation in supersonic convergent–divergent nozzles had been the subject of several experimental and numerical studies in the past. Flow separation in supersonic nozzles is a basic fluid-dynamics phenomenon that occurs at a certain pressure ratio of chamber to ambient pressure, resulting in shock formation and shock/turbulent boundary layer interaction inside the nozzle. In 2009, Abdellah Hadjadj and Marcello Onofri investigated the nozzle flow separation [34]. A one-dimensional model for the numerical simulation of transport effects in small-scale, i.e., low Reynolds number, shock tubes is presented. The conservation equations have been integrated in the lateral directions and three-dimensional effects have been introduced as carefully controlled sources of mass, momentum and energy, into the axial conservation equations. Zeitoun and Burtschel [35] simulated the microscale shock tube flows at different values of

scaling parameter using unsteady 2D Navier–Stokes equations combined with boundary slip velocities and temperature jumps conditions in quite large Knudsen number regime where the rarefaction effects become non negligible. Their numerical results showed a strong attenuation of the shock wave strength with a decrease of the hot flow values along the tube that could lead to transformation of shock wave into the compression waves in smaller scaling parameters. The deviation of shock wave propagation in shock tubes from ideal behavior (e.g., shock attenuation), has been over the years an important issue in the study of shock tube flow. Trimpi and Cohen [36] used several simplifying assumptions to suggest a practical method for taking the boundary layer effects into account for a one-dimensional approach. Wall effects in shock tubes were well described by Emrich and wheeler [37] and good predictions on the deviation of shock strength from the ideal condition were obtained. Mirels [38] presented a method to compute the attenuation of shock waves by the method of characteristics involving simplifying assumptions. Roshko [39] studied the effects of boundary layer growth behind the shock wave and developed a similarity solution for flow duration in shock tubes. Good agreements with the experimental results in the low pressure shock tube were achieved. Details of the laminar boundary layer in shock tubes were studied by Mirels [40] and some correlation formulas were proposed. Boundary layers were also experimentally observed by Chen and Emrich [41] to study their structure in laminar and turbulent regions of the shock tube. In fact, low pressure shock tubes of usual sizes provided the satisfactory conditions necessary for the study of diffusion effects in shock tubes. The propagation of shock waves in small channels had been investigated experimentally and numerically by Sun et al. [42] in channels of 1–16 *mm* height at atmospheric pressure.

In the study of metal-high explosive detonation wave interaction, by the pin technique, it was desirable to obtain time measurements to an accuracy of less than 1 *μsec* over a total time interval of 5 *μsec*. Commercial instruments capable of a high degree of time resolution were not available and a special instrument was developed for this purpose. A cathode-ray oscilloscope, displaying deflection type event pulses, was converted into a precise time-measuring instrument by a calibrated zigzag sweep. The record was obtained by single-shot photography of the cathode-ray tube sweep which was triggered by the event to be measured. Kobiera et al [2] conducted experiment on

the shock wave propagation through the test section and the shock wave caused a disturbance of the droplets; this process was visualized by a schlieren system and recorded by a high-speed camera. The camera was synchronized with the igniters that were connected to the spark plug mounted in the driver section. The test section was also equipped with a pressure measurement system (two pressure sensors and amplifiers) whose signals were recorded on an oscilloscope. The sensors were located ahead of the test section windows, and was used to measure the shock velocity and pressure waveform. Pianthong et al [3] conducted experiment with the use of the shadowgraph method, showing the projectile travelling inside and leaving the pressure relief section at a velocity of about 1100 *m/s*. they also visualized the supersonic diesel fuel jets (velocity about 2 *km/s*) by the shadowgraph method.

## 2.2 Scope of the present work

(i) The study of the shock wave propagation in the open Atmosphere is of fundamental importance in engineering applications. For designing aero-mechanism system such as transport aircraft of supersonic and hypersonic speed, the shock wave and its interaction effects with objects are the important phenomena. The shock interaction effects with objects are generally shown in aero-mechanism system and in combustion process as well as high-speed rotor flows. So research on shock wave propagation in the open Atmosphere is necessary for design purposes.

(ii) The decay of shock strength during propagation in the open Atmosphere may be used to determine the shock interaction region.

(iii) The present research works may be used for mixing purpose in the chemical industry.

(iv) Numerical simulation may be focused on indoor laboratory research works avoiding some difficult experimental works on shock wave propagation.

(v) A technique for time measurement in microsecond level may be established to determine the wave propagation speed in the open Atmosphere.

## 2.3 Objectives of proposed work

(i) Development and construction of the horizontal shock tube for plane normal shock wave.

(ii) Determination of the decay of shock strength both by experimentally and numerically during shock wave propagation in the open Atmosphere.

(iii) Simulation of the decay phenomena using experimental and numerical results.

(iv) Visualization of the wave propagation numerically.

(v) Determination of the diaphragm rupturing effects to generate subsonic and supersonic wave in the shock tube and visualization of spherical wave propagation in Open Atmosphere by using numerical images.

## 2.4 Possible outcomes

(i) An innovative technique will be established to measure the wave strength in Open Atmosphere.

(ii) Device accuracy will be validated to measure wave propagation time in microsecond level by proper calibration experimentally.

(iii) It will be possible to explain the destruction phenomena by shock wave propagation in Open Atmosphere.

(iv) A comparison between experimental and numerical results will be conducted for numerical Code validation.

# Chapter 3

# Theory on Wave Propagation in Open Atmosphere

## 3.1 Introduction

In the present chapter, basic theory on wave propagation, especially shock wave propagation phenomena in open Atmosphere and its propagation characteristics have been introduced for the proper understanding on shock wave. Formation of wave in the flow field needs some techniques to apply disturbance in the flow. Diaphragm ruptured in a shock tube, Converging-diverging duct flow, Bomb blast in open atmosphere and Moving objects like Rocket, Gun fire etc. are the major sources of shock wave generation. Due to pressure rising in the pressure chamber, the diaphragm ruptures suddenly and the fluid starts to flow with high velocity through driven section of the shock tube. After few moments, it may reach supersonic flow which finally generates shock wave in the shock tube. In converging-diverging duct flow, as increasing the flow area at the diverging section, the flow velocity changes from subsonic to supersonic, generating shock wave at the outlet of the duct. In one-dimensional flow the only type of shock wave that can occur is a normal compression shock wave. For a converging-diverging flow, oblique shock waves must be taken into account as they occur at the exit and isentropic flow was shown to occur throughout a converging-diverging tube for a range of downstream pressures in which the flow is subsonic throughout and for downstream pressure, supersonic flow is observed through the diverging portion. So it is necessary to study the normal shock wave in the diverging portion with isentropic flow throughout the tube.

When a fluid at a supersonic speed approaches an airfoil (or a high-pressure region), the flow adjusts to the downstream conditions through a shock wave. Shock waves propagate faster than Mach waves and the flow speed changes abruptly from supersonic to less supersonic or subsonic across the wave. Similarly, other properties change discontinuously across the wave. A Mach wave is a shock wave of minimum strength. A normal shock is a plane shock normal to the direction of flow, and an oblique shock is inclined at an angle to the direction of flow. The velocity upstream of a shock wave is always supersonic. Downstream of an oblique shock, the velocity may be supersonic resulting in a strong shock, or subsonic resulting in a weak shock. The downstream velocity component normal to any shock wave is always subsonic. There is no change in the tangential velocity component across the shock.

A shock wave is a discontinuous surface that connects supersonic flow with subsonic flow. After a shock wave, flow velocity reduces, and pressure and temperature increase; entropy especially increases across a shock wave. Therefore, flow becomes non-equilibrium, and irreversible process occurs inside the shock layer. The thickness of a shock wave in neutral gas is of the order of the mean free path of the fluid particle. A shock wave also appears in magnetized plasma provided that when the plasma flow is parallel to the magnetic field, a shock wave appears if the governing equation for velocity potential is in hyperbolic type in relation with the Mach number and the Alfven number (The ratio of the speed of the Alfven wave to the speed of the fluid at a point in the fluid). When the flow is perpendicular to the magnetic field, the Maxwell stress, in addition to the pressure, plays a role in the shock wave in plasma. When the plasma temperature is so high, as the plasma becomes collision-free, another type of shock wave appears. In a collision-free shock wave, gyro-motions of electrons around the magnetic field lines cause the shock formation instead of collisions in a collision-dominant plasma or neutral gas. Regardless of a collision-dominant or collision-free shock wave, the fluid that passes through the shock wave is heated in addition to being compressed. In inertial confinement fusion, the fuel must be compressed.A shock wave, appearing in the process of implosion, compresses the fuel. The shock wave, however, heats the fuel more intensively, and it makes it difficult to compress the fuel further because high temperatures invite high pressure. Adiabatic compression of the fuel is the desired result during the implosion, without the formation of a shock wave.

Supersonic gas flows have a number of qualitative differences from subsonic flows. One important difference is a result of the principle that a small disturbance in a gas is propagated at the speed of sound. When a small change in pressure is produced by placing, for example, a body in a uniform supersonic flow, the influence of the disturbance cannot travel upstream. In the case of a steady supersonic flow along a wall with a sharp convex corner disturbances occur at the points on the line marking the corner. The influence of the disturbances is limited by the envelope of the Mach cones, which is a plane inclined to the direction of the flow. After passing through this plane, the flow turns and expands in the angular region formed by the set of plane disturbance fronts, or characteristics, which start at the corner. The flow stops turning when it becomes parallel to the direction of the wall after the corner. If, instead of forming a sharp corner, the two straight sections of the wall meet in a smooth curve, then the flow turns gradually and passes through a series of straight characteristics that start at each point of the curved section of the wall. In these two types of flows, which are known as Prandtl-Meyer flows, the gas parameters are constant along the straight characteristics. Waves in a gas that produce an increase in pressure propagate differently from waves that produce a decrease in pressure. A wave producing a pressure increase travels at a speed greater than the speed of sound. The thickness of such a wave can be very small—of the order of the molecular mean free path. In many theoretical studies the wave is replaced by a surface of discontinuity. Such a surface is known as a shock wave. When the gas passes through the shock wave, the velocity, pressure, density, and entropy of the gas abruptly change. In the case of a supersonic flow around a wedge, the translational flow along the side surface of the wedge is separated from the approaching flow by a plane shock wave that starts at the edge of the wedge. For wedge angles greater than a certain limiting angle, the shock wave is curved and is detached from the edge of the wedge. In this case, a zone of subsonic flow is located behind the shock wave. This situation is characteristic of supersonic flow around a blunt-nosed body.

## 3.2 Theory

The speed of a wave in a shock tube can be determined by the momentum equation and the continuity equation. The question is first raised whether a stationary small

change in velocity, pressure, and density can occur in a channel. By referring to **Fig. 3.1**, the continuity equation can be written as;

$$\rho VA = (\rho + d\rho)(V + dV)A$$

In which $A$ is the cross-sectional area of the tube. The equation can be reduced to

$$\rho\, dV + V d\rho = 0 \qquad \ldots \quad \ldots \quad \ldots \quad (3.1)$$

When the momentum equation is applied to the control volume within the dotted lines in **Fig. 3.1**, then

$$PA - (P + dP)A = \rho VA(V + dV - V)$$

Or $$dP = -\rho V dV \qquad \ldots \quad \ldots \quad \ldots \quad (3.2)$$

If $\rho\, dV$ is eliminated between the two equations (Eq. 3.1 and Eq. 3.2), then

$$V^2 = \frac{dP}{d\rho}$$

Hence a small disturbance or sudden change in conditions in steady flow can occur only when the particular velocity $V = \sqrt{dP/d\rho}$ exists in the shock tube. Now this problem can be converted to the unsteady flow of a small disturbance through still fluid by superimposing on the whole system and its surroundings the velocity $V$ to the left, since this in on way affects the dynamics of the system. This is called sound wave and the speed of the wave is called sound speed '$a$' in the medium. The disturbance from a point source would cause a spherical wave to emanate, but at some distance from the source the wave front would be essentially linear or one-dimensional. Large disturbance, e.g., diaphragm rupture in a shock tube, a bomb explosion, may travel faster than the speed of sound. The equation for speed of sound

$$a = \sqrt{\frac{dP}{d\rho}}$$

may be expressed in several useful forms.

Since the pressure and temperature changes due to passage of a sound wave are extremely small, the process is almost reversible. Also, the relatively rapid process of passage of the wave, together with the minute temperature changes, makes the process almost adiabatic. In the limit, the process may be considered to isentropic,

$$P\rho^{-k} = \text{Const}$$

$$\frac{dP}{d\rho} = \frac{kP}{\rho}$$

And $$a = \sqrt{\frac{kP}{\rho}}$$

Or from the perfect gas law, $P = \rho RT$ ,

$$a = \sqrt{kRT}$$

Which shows that the speed of sound in a perfect gas is a function of absolute temperature only. In flow of gas through a tube, the speed of sound generally changes from section to section as the temperature is changed by density changes and friction effects.

The Mach number has been defined as the ratio of velocity of a fluid to the local velocity of sound in the medium,

$$M = \frac{V}{a}$$

Squaring the Mach number produces $V^2 / a^2$, which may be interpreted as the ratio of kinetic energy of the fluid to its thermal energy, since kinetic energy is proportional to $V^2$ and thermal energy is proportional to $T$. The Mach number is a measure of the importance of compressibility.

Euler equation can be written as neglecting elevation changes,

$$VdV + \frac{dP}{\rho} = 0$$

When the analysis is restricted to isentropic flow, the equation of state may be written,

$$P = P_1 \rho_1^{-k} \rho^k$$

Differentiating and substituting for $dP$ in the Euler equation gives,

$$VdV + k\frac{P_1}{\rho_1^{k}}\rho^{k-2}d\rho = 0$$

Integrating yields,

$$\frac{V^2}{2} + \frac{k}{k-1}\frac{P_1}{\rho_1 k}\rho^{k-1} = \text{Const}$$

or $$\frac{V_1^2}{2}+\frac{k}{k-1}\frac{P_1}{\rho_1}=\frac{V_2^2}{2}+\frac{k}{k-1}\frac{P_2}{\rho_2}$$

This is the energy equation relating between the parameters of the upstream and downstream flow across a shock wave.

The shock wave occurs in supersonic flow and reduces the flow to subsonic flow, as proved in the following section. It has very little thickness, of the order of the molecular mean free path of the gas. The controlling equations for adiabatic flow are

Continuity: $$G=\frac{\dot{m}}{A}=\rho_1 V_1=\rho_2 V_2 \quad \ldots \quad \ldots \quad \ldots \quad (3.3)$$

Energy: $$\frac{V_1^2}{2}+h_1=\frac{V_2^2}{2}+h_2=h_0=\frac{V^2}{2}+\frac{k}{k-1}\frac{P}{\rho} \quad \ldots \quad \ldots \quad (3.4)$$

which are obtained for no change in elevation, no heat transfer, and no work done.
The enthalpy is,

$$h=u+\frac{P}{\rho}=c_p T$$

and $h_o$ is the value of stagnation enthalpy, i.e., its value in the reservoir or where the fluid is at rest. **Eq. 3.4** holds for real fluids and is valid both upstream and downstream from a shock wave. The momentum equation for a control volume between section 1 and 2 becomes;

$$(P_1-P_2)A=\rho_2 A V_2^2-\rho_1 A V_1^2$$

Or $$P_1+\rho_1 V_1^2=P_2+\rho_2 V_2^2 \quad \ldots \quad \ldots \quad \ldots \quad \ldots \quad (3.5)$$

For given upstream conditions $h_1$, $P_1$, $\rho_1$, $V_1$,the three equations (**Eq. 3.3-3.5**) are to be solved for $P_2$, $\rho_2$, $V_2$. The equation of state for a perfect gas is also available for use, $P=\rho RT$.

The value of $P_2$ is;

$$P_2=\frac{1}{k+1}\left[2\rho_1 V_1^2-(k-1)P_1\right] \quad \ldots \quad \ldots \quad \ldots \quad \ldots \quad (3.6)$$

Once $P_2$ is determined, by combination of the continuity and momentum equations;

$$P_1+\rho_1 V_1^2=P_2+\rho_1 V_1 V_2 \quad \ldots \quad \ldots \quad \ldots \quad \ldots \quad (3.7)$$

$V_2$ is readily obtained. Finally, $\rho_2$ is obtained from the continuity equation.

For given upstream conditions, $M_1$>1, the values of $P_2$, $\rho_2$, $V_2$ and $M_2 = V_2\sqrt{kP_2/\rho_2}$ exist and $M_2$<1. By eliminating $V_1$ and $V_2$ from **Eq. 3.3, 3.4** and **3.5**, the Rankine-Hugoniot equations (Toro [43]) are obtained:

$$\frac{P_2}{P1} = \frac{[(k+1)/(k-1)](\rho_2/\rho_1)-1}{[(k+1)/(k-1)]-\rho_2/\rho_1} \quad \ldots \quad \ldots \quad \ldots \quad (3.8)$$

and

$$\frac{\rho_2}{\rho 1} = \frac{1+[(k+1)/(k-1)](P_2/P_1)}{[(k+1)/(k-1)]+P_2/P_1} = \frac{V_1}{V_2} \quad \ldots \quad \ldots \quad \ldots \quad (3.9)$$

These equations, relating conditions on either side of the shock wave, take the place of the isentropic relation, $P\rho^{-k} = \text{const.}$

From Eq. 3.4, the energy equation,

$$\frac{V^2}{2} + \frac{k}{k-1}\frac{P}{\rho} = \frac{a^{*2}}{2} + \frac{a^{*2}}{k-1} = \frac{k+1}{k-1}\frac{a^{*2}}{2} \quad \ldots \quad \ldots \quad \ldots \quad (3.10)$$

Since the equation holds for all points in adiabatic flow without change in elevation, and $a^* = \sqrt{kP^*/\rho^*}$ is the velocity of sound. Dividing **Eq. 3.5** by **Eq. 3.3** gives,

$$V_1 - V_2 = \frac{P_2}{\rho_2 V_2} - \frac{P_1}{\rho_1 V_1}$$

and by eliminating $P_2/\rho_2$ and $P_1/\rho_1$ the **Eq. 3.10**, leads to

$$V_1 - V_2 = (V_1 - V_2)\left[\frac{a^{*2}(k+1)}{2kV_1V_2} + \frac{k-1}{2k}\right] \quad \ldots \quad \ldots \quad \ldots \quad (3.11)$$

Which satisfy by $V_1$=$V_2$ (no shock wave) or by

$$V_1V_2 = a^{*2} \quad \ldots \quad \ldots \quad \ldots \quad (3.12)$$

It may be written

$$\frac{V_1}{a^*}\frac{V_2}{a^*} = 1 \quad \ldots \quad \ldots \quad \ldots \quad (3.13)$$

When $V_1$ is greater than $a^*$, the upstream Mach number is greater than unity and $V_2$ is less than $a^*$, and so the final Mach number is less than unity, and vice versa. It is shown in the following section that the process can occur only from supersonic upstream to subsonic downstream.

Together **Eq. 3.6, 3.8,** and **3.9**, a relationship can be established between upstream flow conditions and downstream flow conditions of a normal shock wave in terms of $M_1$ and $k$. From **Eq. 3.6**;

$$\frac{P_2}{P_1} = \frac{1}{k+1}\left[\frac{2k\rho_1 V_1^{\,2}}{kP_1} - (k-1)\right] \qquad \ldots \quad \ldots \quad \ldots \quad (3.14)$$

Since $a_1^{\,2} = kP_1/\rho_1$ and $M_1 = V_1/a_1$, from **Eq. 3.14**,

$$\frac{P_2}{P_1} = \frac{2kM_1^{\,2} - (k-1)}{k+1}$$

Placing this value of $P_2/P_1$ in **Eq. 3.9** yields,

$$\frac{\rho_2}{\rho_1} = \frac{M_1^{\,2}(k+1)}{2 + M_1^{\,2}(k-1)}$$

These are the pressure and density ratios across the normal shock wave.

To examine more closely the nature of the flow change in the short distance across a shock wave, where the area may be considered constant, the continuity and energy equations are combined for steady, frictional, adiabatic flow. By considering upstream conditions fixed, that is, $P_1$, $\rho_1$, $V_1$, a plot may be made of all possible conditions. The most revealing plot is that of enthalpy against entropy, i.e., and *h-s* diagram, shown in **Fig. 3.3.**

The entropy equation for a perfect gas is,

$$s - s_1 = c_v \ln\left[\frac{P}{P1}\left(\frac{\rho_1}{\rho}\right)^k\right]$$

The energy equation for adiabatic flow with no change in elevation is

$$h_0 = h + \frac{V^2}{2}$$

and the continuity equation for no change in area is

$$G = \rho V$$

The equation of state linking h, P, and $\rho$, is

$$h = c_p T = \frac{c_p P}{R\rho}$$

By eliminating $P$, $\rho$, $V$ from the above four equations,

$$s = s_1 + c_v \ln\left[\frac{\rho_1^{\,k}}{P_1}\frac{R}{c_v}\left(\frac{\sqrt{2}}{G}\right)^{k-1}\right] + c_v \ln\left[h(h_0 - h)^{(k-1)/2}\right]$$

To find the conditions for maximum entropy, the above equation is differentiated with respect to h and *ds/dh* is set equal to zero. By indicating subscript values at the maximum entropy point is given by,

$$\frac{ds}{dh} = 0 = \frac{1}{h_a} - \frac{k-1}{2}\frac{1}{h_0 - h_a}$$

or $$h_a = \frac{2}{k+1}h_0$$

After substituting this into equation $h_0 = h + \frac{V^2}{2}$ to find $V_a$,

$$h_0 = \frac{k+1}{2}h_a = h_a + \frac{V_a^{\,2}}{2}$$

and $$V_a^{\,2} = (k-1)h_a = (k-1)c_p T_a = (k-1)\frac{kR}{k-1}T_a = kRT_a = c_a^{\,2}$$

Hence the maximum entropy at point *a* is for $M$=1, or sonic conditions. For $h>h_a$ the flow is subsonic, and for $h<h_a$ the flow is supersonic.

## 3.3 Wave propagation phenomena

Shock waves appear in the atmosphere when explosive events occur, such as when explosive material detonates, when lightning strokes occur or when airplanes break the sound barrier. Shock waves are acoustic waves that are characterized by high pressure amplitudes and a steep increase in pressure in comparison to the ambient pressure, shown in **Fig. 3.4**. In the atmosphere, shock waves can be heard directly as a very loud sound. They can transmit energy from the place of generation to distant areas and may cause window panes to shatter.

An audible sound wave generated by an object that moves faster than the speed of sound (supersonic object). The sonic boom forms because the air is pushed away faster than the air molecules can move. The displaced air becomes highly compressed and creates a very strong sound wave, referred to as a compression head shock or bow shock. At the back of the supersonic object the air has to fill the void left as the object moves forward; in this case, the gas becomes rarefied and a rare fractional tail shock develops. These shock waves are the main components of a sonic boom, and they are

generated the entire time when an object flies faster than the speed of sound, not just when it breaks the sonic barrier. Sonic booms may be natural or generated by human activity. A natural sonic boom is thunder, created when lightening ionizes air, which expands supersonically. Meteors can create sonic booms if they enter the atmosphere at supersonic speeds. Human sources of sonic booms include aircraft, rockets, and the space shuttle during reentry, and bullets. Sonic booms are commonly associated with supersonic aircraft. The shock waves associated with sonic booms propagate away from the aircraft in a unique fashion. These waves form a cone, called the Mach cone, that is dragged behind the aircraft. **Figure 3.5** shows the outline of the Mach cone generated by an F-18 fighter aircraft flying at Mach 1.4. The schlieren photographic technique was used to display the sonic boom, which is normally invisible. The half-angle of the cone is determined solely by the Mach number of the aircraft, $\theta = \arctan(1/M)$, 36° for $M = 1.4$. The shock waves travel along rays that are perpendicular to the Mach cone as shown in **Fig. 3.5**. As the Mach number increases, $\theta$ becomes smaller and the sound travels almost directly downward.

In supersonic flow, expansion waves occur when bodies begin to narrow, making more space available which is shown in **Fig. 3.6**. In passing through an expansion wave, air velocity increases, while temperature and pressure reduce. A simple wave or progressive disturbance in the isentropic flow of a compressible fluid is such that the pressure and density of a fluid particle decrease on crossing the wave in the direction of its motion. It is the opposite of a compression wave, also called a rarefaction wave.

In a two-dimensional supersonic flow around a blunt body as shown in **Fig. 3.7 and Fig. 3.8**, a normal shock is formed directly in front of the body, and extends around the body as a curved oblique shock. At a sufficient distance away, the flow field is unaffected by the presence of the body, and no discontinuity in velocity occurs. The shock then reduces to a Mach wave. Similarly when a bullet is travelled through air with a velocity at about 1.5 times the speed of sound, a normal shock is formed directly in front of the bullet as shown in **Fig. 3.9**, and extends around the body as a curved oblique shock.

In the case of a normal shock wave, the velocities both ahead (i.e. upstream) of the shock and after (i.e. downstream) of the shock are at right angles to the shock wave. In the case of an oblique shock wave there is a change in flow direction across the shock.

A complete shock wave may be effectively normal in part of the flow, curved in other parts of the flow and effectively oblique in other parts of the flow as shown in **Fig. 3.10.** Normal shock waves occur, for example, in the intakes to the engines in some supersonic aircraft, in the exhaust system of reciprocating engines, in long distance gas pipe-lines and in mine shafts as a result of the use of explosives. When a normal shock wave occurs, for example, in a steady flow through duct, it can be stationary with respect to the coordinate system which is fixed relative to the walls of the duct. Such a shock wave is called a stationary shock wave since it is not moving relative to the coordinate system used. On the other hand, when a sudden disturbance occurs in a flow, such as, for example, the sudden closing of a valve in a pipe-line or an explosive release of energy at a point in a duct, a normal shock wave can be generated which is moving relative to the duct walls.

As an object moves through a gas, the gas molecules are deflected around the object. If the speed of the object is much less than the speed of sound of the gas; the density of the gas remains constant and the flow of gas can be described by conservation of momentum and energy equations. As the speed of the object increases towards the speed of sound, it must consider compressibility effects on the gas. The density of the gas varies locally as the gas is compressed by the object. For compressible flows with little or small flow turning, the flow process is reversible and the entropy is constant. The changes in flow properties are then given by the isentropic relations. But when an object moves faster than the speed of sound, and there is an abrupt decrease in the flow area, the flow process is irreversible and the entropy increases. Shock waves are generated which are very small regions in the gas where the gas properties change by a large amount. Across a shock wave, the static pressure, temperature, and gas density increases almost instantaneously. Because a shock wave does no work, and there is no heat addition, the total enthalpy and the total temperature are constant. But because the flow is non-isentropic, the total pressure downstream of the shock is always less than the total pressure upstream of the shock; there is a loss of total pressure associated with a shock wave. Because total pressure changes across the shock, we cannot use the usual (incompressible) form of Bernoulli's equation across the shock. The Mach number and speed of the flow also decrease across a shock wave. If the shock wave is perpendicular to the flow direction it is called a normal shock.

A wave formed in front of a body when it is moving at the speed of sound. The waves do not move ahead of the body; they bunch up and form a Mach wave. If a Mach wave is at right angles to the direction of movement of the body, the wave is called a normal Mach wave. The air passing through a normal shock wave slows down to a subsonic speed while its pressure rises.

An Oblique Shock is a sharp edged shock wave that is formed when supersonic flow is turned on itself. These shocks are weaker than Normal Shocks, and although the temperature, pressure, density, and air stream velocity are reduced across the shock similar to the Normal Shock, the air stream behind the shock is not necessarily subsonic. The Mach number behind the Oblique shock is calculated from the upstream Mach number, defined by the angle at which the flow is tuned. **Figure 3.11** shows a typical oblique shock formed by a sharp angle.

An oblique shock wave, unlike a normal shock, is inclined with respect to the incident upstream flow direction. It will occur when a supersonic flow encounters a corner that effectively turns the flow into itself and compresses. The upstream streamlines are uniformly deflected after the shock wave. The most common way to produce an oblique shock wave is to place a wedge into supersonic compressible flow. Similar to a normal shock wave, the oblique shock wave consists of a very thin region across which nearly discontinuous changes in the thermodynamic properties of a gas occur. While the upstream and downstream flow directions are unchanged across a normal shock, they are different for flow across an oblique shock wave. It is always possible to convert an oblique shock into a normal shock by a Galilean transformation.

For a given Mach number, $M_1$, and corner angle, $\theta$, the oblique shock angle, $\beta$, and the downstream Mach number, $M_2$, can be calculated. $M_2$ is always less than $M_1$. Unlike after a normal shock, $M_2$ can still be supersonic (weak shock wave) or subsonic (strong shock wave). Nature tends to focus on weak solution. Discontinuous changes also occur in the pressure, density and temperature, which all rise downstream of the oblique shock wave.

Using the continuity equation and the fact that the tangential velocity component does not change across the shock, trigonometric relations eventually lead to the $\theta$-$\beta$-$M$ equation which shows $\theta$ as a function of $M_1$ and $\beta$.

$$\tan\theta = 2\cot\beta\frac{M_1^2\sin^2\beta - 1}{M_1^2(\gamma + \cos 2\beta) + 2}$$

It is more intuitive to want to solve for $\beta$ as a function of $M_1$ and $\theta$, but this approach is more complicated, the results of which are often contained in tables or calculated through an applet. Here is a way to calculate $\beta$ knowing $\theta$ and $M_1$.First define $\lambda$:

$$\lambda = \sqrt{(M_1^2 - 1)^2 - 3(1 + \frac{\gamma - 1}{2}M_1^2)(1 + \frac{\gamma + 1}{2}M_1^2)\tan^2\theta}$$

Then define $\chi$:

$$\chi = \frac{(M_1^2 - 1)^3 - 9(1 + \frac{\gamma-1}{2}M_1^2)(1 + \frac{\gamma-1}{2}M_1^2 + \frac{\gamma+1}{4}M_1^4)\tan^2\theta}{\lambda^3}$$

Finally $\beta$ is given by the relation:

$$\tan\beta = \frac{M_1^2 - 1 + 2\lambda\cos(\frac{4\pi\delta + \arccos(\chi)}{3})}{3(1 + \frac{\gamma-1}{2}M_1^2)\tan\theta}$$

where $\delta$=0 corresponds to the strong shock solution and $\delta$=1 to the weak one. Within the $\theta$-$\beta$-$M$ equation, a maximum corner angle, $\theta_{MAX}$, exists for any upstream Mach number. When $\theta > \theta_{MAX}$, the oblique shock wave is no longer attached to the corner and is replaced by a detached bow shock. A $\theta$-$\beta$-$M$ diagram, common in most compressible flow textbooks, shows a series of curves that will indicate $\theta_{MAX}$ for each Mach number. The $\theta$-$\beta$-$M$ relationship will produce two $\beta$ angles for a given $\theta$ and $M_1$, with the larger angle called a strong shock and the smaller called a weak shock. The weak shock is almost always seen experimentally. The rise in pressure, density, and temperature after an oblique shock can be calculated as follows:

$$\frac{p_2}{p_1} = 1 + \frac{2\gamma}{\gamma+1}(M_1^2 \sin^2\beta - 1)$$

$$\frac{\rho_2}{\rho_1} = \frac{(\gamma+1)M_1^2 \sin^2\beta}{(\gamma-1)M_1^2 \sin^2\beta + 2}$$

$$\frac{T_2}{T_1} = \frac{p_2}{p_1}\frac{\rho_1}{\rho_2}.$$

$M_2$ is solved for as follows:

$$M_2 = \frac{1}{\sin(\beta-\theta)}\sqrt{\frac{1+\frac{\gamma-1}{2}M_1^2 \sin^2\beta}{\gamma M_1^2 \sin^2\beta - \frac{\gamma-1}{2}}}.$$

As the Mach number of the upstream flow becomes hypersonic, the equations for the pressure, density, and temperature after the oblique shock wave reach a mathematical limit. The pressure and density ratios can then be expressed as:

$$\frac{p_2}{p_1} \approx \frac{2\gamma}{\gamma+1}M_1^2 \sin^2\beta$$
$$\frac{\rho_2}{\rho_1} \approx \frac{\gamma+1}{\gamma-1}.$$

For a perfect atmospheric gas approximation using $\gamma$ = 1.4, the hypersonic limit for the density ratio is 6. However, hypersonic post-shock dissociation of $O_2$ and $N_2$ into $O$ and $N$ lowers $\gamma$, allowing for higher density ratios in nature. The hypersonic temperature ratio is:

$$\frac{T_2}{T_1} \approx \frac{2\gamma(\gamma-1)}{(\gamma+1)^2}M_1^2 \sin^2\beta.$$

Oblique shock waves are used predominantly in engineering applications when compared with normal shock waves. This can be attributed to the fact that using one or a combination of oblique shock waves result in more favorable post-shock conditions (lower post-shock temperature, etc.) when compared to utilizing a single normal shock. An example of this technique can be seen in the design of supersonic aircraft engine

inlets, which are wedge-shaped to compress air flow into the combustion chamber while minimizing thermodynamic losses. Early supersonic aircraft jet engine inlets were designed using compression from a single normal shock, but this approach caps the maximum achievable Mach number to roughly 1.6. The wedge-shaped inlets are clearly visible on the sides of the F-14 Tomcat, which has a maximum speed of Mach 2.34. Many supersonic aircraft wings are designed around a thin diamond shape. Placing a diamond-shaped object at an angle of attack relative to the supersonic flow streamlines will result in two oblique shocks propagating from the front tip over the top and bottom of the wing, with Prandtl-Meyer expansion fans created at the two corners of the diamond closest to the front tip. When correctly designed, this generates lift.

When an object moves faster than the speed of sound, and there is an abrupt decrease in the flow area, shock waves are generated. Shock waves are very thin regions in the gas where the gas properties change by a large amount. In many flow problems multiple shocks are present. The shocks may intersect with each other and with the surfaces generating them. On this we present the physics which govern the reflection of a shock wave from a solid wall. When a free field blast wave runs into an object like a building, the wave will be reflected. **Figure 3.12** shows how a shock wave is reflected off a building. Due to reflection and diffraction, the wave loading on the walls and the roof will differ. The maximum loading will be on the wall facing the explosion. At this wall the shock wave will be reflected and the pressure will typically increase by a factor of 2.

When the shock wave propagates in a free field, the gas behind the shock wave will have a velocity in the same direction as the wave propagates. When the shock wave hits the wall, the gas must stop and the dynamic pressure is transformed to pressure. This is in principle why the pressure increases due to blast wave reflection.

The equations of reflected shock waves do not readily give solutions for the physical parameters behind the reflected shock in terms of the initial conditions in the tube. It is more convenient and perhaps more illustrative to derive the pressure, density, and temperature for the reflected shock in terms of the conditions in the incident one. From the equations derived, these properties may then be related to the initial conditions by way of the Mach number or speed of the incident shock. When the

normal shock front $S_I$, as shown in **Fig. 3.13**, traveling at the velocity $U_s$ relative to the tube, hits the end wall, it is reflected as the normal shock front $S_R$ which travels back into region (2) with a diminished speed $U_R$. The gas flows into this front with a relative velocity $V_{R_2}$, where $V_{R_2} = U_R + U_2$. Since after a normal reflection the particle velocity relative to the wall must be zero ($U_5 = 0$), the gas gives up the whole of its kinetic energy on passing through the front $S_R$ into the region of the reflected normal shock, thus increasing the properties of state of the gas in this region, above those in the incident region. The reflected shock thus can be envisaged as an extending column which advances out from the end wall of the tube and contains a static gas with high temperature, density, and pressure. A comprehensive classification of the reflection patterns in unsteady and quasi-stationary flows was given [25]. Ben-Dor [44] recently up-dated shock wave reflection phenomena in unsteady and quasi-stationary flows in the past.

Referring to **Figure 3.13**, the flow velocities relative to the reflected normal shock front may be written as:

$$V_{R_5} = U_R$$

$$V_{R_2} = U_R + U_2$$

Thus the Mach number of the gas ahead of the reflected shock is defined by:

$$M_{R_2} = \frac{V_{R_2}}{a_2}$$

NOTE: $M_{R_2} \neq M_R$

Writing the conservation of mass for the flow through the reflected wave we have:

$$\rho_2 V_{R_2} = \rho_5 V_{R_5}$$

Substitution of Equations

$$\rho_2 (U_R + U_2) = \rho_5 U_R$$

Which can be rewritten in the form:

$$U_2 = (U_R + U_2)\left[1 - \frac{\rho_2}{\rho_5}\right]$$

Multiplying and dividing the right hand side of Equation by $a_2$ and making use of the definition of $M_{R_2}$ we can further write that:

$$U_2 = a_2 M_{R_2}\left[1-\frac{\rho_2}{\rho_5}\right]$$

$\rho_2/\rho_5$ may be found by relating reflected shock to Equation, i.e.:

$$\frac{\rho_2}{\rho_5} = \frac{(\gamma-1)M_{R_2}^2+2}{(\gamma+1)M_{R_2}^2}$$

Finally the important relation that:

$$U_2 = \frac{2a_2}{\gamma+1}\left[M_{R_2}-\frac{1}{M_{R_2}}\right] = \frac{2a_1}{\gamma+1}\left[M_s-\frac{1}{M_s}\right]$$

Using the relation that $a^2 = \gamma RT$ and the equation of state, we can write that:

$$\left(\frac{a_2}{a_1}\right)^2 = \frac{p_2}{p_1}\frac{\rho_1}{\rho_2} \qquad \left(\frac{a_2}{a_1}\right)^2 = \frac{p_2}{p_1}\left[1+\frac{\gamma-1}{\gamma+1}\frac{p_2}{p_1}\right]\left[\frac{\gamma-1}{\gamma+1}+\frac{p_2}{p_1}\right]^{-1}$$

From the normal shock relations we had:

$$\frac{p_2}{p_1} = \frac{2\gamma M_s^2-(\gamma-1)}{\gamma+1}$$

and relating this to the reflected shock we have:

$$\frac{p_5}{p_2} = \frac{2\gamma M_{R_2}^2-(\gamma-1)}{\gamma+1}$$

Solving Equations for $p_5 / p_2$ gives:

$$\frac{p_5}{p_2} = \frac{\frac{\gamma+1}{\gamma-1} + 2 - \frac{p_1}{p_2}}{1 + \frac{\gamma+1}{\gamma-1}\frac{p_1}{p_2}}$$

The temperature ratio is found by using the equation of state to obtain:

$$\frac{\mathrm{T}_5}{\mathrm{T}_2} = \frac{p_5}{p_2}\frac{\rho_2}{\rho_5}$$

The final the result is:

$$\frac{p_5}{p_1} = \left[\frac{2\gamma M_s^2 - (\gamma-1)}{\gamma+1}\right]\left[\frac{(3\gamma-1)M_s^2 - 2(\gamma-1)}{(\gamma-1)M_s^2 + 2}\right],$$

$$\frac{T_5}{T_1} = \frac{\left(2(\gamma-1)M_s^2 + (3-\gamma)\right)\left((3\gamma-1)M_s^2 - 2(\gamma-1)\right)}{(\gamma+1)^2 M_s^2}.$$

Diffraction refers to various phenomena which occur when a wave encounters an obstacle. Italian scientist Francesco Maria Grimaldi coined the word "diffraction" and was the first to record accurate observations of the phenomenon in 1665. **Figure 3.14** shows shock wave diffraction around a triangular obstacle taken in an air shock tube. In classical physics, the diffraction phenomenon is described as the apparent bending of waves around small obstacles and the spreading out of waves past small openings. Similar effects occur when light waves travel through a medium with a varying refractive index or a sound wave through one with varying acoustic impedance. Diffraction occurs with all waves, including sound waves, water waves, and electromagnetic waves such as visible light, x-rays and radio waves. As physical objects have wave-like properties (at the atomic level), diffraction also occurs with matter and can be studied according to the principles of quantum mechanics.

The image, shown in **Fig. 3.15** is a CFD-generated shadowgraph of a shock wave emerging from a tube. The mouth of the tube is seen at the left of the image. The shock has already left the tube and has reflected from a rigid wall at the right of the picture. There also appears to be reflections from rigid walls at the top and bottom of the image.

One of the most spectacular features of the flow is the vortex ring which has just collided with the reflected shock wave.

The image, shown in **Fig. 3.16,** is an example of the diffraction of a shock wave over two cylinders. The initial shock Mach number (the Mach number immediately behind the shock in a frame moving with the shock) is 3. Evidence of the intrinsic nonlinearity is seen in the significant distortion of the diffracted fronts between the cylinders. A second point of interest is the flow in the region where the diffracted fronts meet (approximately halfway between the cylinders); these fronts resemble the patterns generated by focusing shock waves.

**Figure 3.17 (i)** represents the computation results for the interaction of shock waves with obstacles. This class of flows is a relatively easy one to explore with the help of experimental optic methods and is traditionally considered to be a reliable method for testing the efficiency of the computational approaches. Here is the comparison of the shaded photograph as shown in **Fig. 3.17 (ii)** and the numerical simulation results for the process of the propagation of a blast wave through a series of obstructions. Shaded photographs present information not about the density distribution itself but about fracture layout of its distribution, and, thus, it makes sense to compare experimentally obtained data and calculations of absolute density derivatives.

In the present research works, metal to metal touch switches generate pulses for triggering which open and close the gate to allow and stop the crystal frequency for counting. The counted frequency is used later to measure the travel time between two trigger points without taking any photographic visualization. In the shock wave research laboratory, Tohoku University Japan, the speed of projectile was measured with photographic visualization by Shimadzu's (Takayama et al. [24]) HPV-1 High Speed Video Camera and the time elapsed from recording the first frame up to the $100^{th}$ frame was only about one ten-thousandth of a second. The ability to record dynamic images over short intervals is extremely significant. Pianthong et al **[3]** conducted experiment with the use of the shadowgraph method, showing the projectile travelling inside and leaving the pressure relief section at a velocity of about 1100 *m/s*. they also visualized the supersonic diesel fuel jets (velocity about 2 *km/s*) by the shadowgraph method.

## 3.4 Summary

In this thesis, some basic theory on shock wave propagation in the open atmosphere has been described to understand properly the shock wave physics. Shock wave is the contact layer of supersonic and subsonic flow. Due to flow discontinuous along the shock axis, it must divide upstream and downstream flow conditions. The relationship between upstream and downstream flow conditions indicates the shock wave present in that flow fields. The established equations between upstream and downstream conditions are the Rankine-Hugoniot equations which are used as shock capturing techniques for computational works. In the present chapter, aside shock theory, some shock wave propagation phenomena are also described which finally clarify the basic shock theory.

# List of Figures

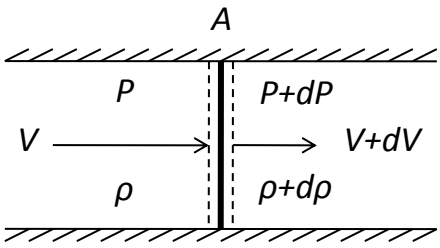


**Figure 3.1:** Steady flow in a tube with sudden small change in velocity, pressure and density.

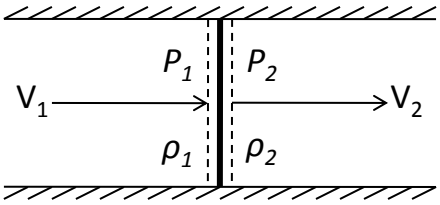


**Figure 3.2:** Upstream and downstream parameters across shock wave.

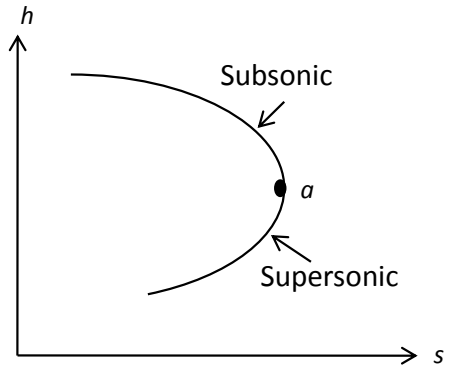


**Figure 3.3:** Enthalpy-entropy relation across shock wave where point 'a' connects supersonic flow with subsonic flow.

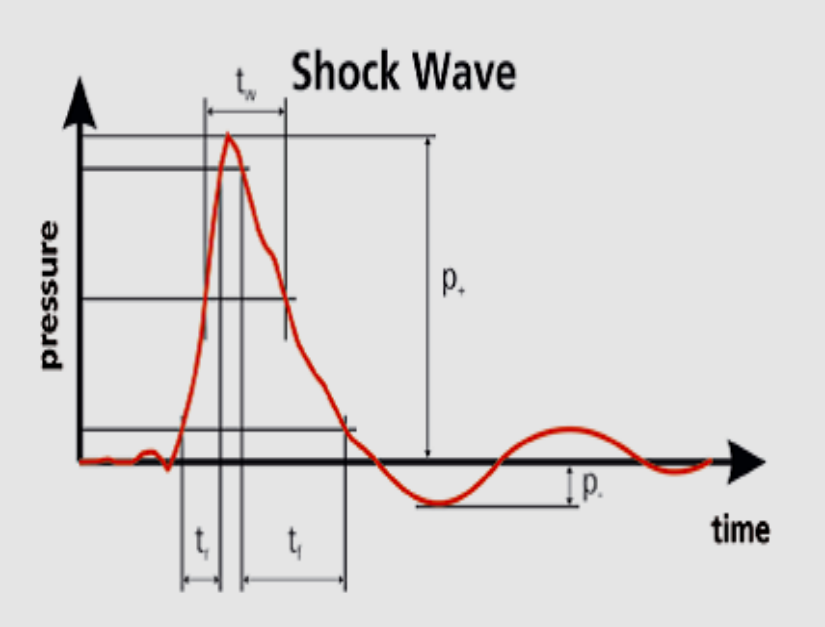


**Figure 3.4:** Pressure curve *P(t)*: the rise to peak pressure (*P*+) takes place in a few nanoseconds (*ns*). The peak pressures reach values of approx. 10 – 150 *MPa*. The pulse lasts approx. 0.3 – 0.5 $\mu s$. The relatively low tensile wave component (*P*–), which is limited to approx. 10% of the peak pressure, is characteristic.

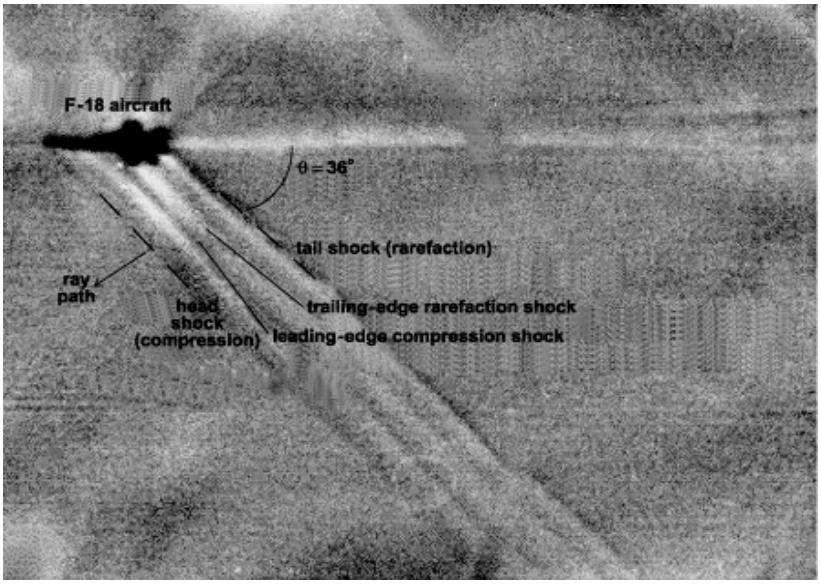


**Figure 3.5:** Schlieren image of the shock waves generated by an F-18 aircraft flying at Mach 1.4. The Mach cone generated by the head and tail shocks can be seen as well as the shocks generated by the leading and trailing edges of the wings. (NASA Dryden Flight Research Center).

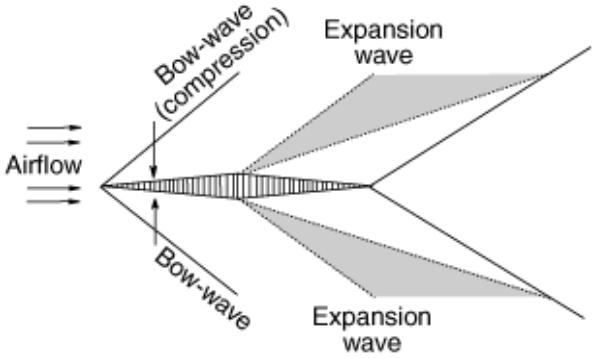


**Figure 3.6:** Shock wave generation with expansion wave and compression wave.

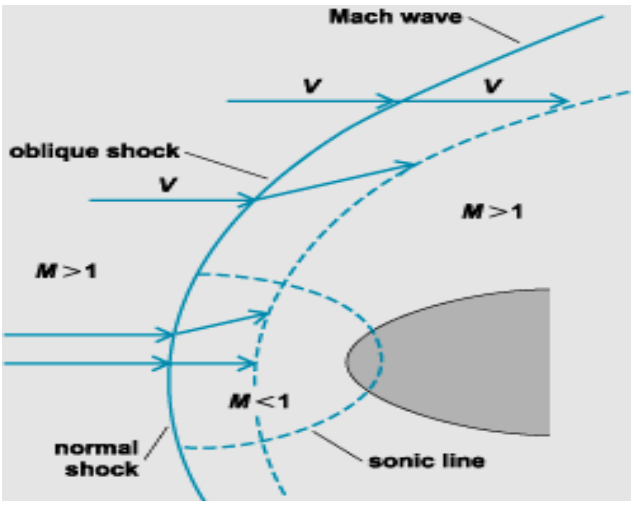


**Figure 3.7:** Typical normal shock, oblique shock, and Mach wave pattern in supersonic flow past a blunt body where the curved line parallel to normal and oblique shock waves indicates the end of the velocity vectors.

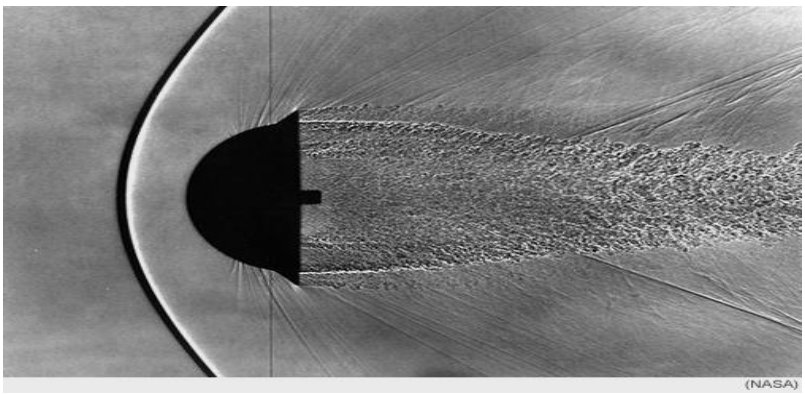


**Figure 3.8:** The image of the shock wave in front of a blunt object in a wind tunnel during an experiment at NASA Ames Research Center.

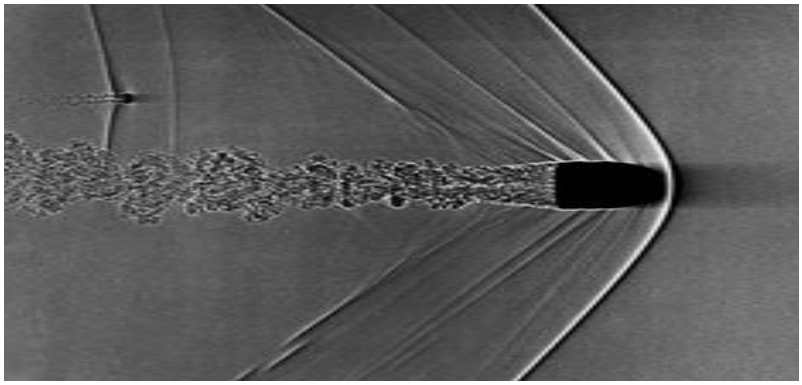

**Figure 3.9:** The image of the shock wave in front of a bullet traveling through air at about 1.5 times the speed of sound.

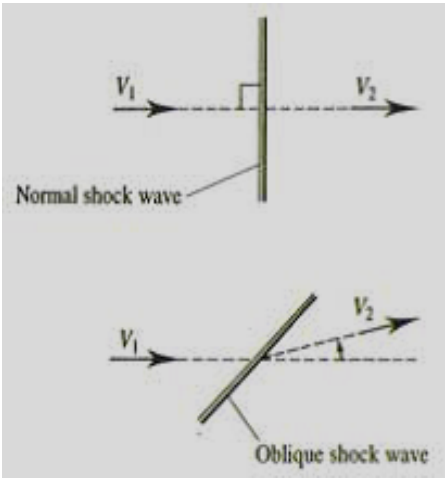


**Figure 3.10:** Relative position of normal shock wave and oblique shock wave with respect to initial velocity.

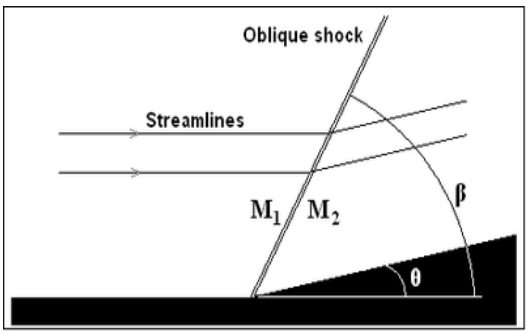


**Figure 3.11:** Supersonic flow encounters a wedge and is uniformly deflected forming an oblique shock.

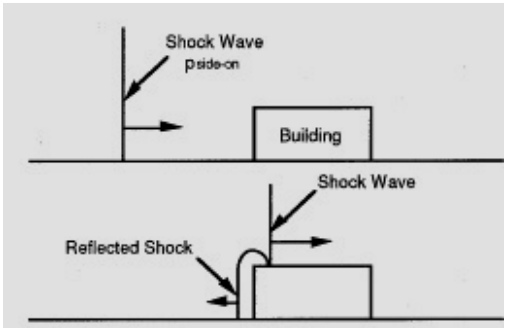


**Figure 3.12:** Normal shock wave reflection phenomena.

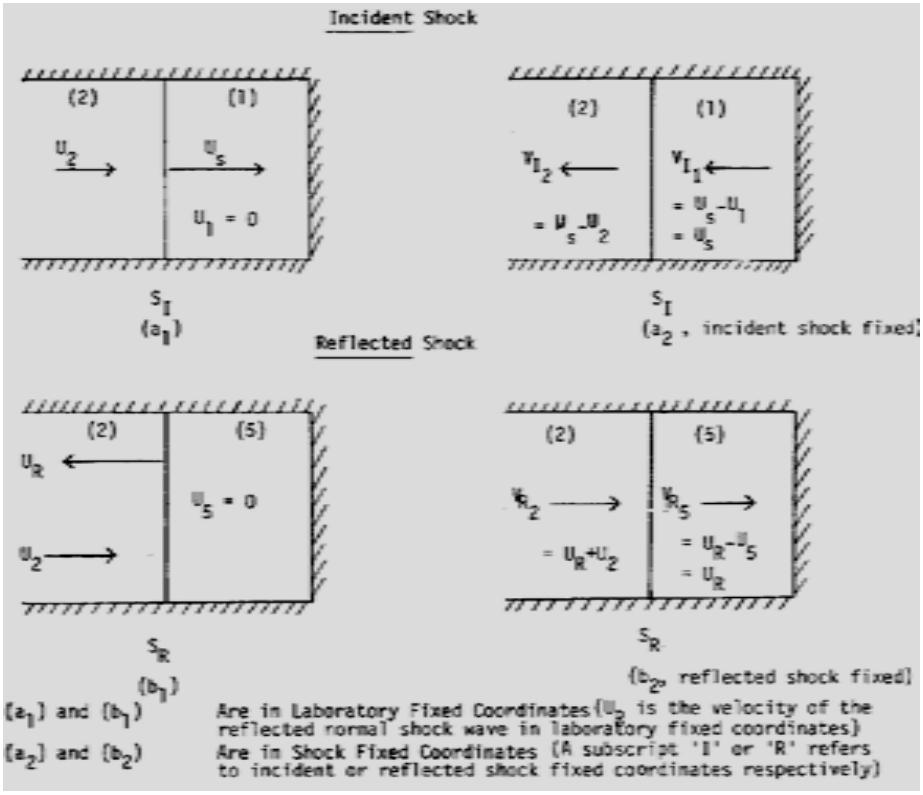


**Figure 3.13:** Flow Situation Before and After the Reflection of a Shock Wave from a Rigid Wall. Region 5 is behind the Reflected Shock Wave.

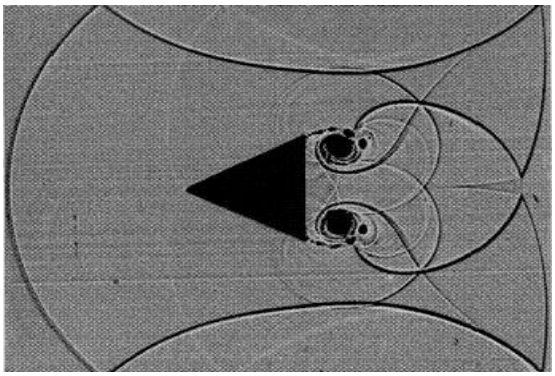

**Figure 3.14:** Shadowgraph of shock wave diffraction around a triangular obstacle taken in an air shock tube (Courtesy German-French Research Institute, St. Louis, ISL).

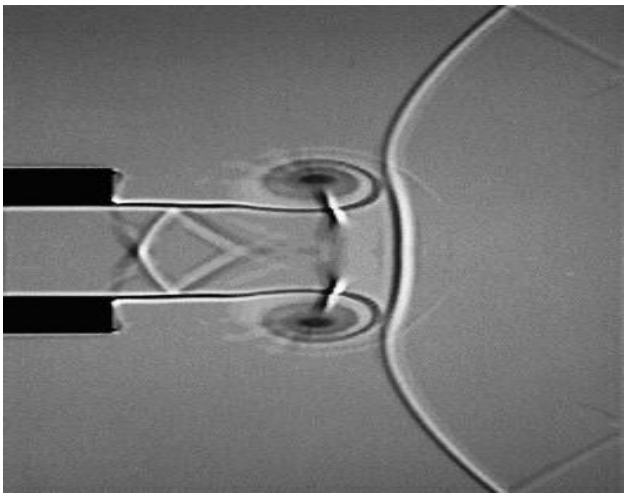

**Figure 3.15:** CFD image of Shock wave diffraction emerging from a tube.

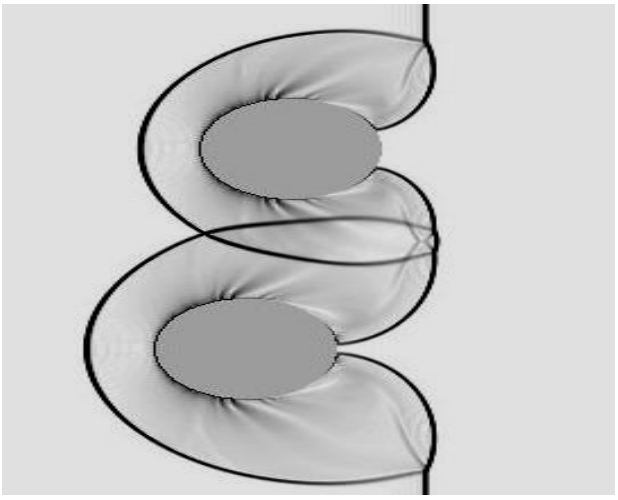

**Figure 3.16:** Shock wave diffraction over multiple cylinders.

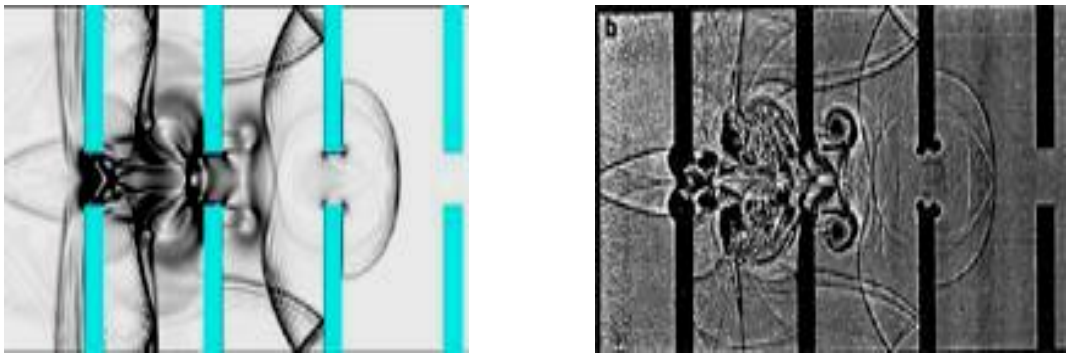

**(i)** **(ii)**

**Figure 3.17:** Interaction of shock waves with obstacles (i) CFD image; (ii) Experimental shaded photograph.

# Chapter 4

# Numerical Simulation on Shock Wave Propagation in Open Atmosphere

## 4.1 Introduction

Both numerical and experimental investigations are performed on wave propagation inside a shock tube. Previous researches on wave propagation in open atmosphere got less priority in the laboratory. Experimental realization of shock wave propagation in open atmosphere and its interaction with a solid body in the laboratory were a difficult task due to the disturbance of the sound and the measurement of wave strength in open atmosphere. In that case the results from computations can be used as diagnostics tools to analysis the characteristics of shock wave propagation in the open atmosphere. A numerical simulation of blast wave interaction with structure columns was conducted by Shi et al. [45] and their accurate estimation of blast loads on structures was essential for reliable predictions of structural response and damage. In their research, current practice in blast effect analysis and design estimated blast loads primarily based on empirical formulae obtained from field blast tests. The propagation of a planar shock wave in a $90^{o}$ branched duct was studied experimentally and numerically by Igra et al. [46] and it was shown that multiple shock wave reflections from the duct's walls caused weakening of transmitted waves and, at late times, an approach to an equilibrium, one-dimensional flow. Using a shock capturing numerical technique on the Euler equations, Rotman [47] numerically calculated the change in a two-dimensional turbulent flow, caused by the passage of a travelling shock wave and it was observed that the shock caused an increase in the turbulent kinetic energy. The Direct Numerical Simulation (DNS) data on interactions with weak shocks (Lee et al. [48]) predicted the

amplification of turbulent fluctuations and it indicated that all characteristic length scales decreased through shock interactions. Many researchers used in their numerical simulation the 3D AUTODYN, an explicit three-dimensional program for numerical analysis of wave interaction problems involving solids, liquids and gases. In the present computations, three-dimensional Euler's equation is solved by shock capturing method. HLL Reimann solver is used for shock capturing in the flow. For the better solution of the flow field, the improved three-dimensional grid adaptation technique is applied in these computations and the present 3D code for the solution of Euler equations has been developed by Jinnah [49].

## 4.2 Numerical method

### 4.2.1 Governing equation

The three-dimensional Euler equations are solved by shock capturing method. Without external forces and heat sources, the conservative form of non-dimensionalized governing equation in three-dimensional Cartesian coordinate system is

$$\frac{\partial Q}{\partial t} + \frac{\partial F}{\partial x} + \frac{\partial G}{\partial y} + \frac{\partial H}{\partial z} = 0$$

where $Q = [\rho, \rho u, \rho v, \rho w, e]$,

$F = [\rho u, \rho u^2, \rho uv, \rho uw, u(e + p)]$,

$G = [\rho v, \rho uv, \rho v^2, \rho vw, v(e + p)]$,

$H = [\rho w, \rho uw, \rho vw, \rho w^2, w(e + p)]$

Here $Q$ is the vector of conservative variables which contains mass, momentum and energy. All variables are calculated in per unit volume. $\rho$ is taken as the mass per unit volume. Three momentum terms in three-dimensional Cartesian coordinates system are $\rho u$, $\rho v$ and $\rho w$ per unit volume. Total energy, $e$ is the energy terms per unit volume in these computations. $F$, $G$ and $H$ are the three inviscid flux vectors in $X$-, $Y$-, and $Z$-axis respectively. Each flux vectors contain mass flux, momentum flux and energy flux. $\rho u$ is the mass flux and $\rho u^2$, $\rho uv$, $\rho uw$ are the momentum flux and $u(e+p)$ is the energy flux in the $X$-axis. Similarly $\rho v$ is the mass flux and $\rho uv$, $\rho v^2$, $\rho vw$ are the momentum flux and $v(e+p)$ is the energy flux in the $Y$-axis and $\rho w$ is the mass flux and $\rho wu$, $\rho vw$, $\rho w^2$ are the momentum flux and $w(e+p)$ is the energy flux in the $Z$-axis. Also $\rho$ is the fluid density and $u$, $v$ and $w$ are velocity components in each direction of Cartesian

coordinates. While *e* is the total energy per unit volume, pressure *p* can be expressed by the following state equation for ideal gas

$p=(\gamma-1)[e-\frac{1}{2}\rho(u^2+v^2+w^2)]$ where $\gamma$ is the ratio of specific heats.

The following characteristics values are used for non-dimensionalized in these computations: Characteristics temperature = *298.00K,* Characteristics length = *0.0010 m,* Characteristics pressure = *101000 Pascal,* Universal Gas constant = *8.31451,* Molecular weight = *0.029,* Ratio of specific gas constant = *1.4,* Characteristics velocity(sound velocity, c) = *292.30 m/s,* Characteristics density = *1.1821 kg/m$^3$,* Characteristics time = *3.4 μsec,* Thermal conductivity at *0$^o$C = 0.02227 W/m-K,* Fluid viscosity at *0$^o$C = 1.603E-05 Pa.S,* Prandtl number = *0.722,* Reynolds number = *21546.*

The above governing equations are solved by Finite Volume Method (FVD) and the necessary formulations are given as follows:

$$\frac{\partial u}{\partial x}=\frac{1}{\Delta x}(u_{i+1,\,j,\,k}-u_{i,\,j,\,k}) \qquad \frac{\partial v}{\partial y}=\frac{1}{\Delta y}(v_{i,\,j+1,\,k}-v_{i,\,j,\,k})$$

$$\frac{\partial w}{\partial z}=\frac{1}{\Delta z}(w_{i,\,j,\,k+1}-w_{i,\,j,\,k})$$

Similarly $$\left(\frac{\partial F}{\partial x}\right)=\frac{1}{(\Delta x)}\left(F_{i+1,\,j,\,k}-F_{i,\,j,\,k}\right),$$

$$\left(\frac{\partial G}{\partial y}\right)=\frac{1}{(\Delta y)}\left(G_{i+1,\,j,\,k}-G_{i,\,j,\,k}\right), \qquad \left(\frac{\partial H}{\partial z}\right)=\frac{1}{(\Delta z)}\left(H_{i+1,\,j,\,k}-H_{i,\,j,\,k}\right)$$

$$\left(\frac{\partial Q}{\partial t}\right)=\frac{1}{(\Delta t)}\left(Q_{i+1,\,j,\,k}-Q_{i,\,j,\,k}\right)$$

### 4.2.2 Numerical discretization and grid adaptation

The governing equations described above for compressible inviscid flow are discretized by the finite volume method. A second order, upwind Godunov scheme of Flux vector splitting method is used to discretize the inviscid flux terms and MUSCL-Hancock scheme is used for interpolation of variables. HLL Reimann solver is used for shock capturing in the flow (Toro [43]).

Three dimensional hexahedral cells with adaptive grids are used for these computations. In this grid system, the cell-edge data structures are arranged in such a

way that each cell contains six faces which are sequence in one to six and each face indicates two neighboring cells that are left cell and right cell providing all faces of a cell are arranged in a particular way by positions and coordinates in the grid system. The sequential six faces in **Fig.4.1 (i)** are *abod, adhe, abfe, efgh, bogf, dogh.*

The grid adaptation is one of the improved and computational time saving techniques, which is used in these computations. The grid adaptation is performed by two procedures, one is refinement procedure and another is coarsening procedure. The refinement and coarsening operations are handled separately in computation. The criterion used for grid adaptation is based on the truncation error ($\epsilon_T$) of the Taylor series expansion of density. The truncation error indicator $\epsilon_T$ is defined for every face of a cell and given by the ratio of the second-order derivative term to the first order one of the Taylor series of density so that

$$\epsilon_T = \max\left[\frac{|(\nabla\rho)_{lc} - (\nabla\rho)_i|}{(\alpha_f \rho_c)/dl + |\nabla\rho|_i}, \frac{|(\nabla\rho)_{lc} - (\nabla\rho)_j|}{(\alpha_f \rho_c)/dl + |\nabla\rho|_j}\right]$$

where *c* represent in **Fig.4.1 (ii)** the location of any face of a cell and *i* & *j* represent left cell & right cell of that face, *dl* is the center distance between cell *i* & *j*, $(\nabla\rho)_i$ & $(\nabla\rho)_j$ are the density gradient for cell *i* & *j*, $(\nabla\rho)_{lc} = (\rho_i - \rho_j)/dl$, $\rho_c$ is the density at the interface of right cell & left cell and $\alpha_f$ is the constant which is initially designed to prevent a zero denominator. In these computations, the value of $\alpha_f$ is used 0.02 and it is problem-independent parameter. The refinement and coarsening operation for any cell depends on ϵT value and this ϵT value is determined for each face of a cell. The criterion for adaptation for any cell is

Refinement = maximum $\epsilon_T$ of six faces of a cell > $\varepsilon_r$

Coarsening = maximum $\epsilon_T$ of six faces of a cell < $\varepsilon_c$

where $\varepsilon_r$ and $\varepsilon_c$ are the threshold values for refinement and coarsening. In these computations, the values of $\varepsilon_r$ are used 0.16~0.48 and the values of $\varepsilon_c$ are used 0.12~0.44 and the higher values are used for higher shock Mach number. The level of refinement, used in all types of computation, is 2 or 3, depending on the number of cell per unit volume. For the original grid size of 5x5x5 *(mm)*, the refined grid size will be 1.25x1.25x1.25 *(mm)* if refinement level is 2. Similarly for the original grid size of 10x10x10 *(mm)*, the refined grid size will be 1.25x1.25x1.25 *(mm)* if refinement level

is 3. So it is easy to perform the grid convergence test by using different grid sizes and different refinement levels.

In refinement procedure, the cells are selected for refinement in which every cell is divided into eight new sub cells and these new sub cells are arranged in a particular sequence so that these sub cells are used suitably in the data-structure. In three-dimensional adaptation, the volume of new sub cells is 1/8 of primary cell where in two-dimensional, this fraction is 1/4. To avoid unlimited cells refinement around shock waves, either the maximum level of refinement or the minimum cell volume or both are prescribed. When either the level or the volume of cell reaches the given limit, further refinement is prohibited. In the refinement procedure, it is required that no two neighboring cells differ by more than one refinement level. This one level-difference rule has accepted by many authors because it simplifies adaptation procedure and prevents pathologically large volume ratios under certain circumstances. However, in unsteady calculations, the rule may be mismatch in moving refined regions, say shock wave regions. To overcome this problem, pre refinement is introduced. Once a cell cannot be refined due to the level difference between itself and one or a few neighboring cells, the neighboring cells are refined no matter what values of their refinement and coarsening are. In the coarsening procedure, the eight sub cells, which are generated from the primary cell, are restored into primary cell. The cell adaptive techniques are shown in **Fig.4.2 (i)** and **Fig.4.2 (ii)**. The three-dimensional grid adaptation technique for grid size 5x5x5 (*mm*) is shown in **Fig.4.3** which is the sectional view of half numerical domain. Similarly the three-dimensional grid adaptation technique for grid size 10x10x10 (*mm*) is shown in **Fig.4.4** which is the sectional view of half numerical domain.

## 4.3 Numerical setup

### 4.3.1 Problem specifications

For the purpose of numerical solutions on shock propagation in Open Atmosphere, a 3D numerical code has been used. A shock tube is selected with a free space at its end wall and for the computation, the 3D numerical domains are used which are shown in **Fig.4.5 and Fig.4.6.** The grid size as shown in **Fig.4.5**, before adaptation is 5 x 5 x 5 *(mm)* and the initial number of grid is 10240. Similarly the grid size as shown in

**Fig.4.6**, before adaptation is 10 x 10 x 10 *(mm)* and the initial number of grid is 1280. Both numerical domains are used for grid convergence study. Each domain has two sections, one is the shock tube and another is the free space at the end of the shock tube. The selected length of the shock tube in the domain is 80 *mm* and at the end of this shock tube a free space region of 80 x 120 x 120 *(mm)* is taken for the shock wave propagation in the Open Atmosphere. The longitudinal distances (*x/d*) of any point on the centerline of the shock tube are determined from the starting point of the shock tube where *d* is the minimum dimensional length of a grid in the grid structure before adaptation and it is taken as $d = 5$ *mm*.The value $x/d = 0$ is the end point of the shock tube and the region between $x/d = 0$ and $x/d = 16$ is used as the free space region. All parameters (velocity, pressure and density etc.) are computed after the shock wave leaving the end point of the shock tube. In these computations, the threshold values for refinement are used 0.24~0.28 and the threshold values for coarsening are used 0.20~0.24 and the level of refinement is 2 and 3. Based on characteristic values, Reynolds number is 21546 and Prandtl number is 0.722.

### 4.3.2 Boundary conditions

The upstream of incident shock wave is set as an inflow boundary condition and the properties and velocities are calculated from Rankine-Hugoniot conditions with incident shock Mach number. In the downstream inflow boundary conditions; the wall surface of the shock tube is used as solid boundary conditions where the gradients normal to the surface are taken zero and the wall surface of the free space is used as open boundary condition. All solid walls are treated as non-viscous solid wall boundary.

### 4.3.3 Grid convergence study

The study of the grid convergence on the present computational results has been carried out for different levels of grid refinement and for different grid sizes. The results obtained for different incident shock Mach numbers are used for the study of the grid convergence. The refinement level two is used to solve the flow field with coarse grid and the refinement level three is used to solve the flow field with very refined grid. The results, obtained for level two and level three refined grids are compared to

observe the accuracy level of the computational results and such comparisons are used to determine the convergence behavior of the present simulation results. The sectional view of adaptive grids of refinement level 2 is shown in **Fig.4.3 and** the sectional view of adaptive grids of refinement level 3 is shown in **Fig.4.4**. It is observed that the solutions of shock wave in Open Atmosphere for different refinement levels and for different grid sizes have the good agreement.

The utilities of the grid refinement in grid convergence study are sometimes difficult if there have the more deviations between the results obtained by two successive levels of the grid refinement. In that case different sizes of the grid are suitable to use for grid convergence study. By using different grid sizes are 5x5x5 (*mm*) and 10x10x10 (*mm*), all flow parameters in the computational domain are determined and it is observed the results show well agreement.

## 4.4 Results and Discussion

In the present research work, the investigation on shock wave propagation in the open Atmosphere from the end section of the shock tube is focused mainly to observe the shock wave decaying phenomena due to expansion in the free space. The aim of the study of the shock wave decaying is to estimate the interaction effects with different objects in the free space. Spherical expansion of shock wave in the open atmosphere rapidly decreases the strength of the shock wave. The strength is dependent on the Mach number of shock wave, relation of shock wave with Mach number, distance decay of spherical shock wave and directional characteristics which are explained clearly from the present computational results. The purpose of the present work to provide a comprehensive and accurate description of shock wave propagation in the open Atmosphere. Many researchers conducted their research works on shock wave propagation in closed chamber but researches on shock wave propagation in open atmosphere got less priority and few research works were conducted by both experimentally and numerically. In the present computations, the shock wave of Mach number 1.5 is allowed to propagate from the end section of the shock tube. 80x120x120 (*mm*) domain is used at the end section of the shock tube to generate the numerical grids. All wall boundaries of the selected domain are considered as open boundaries to make it as equivalent to free space. The time-dependent Reynolds-averaged 3D Euler

equations are solved by the grid adaptation technique. All the relevant flow parameters are resolved for the shock wave of Mach number 1.5. Navier-Stokes simulation (NS) is also performed to observe the present shock wave propagation in the free space with the same incident shock Mach number. The Navier-Stokes simulation (NS) results are used to compare with the present simulation results and it is observed that there have good agreements between the present simulation results and the NS results.

During the propagation of the shock wave of Mach number 1.5, it leaves the end section of the shock tube to free space. The wave propagation in free space changes its propagation characteristics due to rapid expansion in all directions and at the same time the decay of the wave strength is observed. By measuring different parameters of the upstream and downstream flow of the wave, it is possible to estimate the decaying phenomena of the wave strength. To measure the different parameters of the upstream and downstream flow of the wave, 22 points of equal spacing are selected along the center line of the shock tube, as shown in **Fig.4.7**, in them, 8 points are selected inside the shock tube which are used to get the incident wave information and the rest of 14 points are selected outside of the end section of the shock tube which are used to establish the decaying phenomena of the wave propagation in the free space. All flow parameters (velocity, pressure and density etc.) are computed on these 22 points and the measured values indicate the wave characteristics values along the longitudinal direction (wave propagation direction, *x*-axis). The longitudinal distance (*x/d*) of any point on the centerline is determined from the end point of the shock tube where $m$ = 5.0 *mm*, the minimum grid dimension before adaptation in the grid system. The distance, $x/d$ = 0.0 at the position of the end point of the shock tube. The value, $x/m = -7.6$ is the starting point of the centerline and the value, $X/m$ = 13.4 is the ending point of the centerline.

For the shock wave position as shown in **Fig.4.8 (i)** which is just near the end section in the free space, the longitudinal velocity, *U/c* variations are determined along the center line using different grid sizes of 5x5x5 (*mm*) and 10x10x10 (*mm*). *c* is the characteristic velocity. **Fig.4.9 (i)** shows the longitudinal velocity profiles across the shock wave when the shock wave just starts to travel in the free space and the wave travelled time is $t$ = 35 $\mu sec$ and it is observed that the decay of the wave strength increases with increasing the travelled time in the free space. Also it is observed that

the velocity obtained using different grid sizes satisfies the grid convergence study. Navier-Stokes equations are also solved to compute the longitudinal velocity variation along the center line in the free space with the same incident shock Mach number. The comparisons between the Navier-Stokes simulation (NS) results and the present simulation results on velocity are performed and it is observed that there have good agreements between the present simulation results and the NS results. Similarly **Fig.4.9 (ii), (iii)** and **(iv)** show the longitudinal velocity profiles for the wave propagating time 96 $\mu sec$, 121 $\mu sec$ and 190 $\mu sec$ respectively in the free space, where the position of the wave is shown in **Fig.4.8 (ii)**, **(iii)** and **(iv)** and it is observed that the shock induced longitudinal flow velocity decreases in all cases for the different wave positions which indicates the decay of the wave strength. Also the longitudinal velocity from NS results for the travelled time 35 $\mu sec$, 96 $\mu sec$, 121 $\mu sec$ and 190 $\mu sec$ of the wave have the good agreements with the present simulation results.

For the shock wave position as shown in **Fig.4.8 (i)** which is just near the end section in the free space, the normalized pressure, $P/P_o$ variations are determined along the center line using different grid sizes of 5x5x5 (*mm*) and 10x10x10 (*mm*). $P_o$ is the characteristic pressure, taken as Atmospheric pressure. **Fig.4.10 (i)** shows the normalized pressure profiles across the shock wave when the shock wave just starts to travel in the free space and the wave travelled time, $t$ = 35 $\mu sec$ and it is observed that the wave strength decreases with the increase of the travelled time in the free space. Also it is observed that the pressure obtained using different grid sizes satisfies the grid convergence study. Navier-Stokes equations also solve to compute the normalized pressure variation along the center line in the free space with the same incident shock Mach number. The comparisons between the Navier-Stokes simulation (NS) results and the present simulation results on pressure are performed and it is observed that there are good agreements between the present simulation results and the NS results. Similarly **Fig.4.10 (ii), (iii)** and **(iv)** show the normalized pressure profiles for the wave propagating time 96 $\mu sec$, 121 $\mu sec$ and 190 $\mu sec$ respectively in the free space, where the position of the wave is shown in **Fig.4.8 (ii)**, **(iii)** and **(iv)** and it is observed that the normalized pressure decreases across the wave in all cases for the different wave positions which indicates the decay of the wave strength. Also the normalized pressure

from NS results for the travelled time 35 $\mu sec$, 96 $\mu sec$, 121 $\mu sec$ and 190 $\mu sec$ of the wave have the good agreements with the present simulation results.

For the shock wave position as shown in **Fig.4.8 (i)** which is just near the end section in the free space, the normalized density, $\rho/\rho_o$ variations are determined along the center line using different grid sizes of 5x5x5 (*mm*) and 10x10x10 (*mm*). $P_o$ is the characteristic density. **Fig.4.11 (i)** shows the normalized density profiles across the shock wave when the shock wave just starts to travel in the free space and the wave travelled time, $t$ = 35 $\mu sec$ and it is observed that the decay of the wave strength increases with increasing the travelled time in the free space. Also it is observed that the density obtained using different grid sizes satisfies the grid convergence study. Navier-Stokes equations also solve to compute the normalized density variation along the center line in the free space with the same incident shock Mach number. The comparisons between the Navier-Stokes simulation (NS) results and the present simulation results on density are performed and it is observed that there have good agreements between the present simulation results and the NS results. Similarly **Fig.4.11 (ii), (iii)** and **(iv)** show the normalized density profiles for the wave propagating time 96 $\mu sec$, 121 $\mu sec$ and 190 $\mu sec$ respectively in the free space, where the position of the wave is shown in **Fig.4.8 (ii)**, **(iii)** and **(iv)** and it is observed that the normalized density decreases across the wave in all cases for the different wave positions which indicates the decay of the wave strength. Also the normalized density from NS results for the travelled time 35 $\mu sec$, 96 $\mu sec$, 121 $\mu sec$ and 190 $\mu sec$ of the wave have the good agreements with the present simulation results.

For the shock wave position as shown in **Fig.4.8 (i)** which is just near the end section in the free space, the lateral velocity, $v/c$ variations are determined along the center line using different grid sizes of 5x5x5 (*mm*) and 10x10x10 (*mm*). **Fig.4.12 (i)** shows the lateral velocity, $v/c$ profiles across the shock wave when the shock wave just starts to travel in the free space and the wave travelled time is $t$ = 35 $\mu sec$ and it is observed that the magnitude of the lateral velocity, $v/c$ follows the zero line which proves that the shape of the wave propagation is spherical. . Also it is observed that the velocity obtained using different grid sizes satisfies the grid convergence study. Similarly **Fig.4.12 (ii), (iii)** and **(iv)** show the lateral velocity, $v/c$ profiles after the wave propagating time 96 $\mu sec$, 121 $\mu sec$ and 190 $\mu sec$ respectively in the free space, where

the position of the wave is shown in **Fig.4.8 (ii)**, **(iii)** and **(iv)** and it is observed that the shock induced lateral velocity, *v/c* follows the zero line approximately. Also the lateral velocity, *v/c* from NS results for the travelled time 35 *μsec,* 96 *μsec,* 121 *μsec* and 190 *μsec* of the wave have the good agreements with the present simulation results.

For the shock wave position as shown in **Fig.4.8 (i)** which is just near the end section in the free space, the lateral velocity, *w/c* variations are determined along the center line using different grid sizes of 5x5x5 (*mm*) and 10x10x10 (*mm*). **Fig.4.13 (i)** shows the lateral velocity, *w/c* profiles across the shock wave when the shock wave just starts to travel in the free space and the wave travelled time is $t$ = 35 *μsec* and it is observed that the magnitude of the lateral velocity follows the zero line which proves that the shape of the wave propagation is spherical. . Also it is observed that the velocity obtained using different grid sizes satisfies the grid convergence study. Similarly **Fig.4.13 (ii), (iii)** and **(iv)** show the lateral velocity, *w/c* profiles after the wave propagating time 96 *μsec,* 121 *μsec* and 190 *μsec* respectively in the free space, where the position of the wave is shown in **Fig.4.8 (ii)**, **(iii)** and **(iv)** and it is observed that the shock induced lateral velocity, *w/c* follows the zero line approximately. Also the lateral velocity, *w/c* from NS results for the travelled time 35 *μsec,* 96 *μsec,* 121 *μsec* and 190 *μsec* of the wave have the good agreements with the present simulation results.

In the present computation, the longitudinal velocity along the *x*-direction is the normal velocity on *yz*-plane and because of the zero velocity on other *y* and *z* direction, the tangential velocity of the wave in the free space is zero. So the wave is always propagating in the normal direction. Similarly if the wave propagates in *y*-axis, that is, the direction is normal on *zx*-plane, then the tangential velocity along *x* and *z* axis will be zero. So the propagation is always observed in radial direction and the surfaces of the wave propagation in the open Atmosphere have the tendency to be spherical in shape.

## 4.5 Summary

The shock wave propagation in the open atmosphere has been investigated by means of Euler simulation where the flow is considered as laminar and non-viscous flow. The results have been compared with the Navier-Stokes Simulation (NS) results

to establish the absence of viscous effects in the present flow. Due to absence of the solid boundary of the selected numerical domain in the free space, the fluid flow will act as non-viscous flow. So the solution of the Euler equation is considered as the optimum solution where the Navier-Stokes Simulation (NS) results are used to verify the Euler simulation results. The advantages of the use of Euler simulation are the simple equations to solve, faster to run the numerical code and more accurate solutions due to fewer boundary conditions as compare to NS.

The present numerical technique is used properly to determine the decay of the shock wave propagation in the open atmosphere and at the same time, the spherical expansion is observed by numerical imaging. The experiments on the shock wave propagation the open atmosphere are the difficult tasks due to strong sound wave generation in the lab and to measure the wave strength in the open atmosphere by sensing devices. In that case, the numerical simulation can be used as diagnostic tools to observe the wave propagation phenomena. Numerical techniques for such types of propagation are more suitable to get the reliable results and easily estimate the physical data structure which is difficult to measure in experiment.

# List of Figures

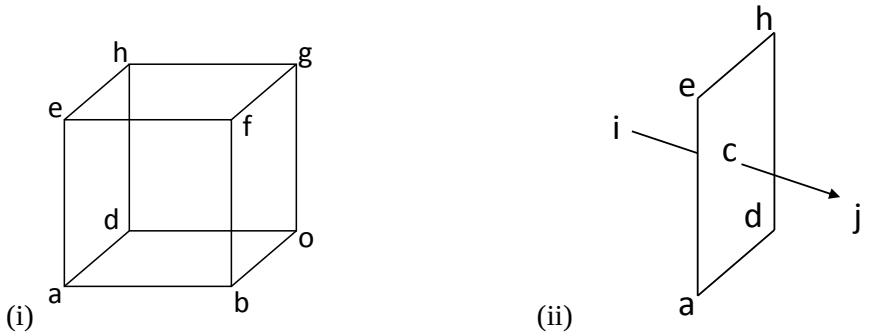


**Figure 4.1:** (i) Three-dimensional cell with six faces; (ii) Each face addresses the center of two neighboring cells, *i* and *j*.

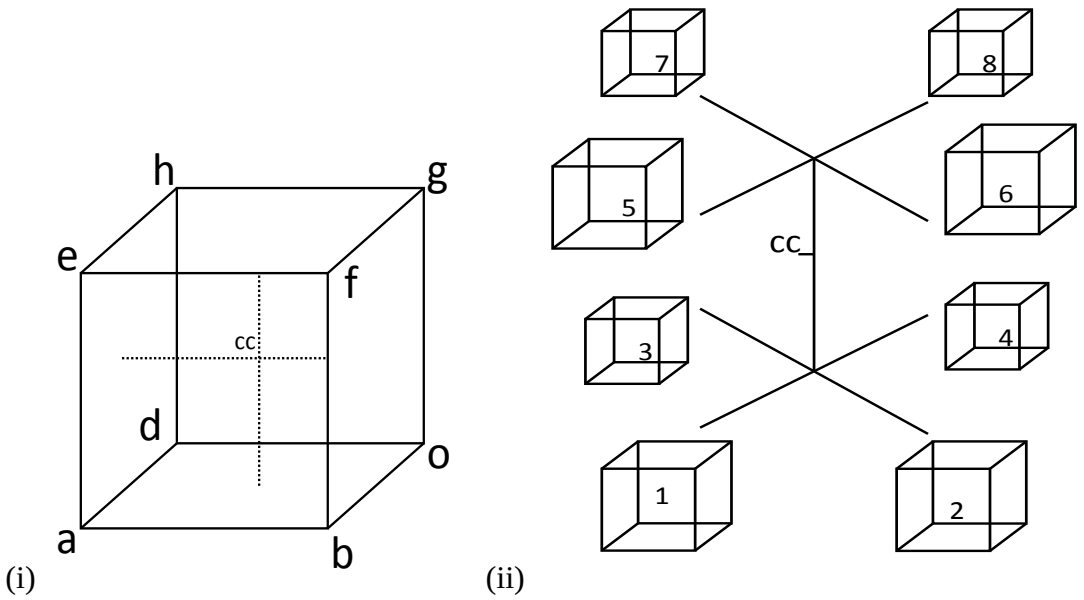


**Figure 4.2:** (i) Primary cell before adaptation where the center of the cell, cc is shown; (ii) Sequence of the eight cells after refinement of the primary cell.

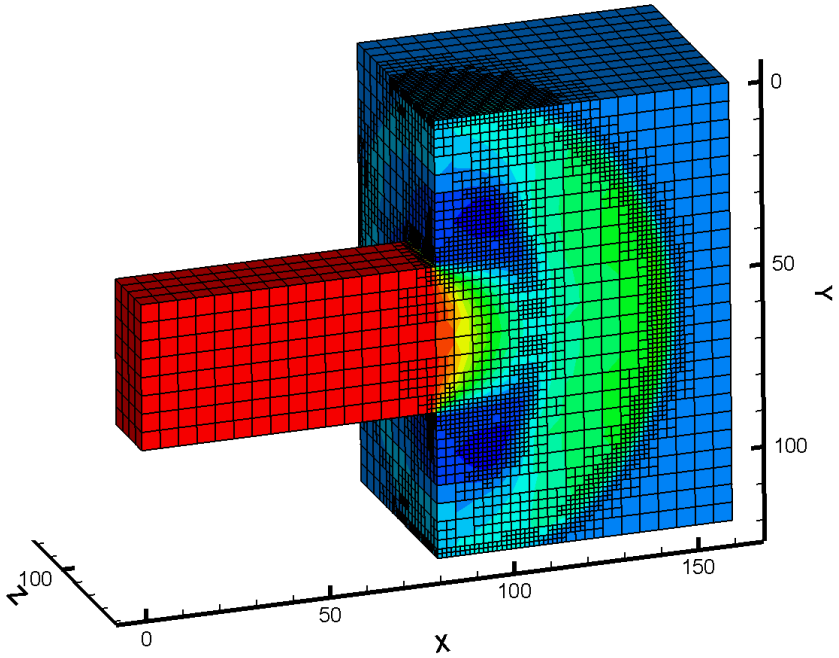


**Figure 4.3:** Sectional view of half numerical domain of grid size 5x5x5 (*mm*) where 3D grid adaptation technique is shown.

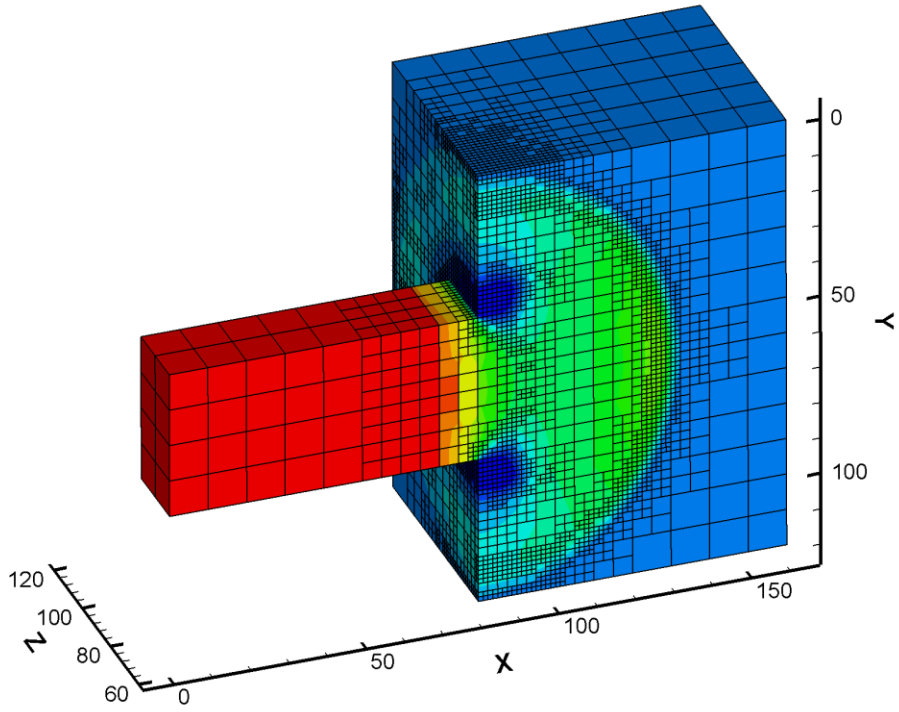


**Figure 4.4:** Sectional view of half numerical domain of grid size 10x10x10 (*mm*) where 3D grid adaptation technique is shown.

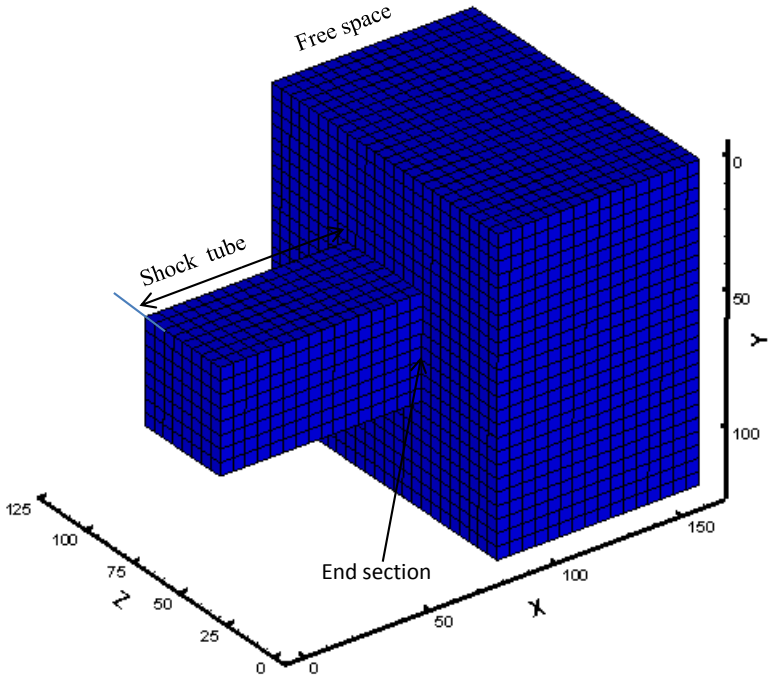


**Figure 4.5:** 3D numerical domain where the grid size is 5x5x5 (*mm*).

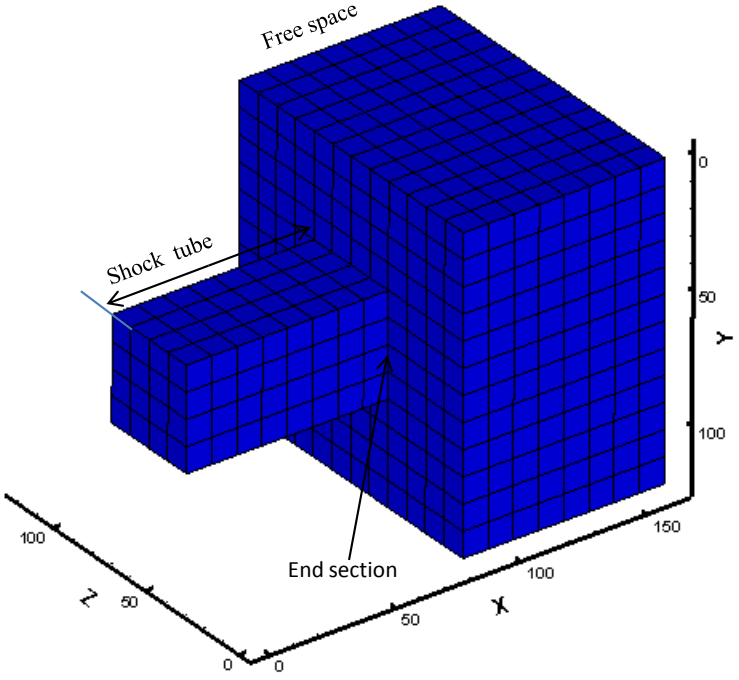


**Figure 4.6:** 3D numerical domain where the grid size is 10x10x10 (*mm*).

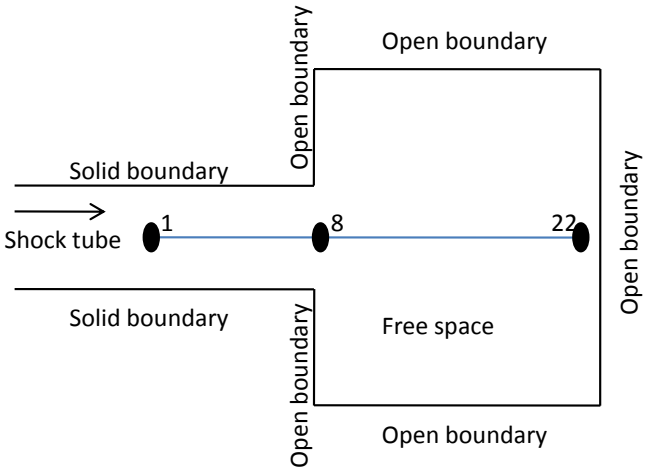


**Figure 4.7:** Schematic layout of the shock tube and the relative position of the free space.

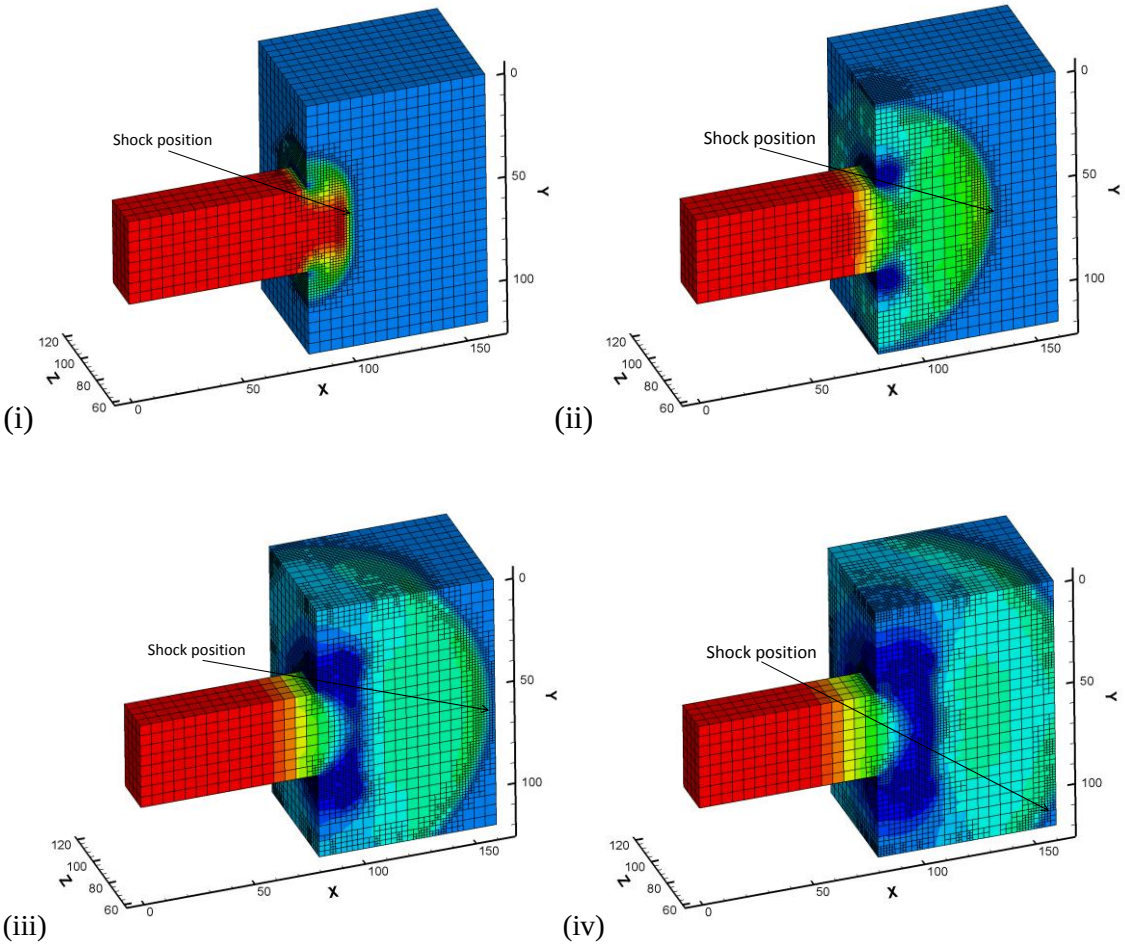


(i) (ii) (iii) (iv)

**Figure 4.8:** Shock wave position from the end section of the shock tube in the free space after the wave travelled time **(i)** $t$ = 35 $\mu sec$, **(ii)** $t$ = 96 $\mu sec$, **(iii)** $t$ = 121 $\mu sec$, **(iv)** $t$ = 190 $\mu sec$.\

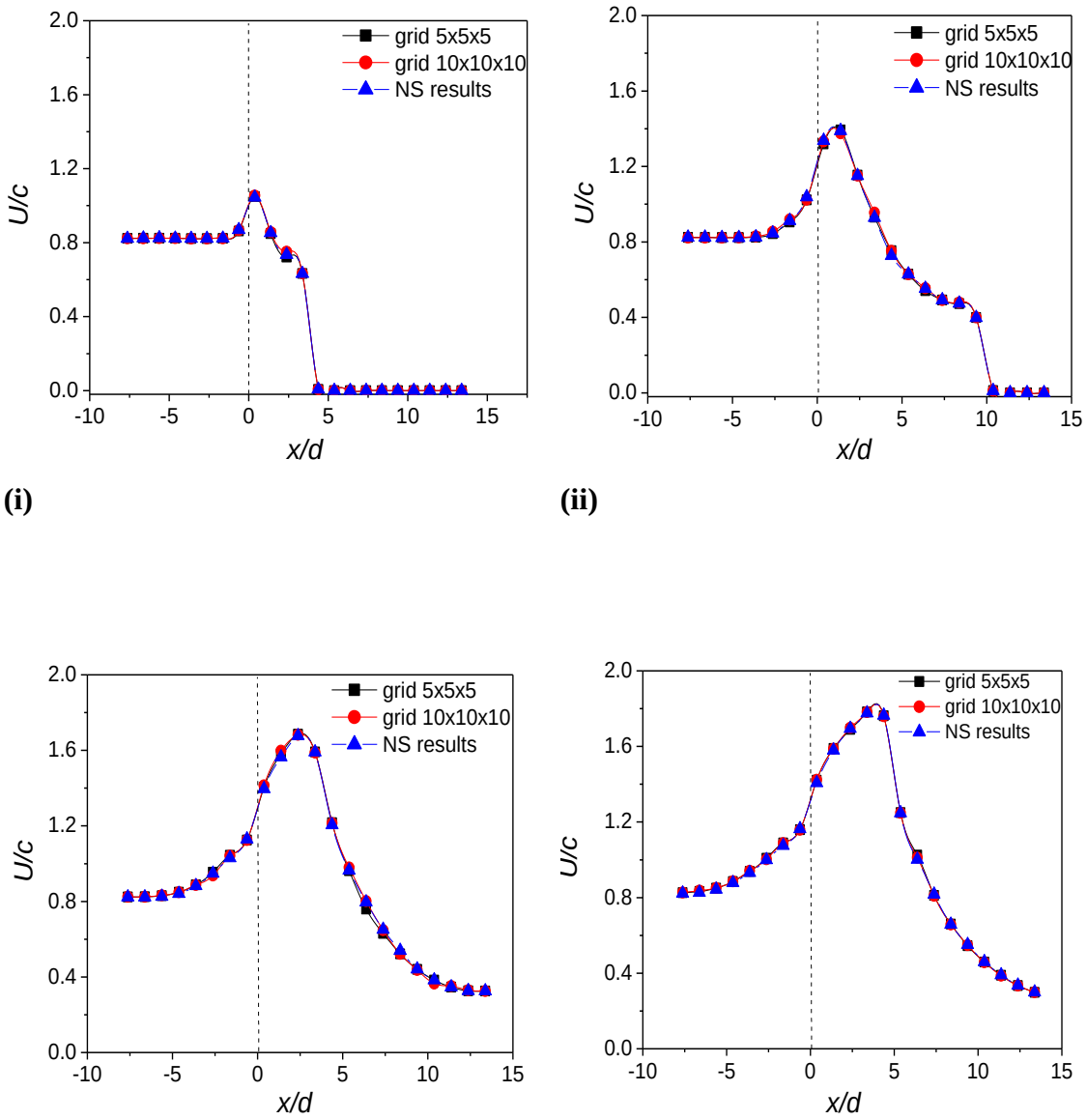


**Figure 4.9:** Longitudinal velocity, *U/c* profiles along the centerline of the free space using different grid sizes when the wave travelled time; **(i)** $t$ = 35 $\mu sec$, **(ii)** $t$ = 96 $\mu sec$, **(iii)** $t$ = 121 $\mu sec$, **(iv)** $t$ = 190 $\mu sec$.

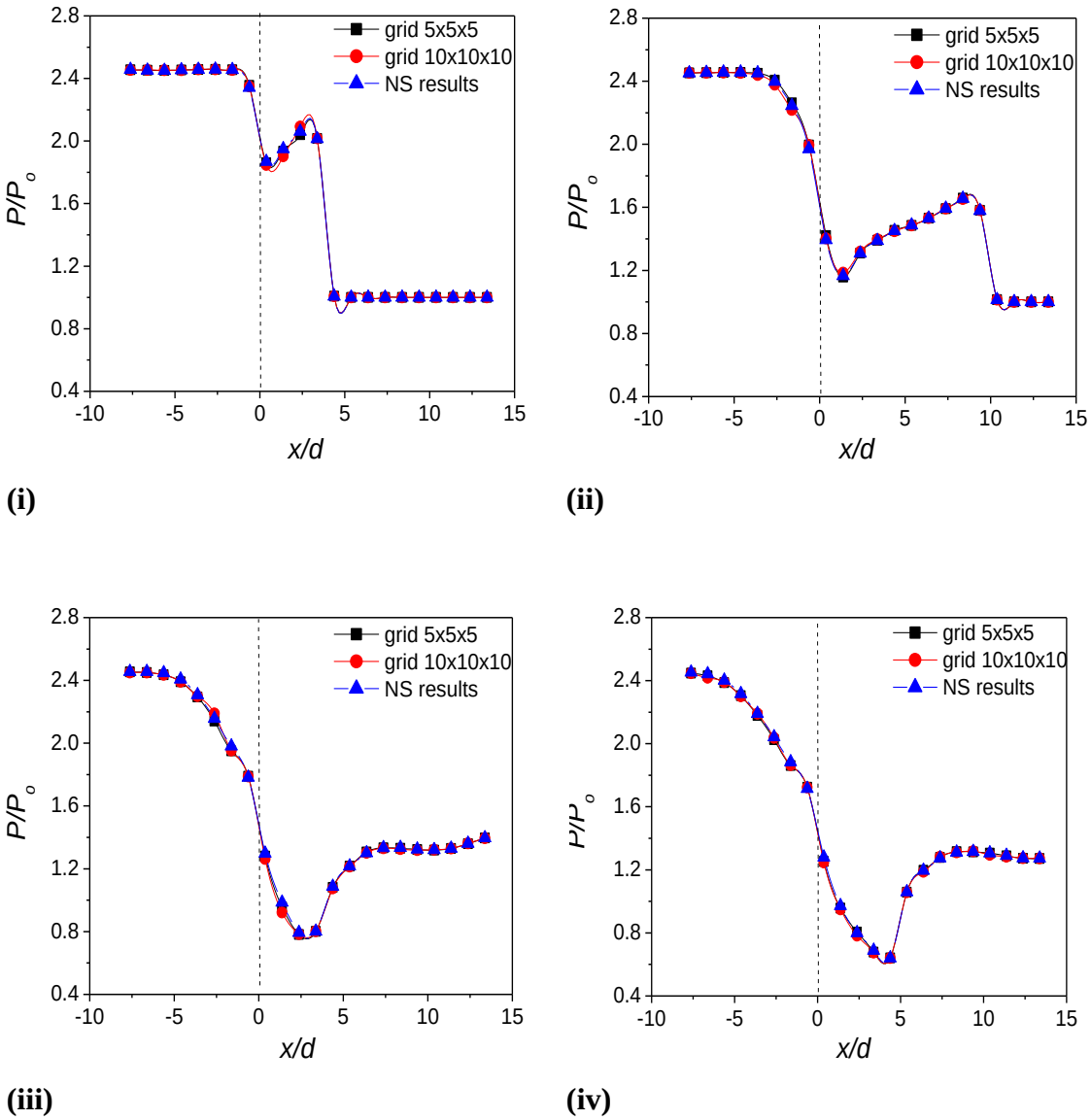


**Figure 4.10:** Normalized pressure, $P/P_o$ profiles along the centerline of the free space using different grid sizes when the wave travelled time; **(i)** $t$ = 35 $\mu sec$, **(ii)** $t$ = 96 $\mu sec$, **(iii)** $t$ = 121 $\mu sec$, **(iv)** $t$ = 190 $\mu sec$.

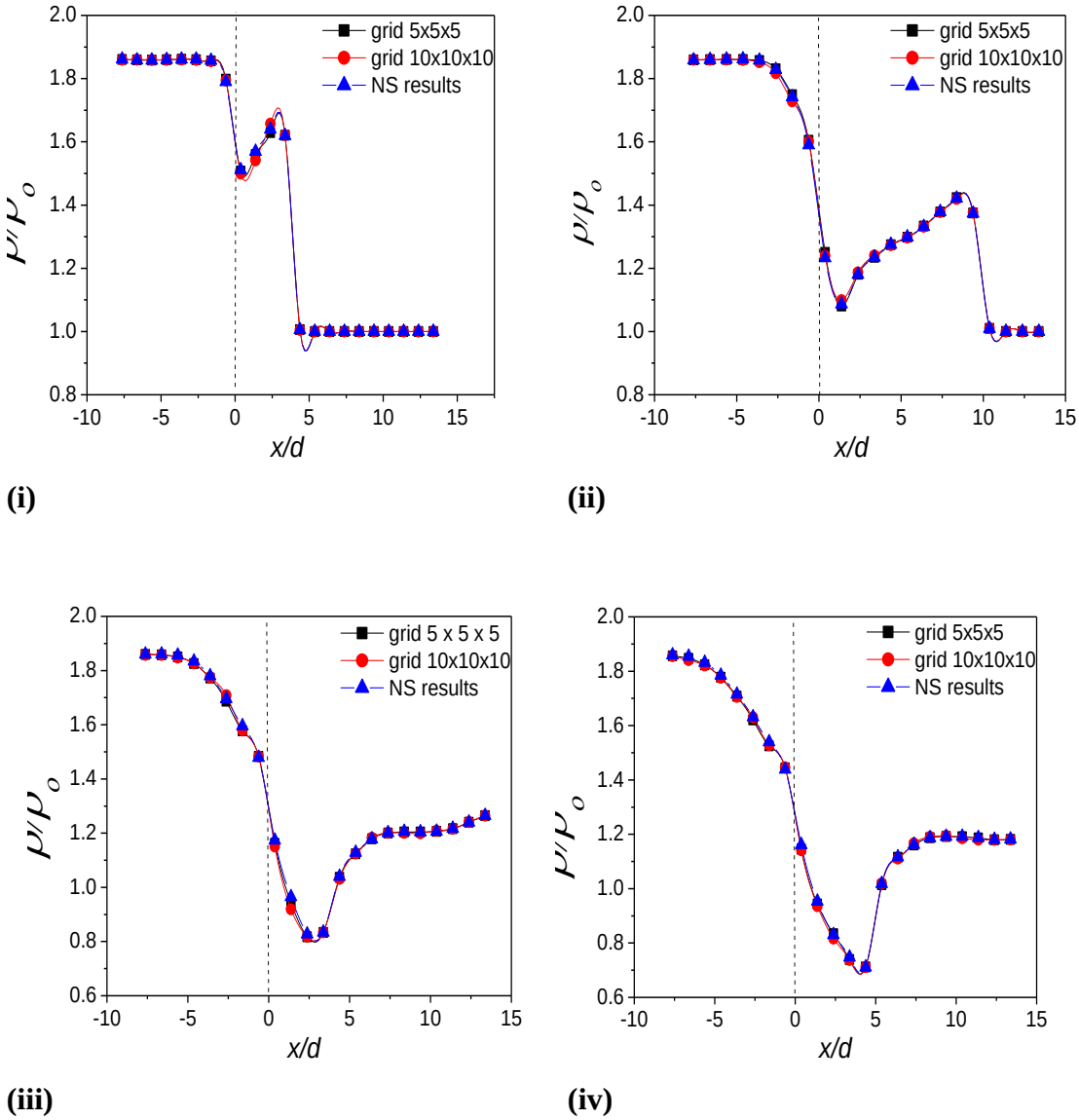


**Figure 4.11:** Normalized density, $\rho/\rho_o$ profiles along the centerline of the free space using different grid sizes when the wave travelled time; **(i)** $t$ = 35 $\mu sec$, **(ii)** $t$ = 96 $\mu sec$, **(iii)** $t$ = 121 $\mu sec$, **(iv)** $t$ = 190 $\mu sec$.

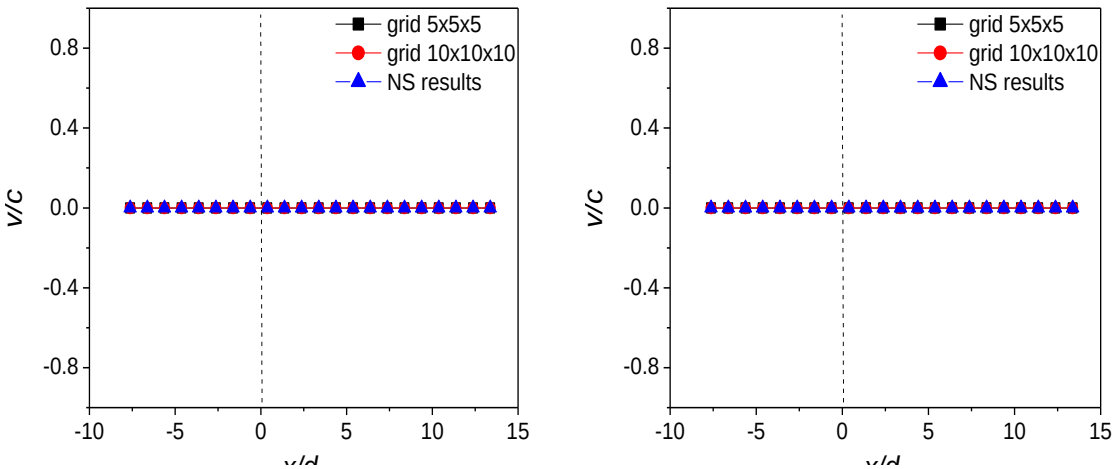


**(i)** **(ii)**

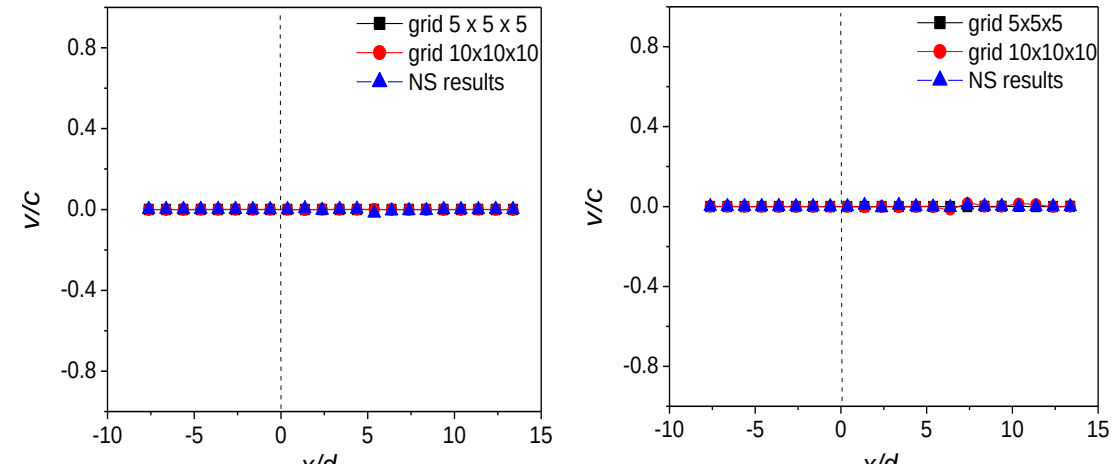


**(iii)** **(iv)**

**Figure 4.12:** Lateral velocity, *v/c* profiles along the centerline of the free space using different grid sizes when the wave travelled time; **(i)** $t$ = 35 $\mu sec$, **(ii)** $t$ = 96 $\mu sec$, **(iii)** $t$ = 121 $\mu sec$, **(iv)** $t$ = 190 $\mu sec$.

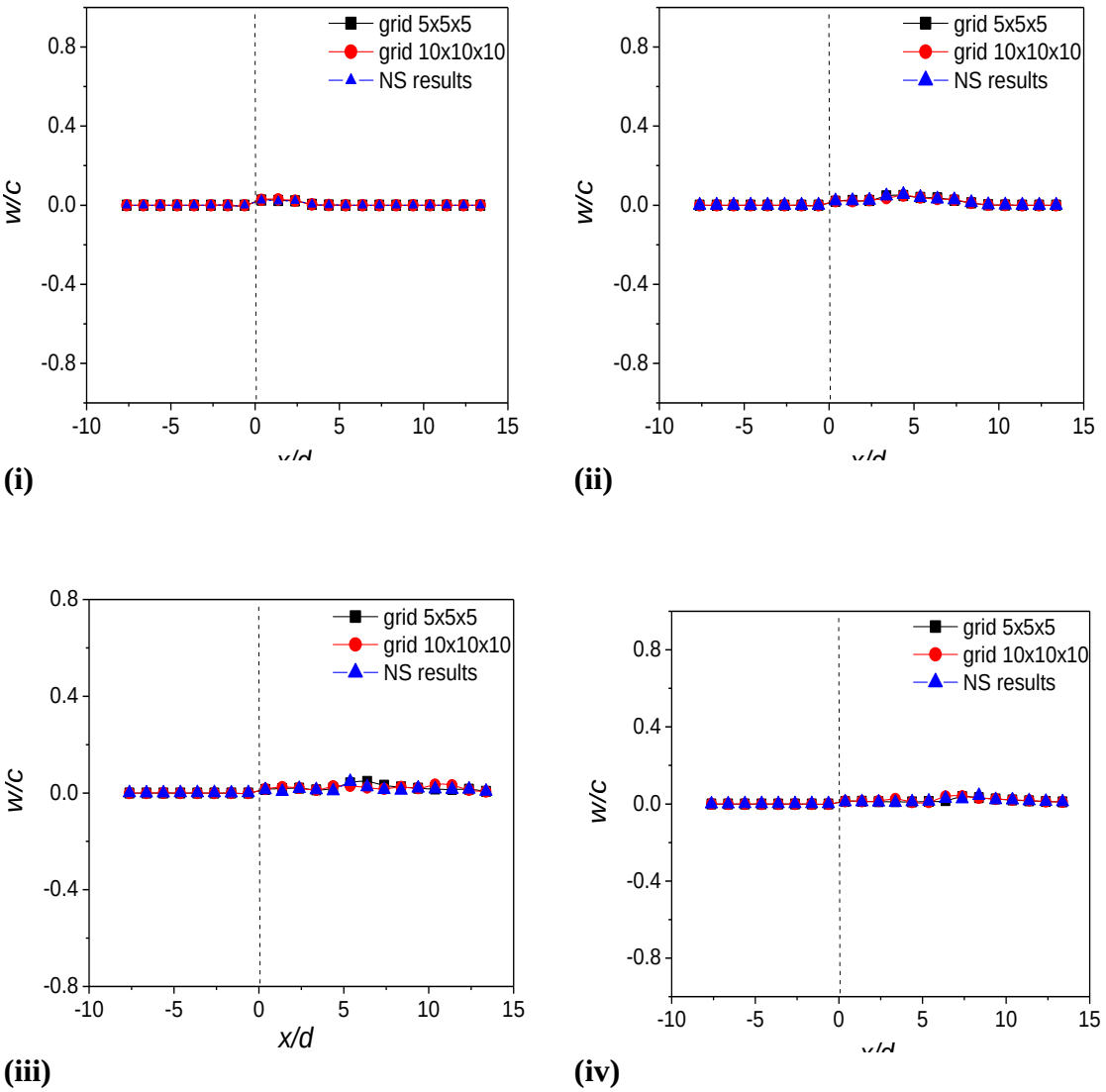


**Figure 4.13:** Lateral velocity, *w/c* profiles along the centerline of the free space using different grid sizes when the wave travelled time; **(i)** $t$ = 35 $\mu sec$, **(ii)** $t$ = 96 $\mu sec$, **(iii)** $t$ = 121 $\mu sec$, **(iv)** $t$ = 190 $\mu sec$.

# Chapter 5

# Experiment on Wave Propagation in Open Atmosphere

## 5.1 Introduction

In the study of wave propagation in the open atmosphere, an experiment has been conducted to measure the wave speed during the propagation in the open atmosphere by the present technique. To measure the travelling time of the wave propagation in the open atmosphere, it is desirable to obtain time measurements to an accuracy of microsecond level. The investigation of wave propagation in the open atmosphere is one of the complex experimental works. Experimental investigation is essential to improve the understanding of wave propagation with subsonic or supersonic speed in the open atmosphere. Some optical techniques can able to visualize the propagation and the location of the wave. High speed camera is also used for the flow visualization to analysis the structure of the wave. The application of some of these techniques to supersonic and hypersonic flows can be highly challenging due to the high velocity, strong gradients and restricted optical access generally encountered. Widely used qualitative and semi-quantitative optical flow diagnostics are shadowgraph, schlieren, and interferometry. Schlieren visualizations of weak shock waves from common phenomena include loud trumpet notes, various impact phenomena that compress a bubble of air, bursting a toy balloon, popping a champagne cork, snapping a wooden stick, and snapping a wet towel. The balloon burst, snapping a ruler on a table, and snapping the towel and a leather belt all produced readily visible shock wave phenomena. Doig et al. [1] conducted experiment where direction-indicating color schlieren flow visualization was used to find out optically the general efficiency of the methods. Multiple images were taken during a single tunnel run, which allowed, to

some extent, confirmation of the general steadiness of the flow. The light source used in the experiments had a flash duration of 200 $\mu s$, which was short enough to 'freeze' any large-scale motions in the flow but long enough to average out small-scale fluctuations such as free-stream turbulence and boundary layer effects on the test section windows.

Laser-based techniques such as laser Doppler anemometry and particle image velocimetry are well established for investigation of supersonic flows, but as yet their use in hypersonic flows has been limited. Other relevant measurement techniques include particle tracking velocimetry, Doppler global velocimetry, laser-two-focus anemometry, background oriented schlieren and laser induced fluorescence methods, molecular tagging velocimetry for velocity measurement and thermo-graphic phosphor thermometry for surface temperature measurement. Laser measurement techniques are becoming more commonly applied to many areas of thermo-fluids and heat transfer. An area of their application, which presents highly challenging requirements, is in the measurement of aerospace flows. In the shock wave research laboratory, Tohoku University Japan, the speed of projectile was measured by Shimadzu's HPV-1 High Speed Video Camera and the time elapsed from recording the first frame up to the $100^{th}$ frame was only about one ten-thousandth of a second. The ability to record dynamic images over short intervals is extremely significant.

In the study of metal-high explosive detonation wave interaction, by the pin technique, it is desirable to obtain time measurements to an accuracy of less than 1 $\mu sec$ over a total time interval of 5 $\mu sec$. Commercial instruments capable of a high degree of time resolution were not available and a special instrument was developed for this purpose. A cathode-ray oscilloscope, displaying deflection type event pulses, is converted into a precise time-measuring instrument by a calibrated zig-zag sweep. The record is obtained by single-shot photography of the cathode-ray tube sweep which is triggered by the event to be measured. Kobiera et al. [2] conducted experiment on the shock wave propagation through the test section and the shock wave causes a disturbance of the droplets; this process was visualized by a schlieren system and recorded by a high-speed camera. The camera was synchronized with the igniter that was connected to the spark plug mounted in the driver section. The test section was also equipped with a pressure measurement system (two pressure sensors and amplifiers)

whose signals were recorded on an oscilloscope. The sensors were located ahead of the test section windows and they could be used to measure the shock velocity and pressure waveform. Pianthong et al. [3] conducted experiment with the use of the shadowgraph method, showing the projectile traveling inside and leaving the pressure relief section at a velocity of about 1100 *m/s*. they also visualized the supersonic diesel fuel jets (velocity about 2 *km/s*) by the shadowgraph method.

In the present method, metal to metal touch switches generate pulses for triggering which open and close the gate to allow and stop the crystal frequency for counting. Using the number of pulse counted, the traveling time between the trigger points is measured for the subsonic or supersonic objects. Due to pressure difference across the wave, the trigger is operated by the pressure response to detect the wave position in the open atmosphere. This is one of the easier methods to measure the traveling time of the subsonic or supersonic wave between the two trigger points as compare to other methods. Even visualizations of the wave front or the pressure response from pressure transducers are the familiar methods to measure the strength of the wave or to identify its locations but the present technique is more reliable and accurate to measure the time. Normally the propagation time of the logic gates is not more than 20 nanoseconds, so the accuracy level of the measured time will be less than 0.006%.

## 5.2 Experimental Setup

Experiments are carried out in a single diaphragm horizontal shock tube in the Fluid Mechanics Laboratory of the Islamic University of Technology (IUT). **Figure 5.1** shows a schematic illustration of the horizontal shock tube consisting of 150 mm diameter and 1.5 meter long high pressure chamber made of mild steel. High pressure chamber is the driver section of the shock tube and the driven section of the shock tube is 100 mm diameter and 5 meter long. A diaphragm is used between two flanges of the driver section and the driven section of the shock tube and tightly fastens by nut-bolt with proper gasket. The diaphragm is separated high pressure chamber from atmospheric pressure and by inserting the pressure inside the high pressure chamber, chamber pressure gradually increases and due to high pressure of the chamber, the diaphragm feels tension force and at certain instant it starts to rupture. Due to sudden rupture, the fluid from the high pressure chamber starts to flow with high velocity and

when the flow velocity reaches to exceed sonic limit, the shock wave generates after travelling certain distance in the driven section. In the present experiment, the shock wave is allowed to propagate in the open atmosphere, even though it is not safe for human beings if the shock wave strength overcomes the moderate Mach number. After propagating the shock wave in the open Atmosphere, the post-shocked high speed air generated from end section of the shock tube, which is shown in **Fig. 5.2.** High pressure of fluid which is less than chamber pressure, drives the shock front and the rupture of the diaphragm depends on the material properties of the diaphragm and it is observed that better toughness, slightly brittle properties of the diaphragm can able to generate stronger shock wave. On the other hand, in smaller diameter shock tubes, diaphragms are ruptured relatively uniform and quickly and then incident shock formation distance is relatively short and its frontal shape is planar. However, in a large size shock tube under study, large diameter plastic diaphragm such as Mylar ones tend to rupture non-uniformly to generate three dimensionally distorted shock fronts. Even though distorted shock fronts became planar, irregular wavelets persisted behind the incident shock front for relatively long distance. In the present experiment, three types of diaphragm are used where ductile typed thick polythene diaphragm is not suitable to generate shock wave. Raksin sheet and X-ray film are suitable to generate shock wave in the driven section of the shock wave. Rupturing characteristics of different diaphragms are observed in the experiments which are shown in **Figs. 5.3 (i)-(iii).** Ductile typed thick polythene diaphragm starts continuous deformation as increasing the pressure of the chamber and it is continuing the deformation of the diaphragm up to the rupturing of the diaphragm happened. So such type of diaphragm rupturing fails to create supersonic velocity suddenly at the driven section which finally generates shock wave. Due to brittle characteristics of the Raksin sheet and X-ray film, the deformation is not linear as increasing the pressure of the chamber and the rupturing happened suddenly making large ruptured area. Due to sudden diaphragm ruptured, a fluid column from high pressure chamber starts to move through driven section and creates shock wave after travelling certain distance in the driven section. At the same time, an expansion wave, known as expansion fan, moves through high pressure chamber, as a result, a contact surface is created which is moved behind the shock wave with lower velocity, as shown in **Fig. 5.4. Figure 5.4** gives an *x-t* diagram for a typical shock wave indicating the

available test time in the test section of the shock tube. The test time is terminated by the arrival of the reflected expansion wave head from the driver end as indicated in **Fig. 5.4** for moderate incident shock Mach numbers, and the arrival of the contact surface terminates the test time for the stronger incident shock waves.

In the present experiment, a time measuring device has been constructed to measure the subsonic or supersonic wave propagation time in microsecond level in the open Atmosphere. A piezoelectric crystal type HOSONIC, D349 which generates 3579540 pulses per second is used to measure the traveling time in micro-second level for any objects with subsonic or supersonic speed in open atmosphere. A circuit has been developed by using two trigger points which is shown in **Fig. 5.5**. Metal to metal touch switches generate pulses for triggering which open and close the gate to allow and stop the crystal frequency for counting. A metal wire carrying sufficient voltage when touches another metal wire then a voltage signal generates in that wire which causes to change the state of the AND gate to open and allow to pass the crystal frequency through it. Similarly trigger-2 closes the AND gate not to pass the crystal frequency through it. In these triggering techniques, it is not necessary to change the signal, like light, heat, magnetic signal into electric voltage signal. A direct metal to metal contact triggering is more efficient as compared to other sensing devices, like pressure transducers, Electro-optic sensors, Infrared sensors, Magnetic sensors etc. Using the number of pulse counted, the traveling time between the trigger points is measured for the subsonic or supersonic objects. Though visualizations of the wave front or the pressure response from pressure transducers are the familiar methods to measure the strength of the wave or to identify its locations but the present technique is more reliable and accurate to measure the time. Normally the propagation time of the logic gates is not more than 20 nanoseconds, so the accuracy level of the measured time will be less than 0.006%.

To conduct an experiment on subsonic or supersonic objects, a shock tube is constructed in the Fluid Mechanics Laboratory of IUT for wave propagation in the open atmosphere. A compressor of 10 $kg/cm^2$ pressure range is used to raise the air pressure in the pressure chamber of the shock tube. Due to sudden rupture of the diaphragm for the chamber pressure of range 3.5 – 4.5 $kg/cm^2$, a wave generates in a shock tube which travels with subsonic or supersonic speed depending on the pressure

in the chamber during rupture. If pressure range increases, a supersonic shock wave generates. Two trigger points (Trigger-1 and Trigger-2) are installed 61.5 *cm* apart in the shock tube to measure the incident wave Mach number. Similarly other 4 trigger points are also installed at different positions by the supporting rod, shown in **Fig. 5.6**, to measure the wave speed during the propagation in the open Atmosphere and the measured traveling time between different triggers are recorded. Trigger-2 is installed at the end point of the shock tube where $x = 0.0$ *cm* is taken and all other trigger distances are measured from Trigger-2. Here the distance of the Trigger-3 from Trigger-2 is 9 *cm*, shown in **Fig. 5.7**. Similarly from Trigger-2, the distance of Trigger-4 is 18.5 *cm*, the distance of Trigger-5 is 28.5 *cm* and the distance of Trigger-6 is 38.5 cm, shown in **Fig. 5.7**.

## 5.3 Numerical setup

### 5.3.1 Problem specifications

In the present simulation, the valid 2D numerical code has been used to compare with experimental results. The validity test of 3D code for the solution of Euler equations has already performed in the previous chapter. The present numerical problem is axisymetric in computation. So, avoiding 3D complex solution and more computation time, the 2D code for the solution of Euler equations are used for the shock wave propagation in the open Atmosphere. The governing equation is,

$$\frac{\partial Q}{\partial t} + \frac{\partial F}{\partial x} + \frac{\partial G}{\partial y} = 0$$

where $Q$ is the vector of conservative variables, $t$ is the time, $F$ and $G$ are the in viscid flux vectors. The governing equation described above for compressible inviscous flow is discretised by the finite volume method. A second order, upwind Godounov scheme of Flux vector splitting method is used to discrete the inviscid flux terms where HLL-Reimann solver is used for shock capturing in the flow. Two dimensional cells with adaptive grid systems are used for these computations. In this grid systems, the cell-edge data structures are arranged in such a way that each cell contains four faces which are in sequence from one to four and each face indicates two neighboring cells that are left cell and right cell providing all faces of a cell are vectorized by position and coordinate in the grid systems.

The initial two-dimensional grid systems are shown in **Fig. 5.8**. The physical size of each cell before adaptation is equal to 13 x 13 (*mm*). The grid adaptation is one of the improved and computational time saving techniques, which is used in these computations. The grid adaptation is performed by two procedures, one is refinement procedure and another is coarsening procedure. The refinement and coarsening operations are handled separately in computation.

### 5.3.2 Boundary Conditions

The upstream of incident shock wave is set as inflow boundary condition, the properties and velocities of which are calculated from Rankine-Hugoniot conditions with incident shock Mach number. The downstream inflow boundary conditions, shown in **Fig. 5.8**, are open boundary conditions and the wall surfaces of the shock tube are used as solid boundary conditions where the gradients normal to the surface are taken zero.

## 5.4 Results and Discussion

In the present research work, the investigation on wave propagation in the open Atmosphere from the end section of the shock tube is focused mainly to observe the decay of the wave strength. Both experimentally and numerically, it is observed the wave propagation phenomena in the open Atmosphere and also measures the decaying parameters during propagation and finally a comparison test is performed between numerical results and experimental results. The numerical images are used to visualize the density contour in the flow field during the shock wave propagation in the open Atmosphere. It is observed from the density contour that the number of lines near shock front decreases gradually as increasing the distance of the shock front from the end section of the shock tube. The density contour behind the shock front shows that each line indicates the uniform density along the line and the two adjacent lines measure the density gradient of the flow field. Here there have approximately 60 contour lines considered between maximum and minimum density in the field and the density contours step is 0.01 which are shown in **Fig. 5.9 (i)-(viii)**. Similarly the density fringes are visualized numerically to investigate the wave propagation phenomena in the open Atmosphere which are shown in **Fig. 5.10 (i)-(viii)**. Many researchers were used

Double exposure holographic interferometry to visualize experimentally the density fringes for the shock wave interaction with different objects, like Wedge, Cone and Cylinder etc. A Laser beam is used to take two consequent exposures on the same photo film within few nanoseconds. Because of double shot on the same photo film, the word double exposure is used. Numata et al. [50] were conducted their experiments to observe the shock wave reflection from a skewed wedge by using the holographic interferometry. A series of experiments was carried out in order to investigate the initial transient flow in the nozzle by Saito et al. [51]. In their experiment the flow was visualized by using the double exposure laser holographic interferometry and a comparison test was conducted on density fringes of the flow field obtained by experimentally and numerically. In the present computation, the density fringes are used to explain the wave propagation characteristics and to get the complete idea on the spherical expansion of the shock front in the open Atmosphere.

Experimental investigations are conducted by developing the time measuring technique in micro-second level. Trigger-1 as shown in **Fig. 5.5**, is installed at the end section of the shock tube where $x = 0$ *cm* as shown in **Fig. 5.7**. Similarly Trigger-2 as shown in **Fig. 5.5**, is installed at a point in the free space where the distance of the point from the end section, $x = 9$ *cm* as shown in **Fig. 5.7**. Now during the wave propagation over these triggers, the device is captured frequency which is directly proportional to the travelled time of the wave from trigger-1 to trigger-2. The captured frequency is converted into travelled time by dividing the known crystal frequency. Here the known crystal frequency is 3579540 Hz, that means, 1 second is equivalent to 3579540 pulses. Similarly by installing trigger-1 and trigger-2 of the device at the points where $x = 0$ cm and x = 38.5 cm respectively, the captured frequency is measured during the wave propagation of the distance between two points and the captured frequency is then converted into travelled time of the wave.

**Figure 5.11** shows different captured frequencies measured experimentally during the wave propagation over the points in the open Atmosphere where the position of the points are, $x = 0$ *cm*, $x = 9$ *cm*, $x = 18.5$ *cm*, $x = 28.5$ *cm* and $x = 38.5$ *cm* as shown in **Fig. 5.7** and here Raksin is used as a diaphragm to generate the wave in the shock tube. The average wave speeds ($U_{av}$) are determined by the ratio of the distance between two trigger points to the wave travelled time of this distance and the wave

speed between any two trigger points is considered as the wave speed at the mid point of the two trigger points.

In case of Raksin diaphragm, **Figure 5.12** shows the average wave speed ($U_{av}$) variations in the open Atmosphere after leaving from the shock tube. Here the maximum wave speed is 326 *m/s* at position, $x = 4.5$ *cm* which is the mid point between the points, $x = 0$ *cm* and $x = 9$ *cm*. As compare to the local sound velocity, the wave speed is subsonic. So it is concluded that the rupture of the Raksin diaphragm generates subsonic wave in the open Atmosphere. It is also observed that as increasing the travel distance of the wave, the strength of the wave decreases which is shown in **Fig. 5.12.**

Similarly **Figure 5.13** shows different captured frequency measured experimentally during the wave propagation over the points in the open Atmosphere where the position of the trigger points are $x = 0$ *cm*, $x = 9$ *cm*, $x = 18.5$ *cm*, $x = 28.5$ *cm* and $x = 38.5$ *cm* as shown in **Fig. 5.7** and here X-ray film is used as a diaphragm to generate the wave in the shock tube.

In case of X-ray film diaphragm, **Figure 5.14** shows the average wave speed ($U_{av}$) variations in the open Atmosphere after leaving from the shock tube. Here the maximum wave speed is 380 *m/s* at position, $x = 4.5$ *cm* which is the mid point between the points, $x = 0$ *cm* and $x = 9$ *cm*. As compare to the local sound velocity, the wave speed is supersonic. So it is concluded that the rupture of the X-ray film diaphragm generates shock wave in the open Atmosphere. It is also observed that as increasing the travel distance of the wave, the strength of the wave decreases which is shown in **Fig. 5.14.**

In case of Raksin diaphragm, the decay of the wave propagation is determined both experimentally and numerically during the wave propagation over the trigger points in the open Atmosphere and **Figure 5.15** shows the profile of the percentage of decay at different trigger points when the wave generates by the rupture of Raksin diaphragm. It is observed that initially the percentage of decay increases obtained by experiment as compare to the numerical results. It is observed that the percentage of the decay increases as increase the distance from the end point of the shock tube. It is also observed that the decay obtained from experiment has the good agreement with the numerical result.

In case of X-ray film diaphragm, the decay of the wave propagation is determined both experimentally and numerically during the wave propagation over the trigger points in the open Atmosphere and **Figure 5.16** shows the profile of the percentage of decay at different trigger points when the wave generates by the rupture of X-ray film diaphragm. It is observed that initially the percentage of decay increases obtained by experiment as compare to the numerical results. It is observed that the percentage of the decay increases as increase the distance from the end point of the shock tube. It is also observed that the decay obtained from experiment has the good agreement with the numerical result. So it is concluded that the decay of subsonic wave and supersonic wave has the same nature during the propagation in the open atmosphere and such type of decay observe due to spherical expansion in the open Atmosphere. The decay of shock wave may differ with subsonic wave due to rapid compression and expansion happened during shock wave propagation but the percentage of decay is same after propagating far distance in the open Atmosphere.

## 5.5 Summary

In the present experimental works, a shock tube has been constructed where subsonic wave as well as shock wave has been generated by rupturing different types of diaphragm. The material properties of diaphragm are the major factor to generate shock wave in a shock tube. It is observed that the material properties like tough and brittle are the best properties in the present case. Due to unavailable expected quality of diaphragm in the market, transparent Raksin sheet and used X-ray film are used in the present experiment. It is observed that X-ray film gives the better performance as compare to Raksin for better rupture.

For measuring the wave speed in the open Atmosphere, the present time measuring technique is simple in use and accurate in measurement as compare to other complicated technique like wave visualization by High Speed Video camera. During wave propagation, the wave speed decreases as increasing the travel time in open Atmosphere. So decreasing the speed indicates that the decay of the wave strength is normal phenomena during propagation in the open Atmosphere. In the present research, both experimental and numerical techniques are applied successfully to determine the decay of the wave strength.

# List of Figures

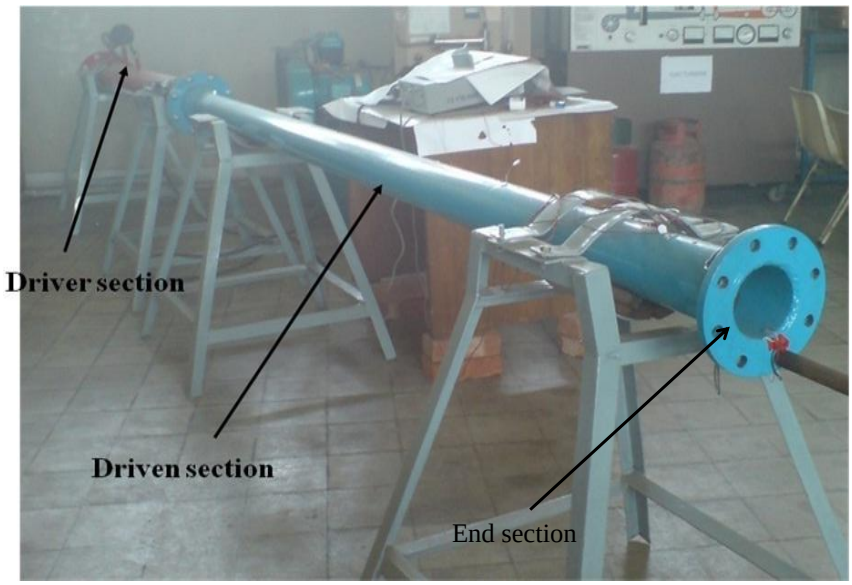


**Figure 5.1:** Photograph of Simple shock tube, constructed in Fluid Mechanics Lab on IUT where driver section and driven section are shown.

**Figure 5.2:** Photograph of Post-shocked high speed air delivered from end section of the shock tube.

**(i)**

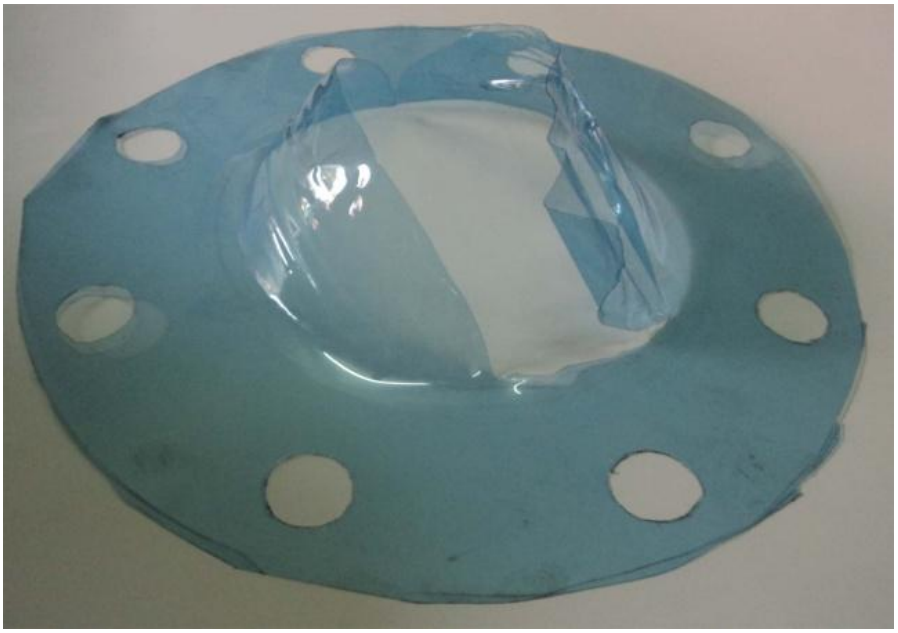

**(ii)**

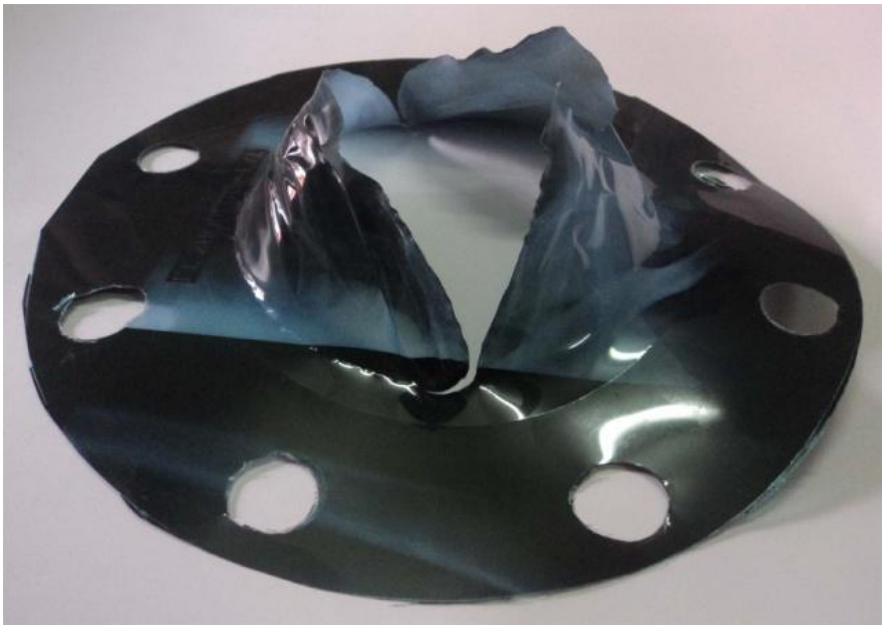

**(iii)**

**Figure 5.3:** Photograph of rupturing characteristics of different diaphragms of **(i)** Thick polythene; **(ii)** Raksin; **(iii)** X-ray film.

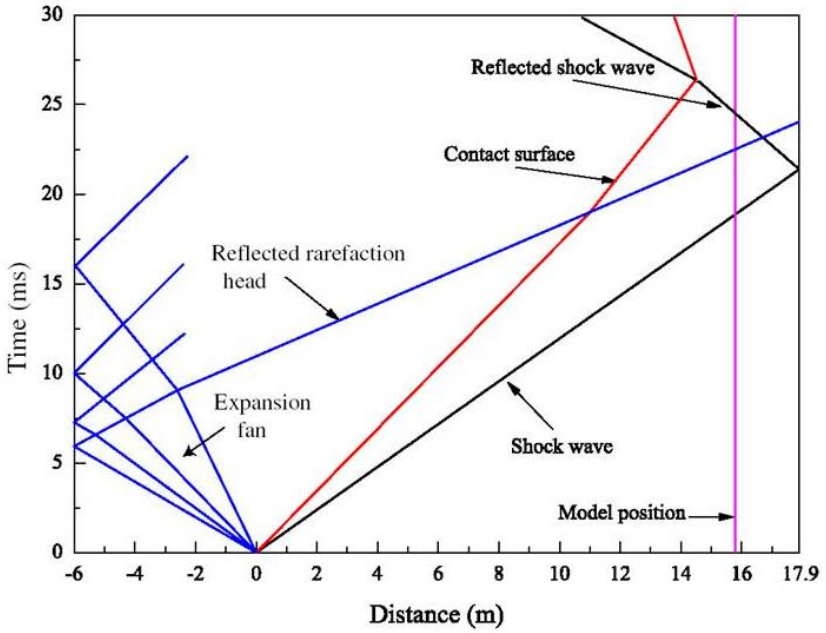


**Figure 5.4:** A typical diagram *x-t* diagram for the relative direction of the shock wave and expansion wave propagation after the rupture of diaphragm.

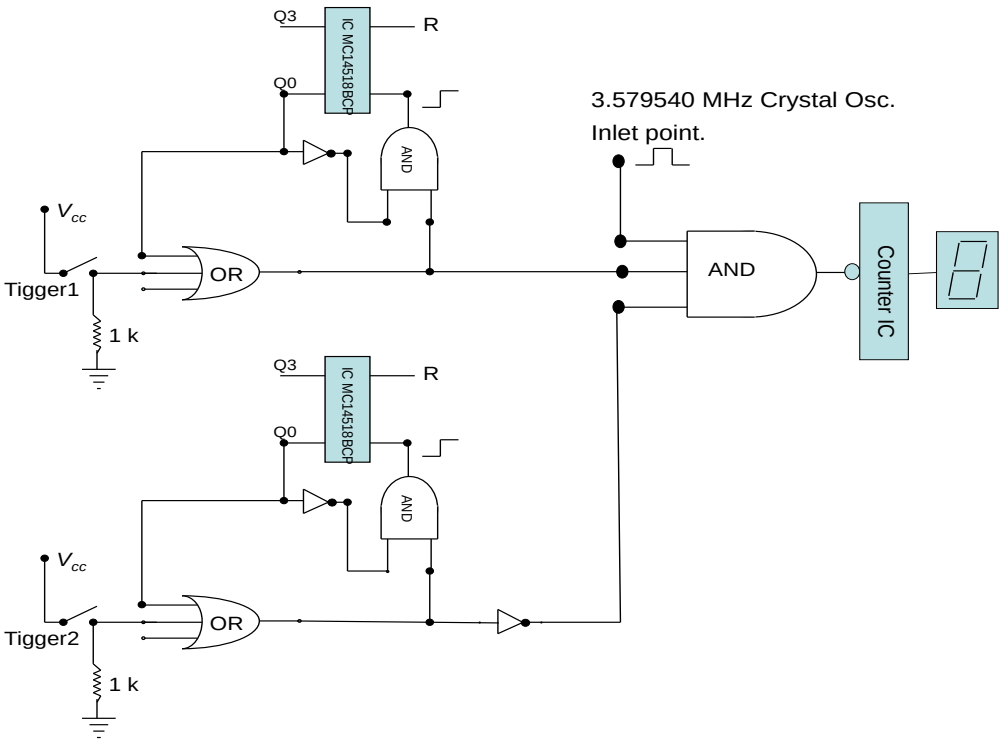


**Figure 5.5:** Circuit layout use to construct time measuring device.

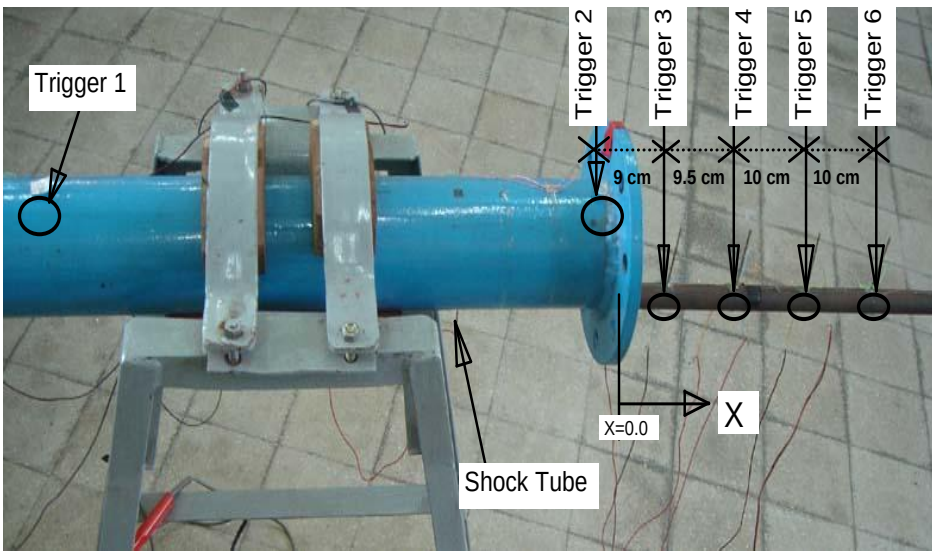


**Figure 5.6:** A schematic illustration of the horizontal shock tube where the relative distances between different trigger points are given.

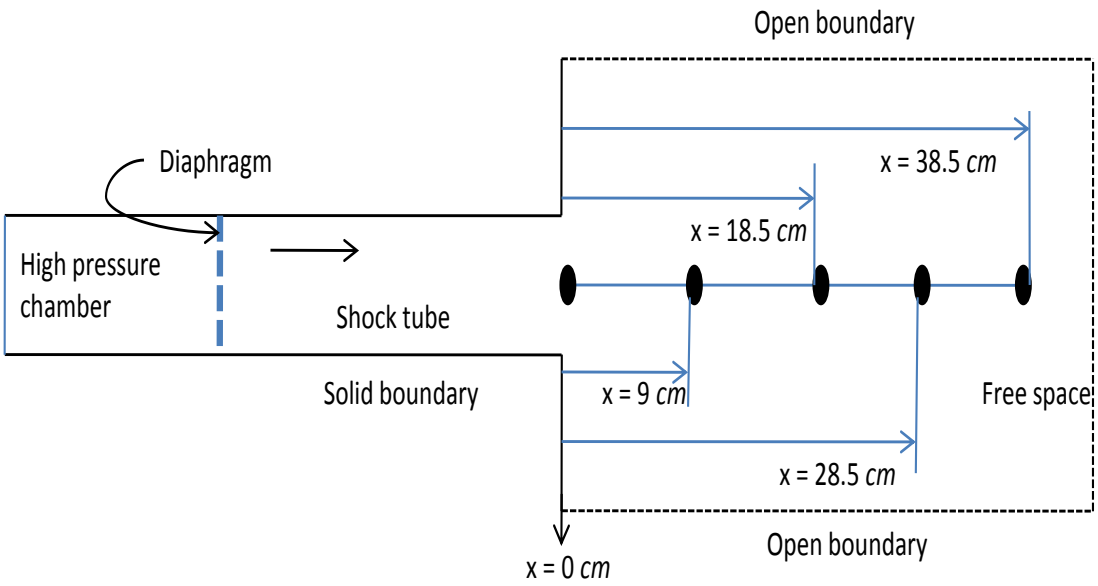


**Figure 5.7:** Schematic diagram of the Shock tube and the position of triggers.

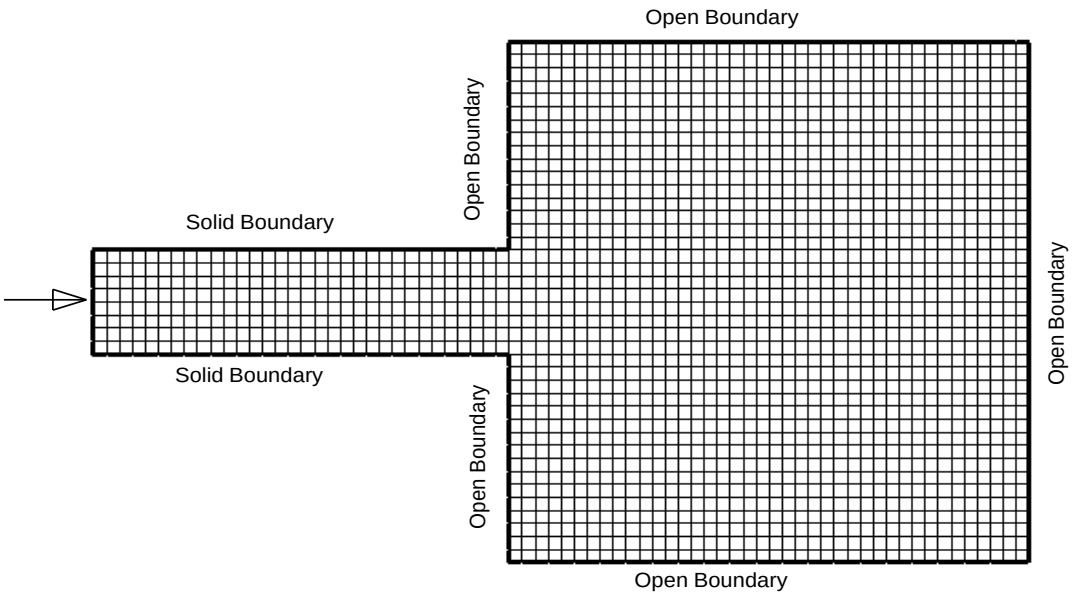


**Figure 5.8:** 2D numerical grids of the shock tube and the free space where solid boundaries are taken for shock tube and open boundaries are taken for free space.

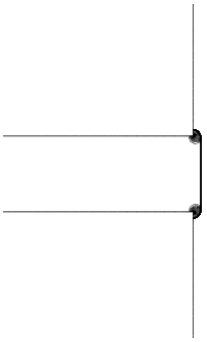

(i) Near end section of the shock tube, $x$ = 0 *cm*, density contours step 0.01.

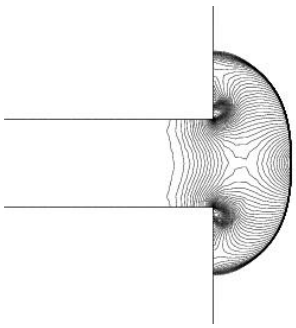

(ii) Shock front position at $x$ = 9.0 *cm*, density contours step 0.01.

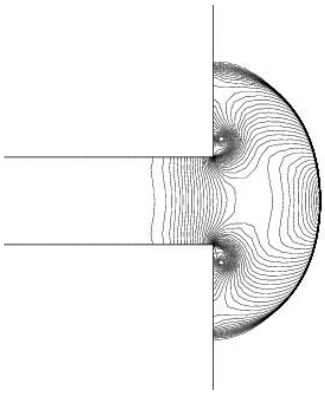

(iii) Shock front position at $x$ = 13.75 *cm*, density contours step 0.01.

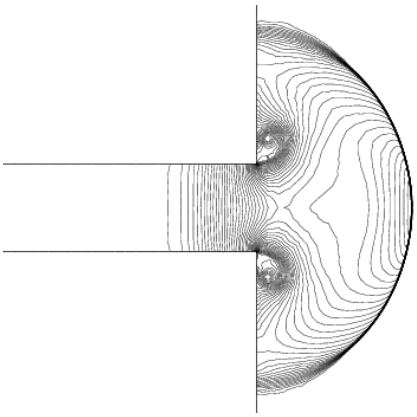

(iv) Shock front position at $x$ = 18.5 *mm*, density contours step 0.01.

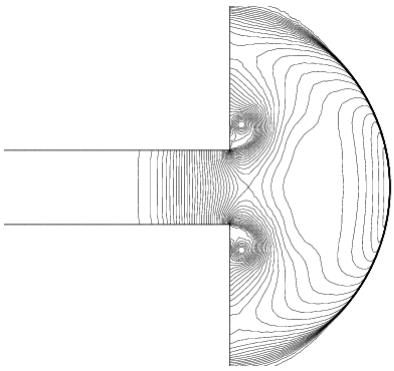

(v) Shock front position at $x$ = 23.5 *mm*, density contours step 0.01.

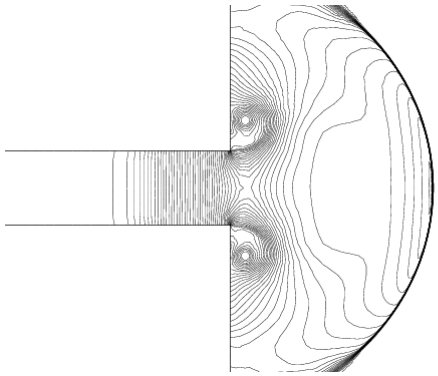

(vi) Shock front position at $x$ = 28.5 *mm*, density contours step 0.01.

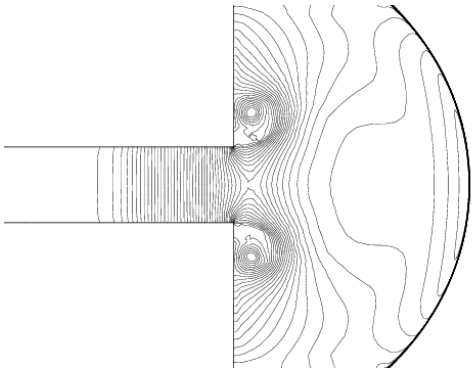

(vii) Shock front position at $x$ = 33.5 *mm*, density contour step 0.01.

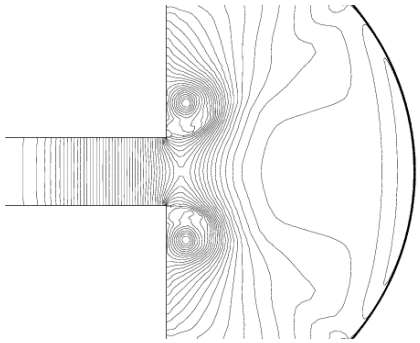

(viii) Shock front position at $x$ = 38.5 *mm*, density contour step 0.01.

**Figure 5.9:** Numerical results of the density contours at different locations of the shock front in the open Atmosphere for moderate shock propagation.

**(i)** Near end section of the shock tube, $x$ = 0.0 *cm*, density fringes step 0.1.

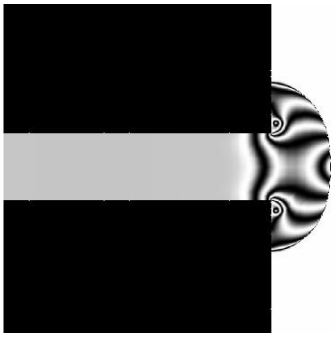

**(ii)** Shock front position at $x$ = 9.0 *cm*, density fringes step 0.1.

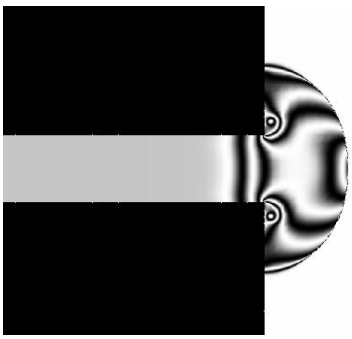

**(iii)** Shock front position at $x$ = 13.75 *cm*, density fringes step 0.1.

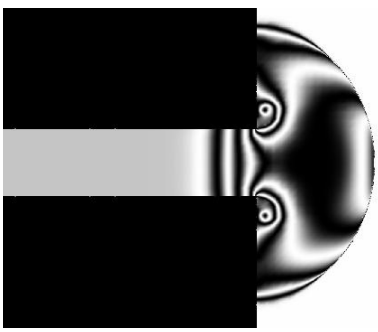

**(iv)** Shock front position at $x$ = 18.5 *cm*, density fringes step 0.1.

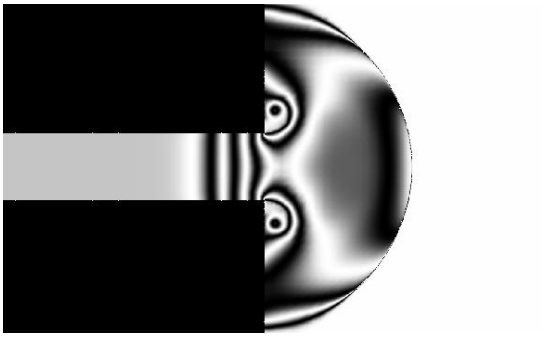

**(v)** Shock front position at $x$ = 23.5 *cm*, density fringes step 0.1.

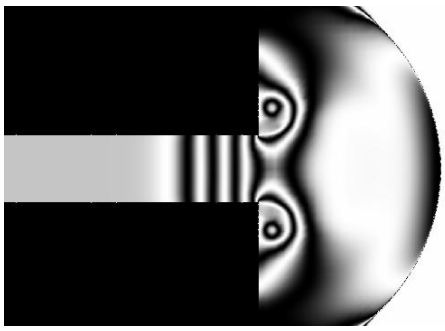

**(vi)** Shock front position at $x$ = 28.5 *cm*, density fringes step 0.1.

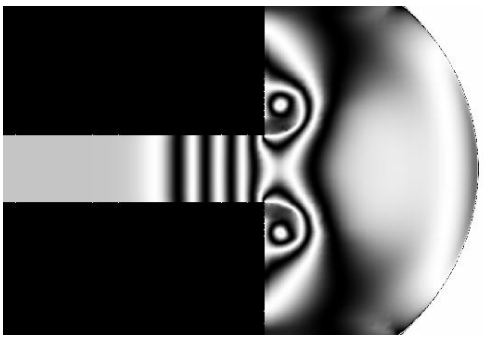

**(vii)** Shock front position at $x$ = 33.5 *cm*, density fringes step 0.1.

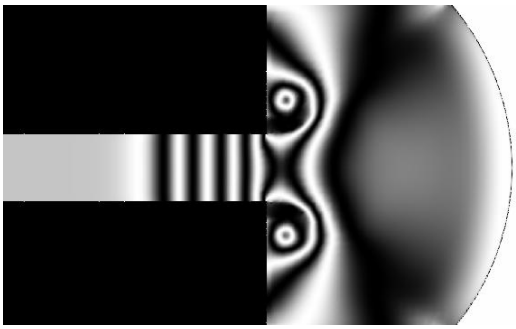

**(viii)** Shock front position at $x$ = 38.5 *cm*, density fringes step 0.1.

**Figure 5.10:** Numerical results of the density fringes at different locations of the shock front in the open Atmosphere for moderate shock propagation.

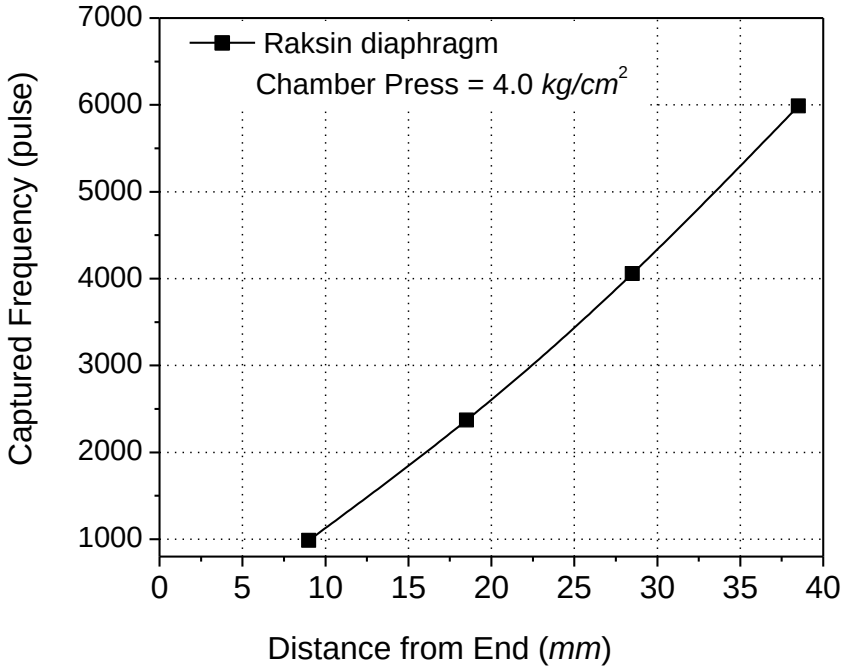


**Figure 5.11:** Captured frequency measured **e**xperimentally during the wave travels between different trigger points in the open Atmosphere (Here 1 sec = 3579540 pulses).

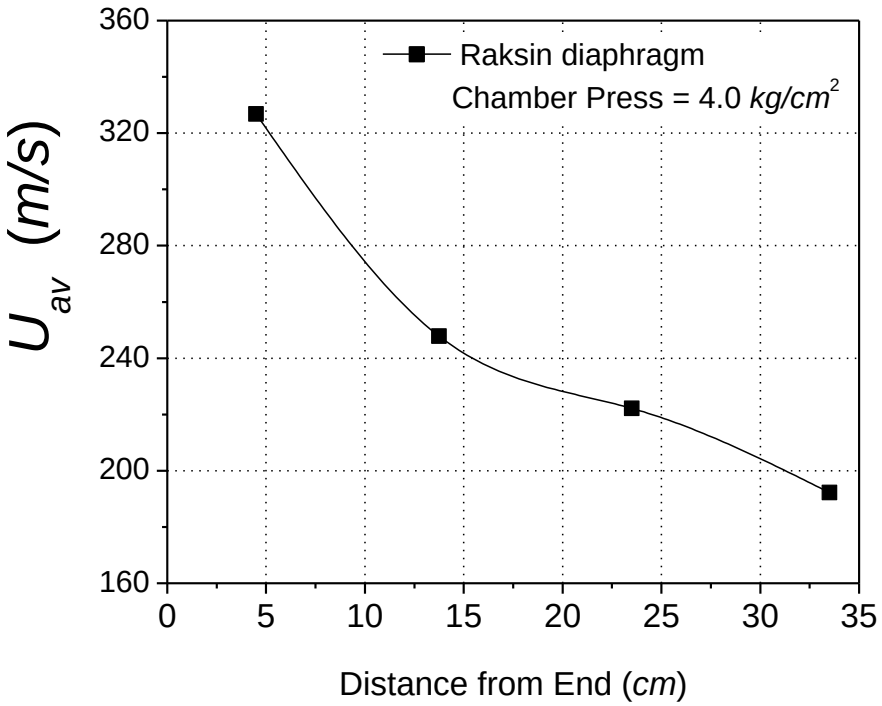


**Figure 5.12:** Experimental results of the average wave speed at different locations of the shock front in the open Atmosphere (Here rupture of Raksin diaphragm generates subsonic wave at the end of shock tube).

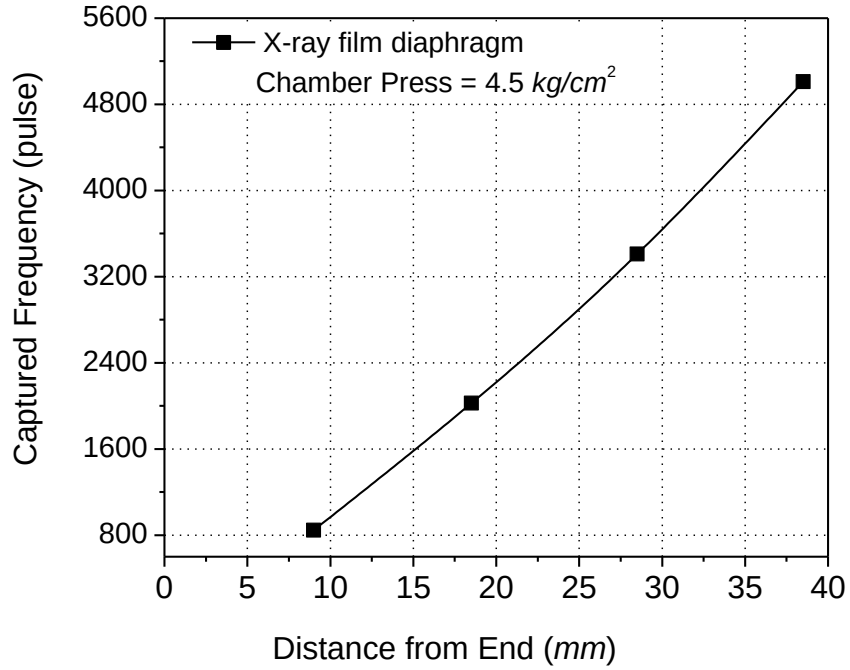


**Figure 5.13:** Captured frequency measured **e**xperimentally during the wave travels between different trigger points in the open Atmosphere (Here 1 sec = 3579540 pulses).

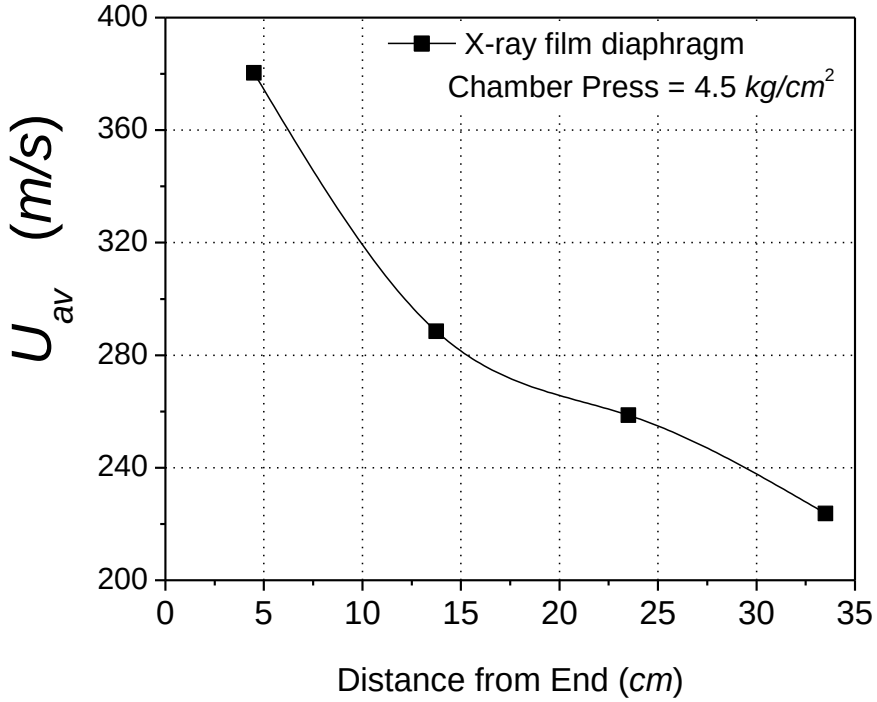


**Figure 5.14:** Experimental results of the average wave speed at different locations of the shock front in the open Atmosphere (Here rupture of X-ray film diaphragm generates supersonic wave at the end of shock tube).

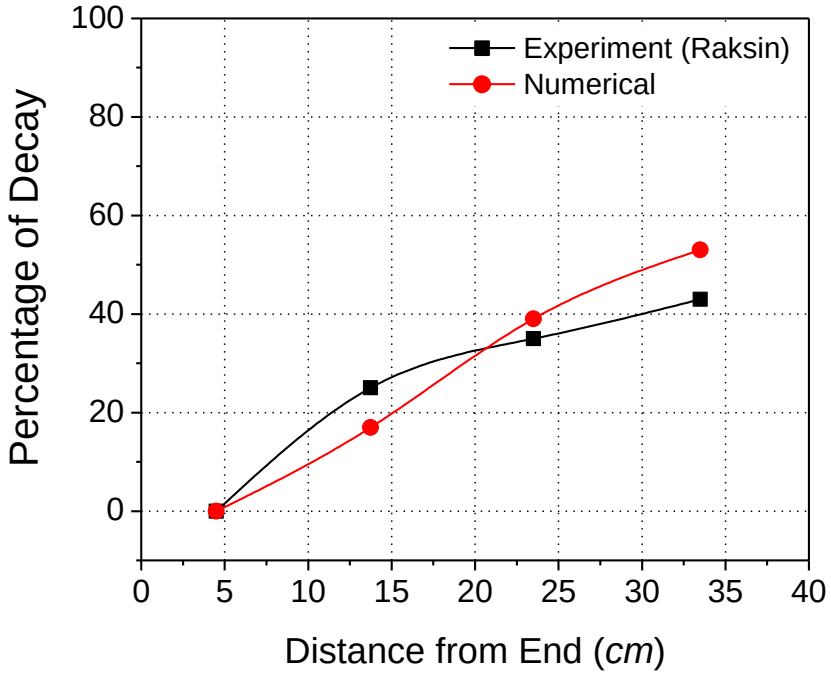


**Figure 5.15:** Comparison between Experimental results and Numerical results of the percentage of decay of the wave propagation in the open Atmosphere (Here rupture of Raksin diaphragm generates subsonic wave at the end of shock tube).

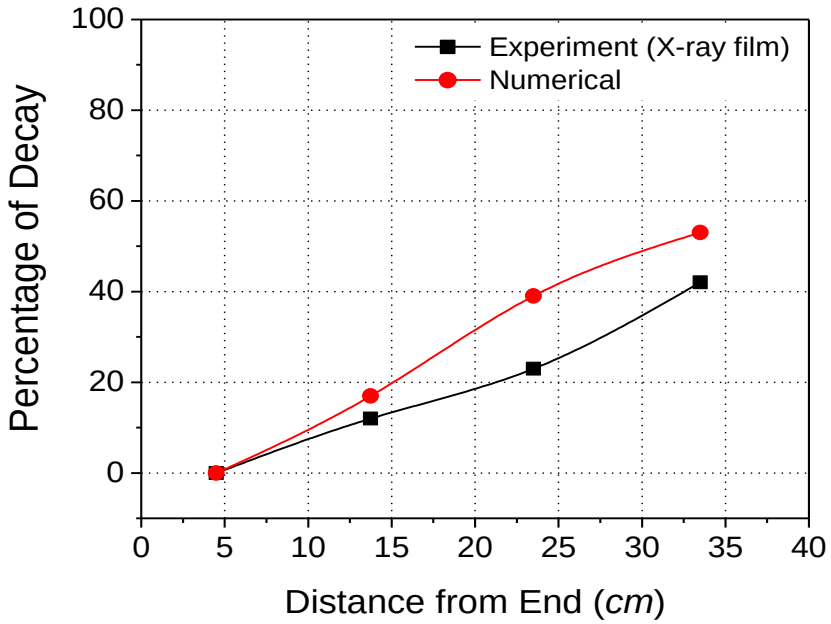


**Figure 5.16:** Comparison between Experimental results and Numerical results of the percentage of decay of the wave propagation in the open Atmosphere. (Here rupture of X-ray film diaphragm generates supersonic wave at the end of shock tube).

# Chapter 6

## Conclusions and Future Suggestions

## 6.1 Conclusions

From the present experimental and computational results, the following conclusions may be drawn:

(i) 3D numerical study is conducted to ensure the validation of the code for the present problems and the computational results are completely independent on the grid size.

(ii) The 3D numerical solutions have the advantages to know properly the expansion phenomena of the wave in space and the 3D numerical visualization indicates that the wave front during propagation in Open Atmosphere is always spherical in shape.

(iii) Euler simulation results are quite reasonable for the present research works. The advantages of the use of Euler simulation are the simple equations to solve, faster to run the numerical code and more accurate solutions due to fewer boundary conditions as compare to NS.

(iv) The Euler simulation results have been compared with the Navier-Stokes Simulation (NS) results to establish the absence of viscous effects in the present flow. The solution of the Euler equation is considered as the optimum solution where the Navier-Stokes Simulation (NS) results are used to verify the Euler simulation results.

(v) A time measuring system has been developed to measure the propagation time experimentally. It is observed that the present wave speed measuring

technique is more suitable and comparatively easy. The metal to metal triggering techniques used in the present experiment are faster and more sensitive as compare to other triggering techniques and it is possible to measure both the subsonic and supersonic wave speed by this method. So the present time measuring technique of wave propagation is one of the innovative works in this research.

(vi) Experiments on wave propagation in open Atmosphere are conducted by a simple shock tube, constructed in Fluid Mechanics Laboratory, IUT. It is observed that wave strength generated by this shock tube depends on the diaphragm materials as well as the chamber pressure withstand by the diaphragm. Different types of diaphragm are used to observe the rupturing characteristics of the diaphragm and it is concluded that the diaphragms with the properties of tough and brittle are suitable to generate the shock wave in the driven section of the shock tube properly. Brittle typed diaphragms are making large open area after rupture as a result create high pressure gradient in the fluid flows of the driven section which finally generate shock wave in the shock tube.

(vii) After leaving the shock tube, the decay of the shock wave propagation in the open Atmosphere is observed and the estimation of the decaying rate has been measured by travel time along the axis of the shock tube. After travelling a short distance in open Atmosphere, the shock wave with supersonic speed changes to subsonic wave which behaviors differ from shock wave. So construction of the shock tube is the important works in the present experiments to conduct research on both supersonic and subsonic wave.

(viii) By visualizing the shock wave propagation in open atmosphere, it is observed that the wave strength decreases gradually after the wave propagation in the free atmosphere from the outlet of the shock tube end face. The numerical results of the density fringes indicate the expansion wave propagation towards the shock tube outlet and it is observed that wave front is spherical in shape.

## 6.2 Future Suggestions

Future suggestions of this research are highly important in both practical fields and research fields which are drawn as follows:

(i) In practical fields, it is necessary to know the interaction effects with objects in free space. In the atmosphere, shock waves can be heard directly as loud bangs. They can transmit energy from the place of generation to distant areas and may cause window panes to shatter. Like an ordinary wave, shock wave carries energy and can propagate through a medium (solid, liquid, gas or plasma) or in some cases in the absence of a material medium, through a field such as the electromagnetic field. The field of shock waves in condensed materials (solids or liquids) has grown into an important interdisciplinary area of research involving condensed matter physics, geophysics, materials science, applied mechanics, and chemical physics. The nonlinear aspect of shock waves is an important area of applied mathematics. So better research, in future needs more financial supports and sophisticated instruments to measure the shock wave interaction effects with objects in free space.

(ii) In the present research, experimental photographs are the important topics to explain shock wave phenomena in open atmosphere. Widely used qualitative and semi-quantitative optical flow diagnostics are shadowgraph, schlieren, and interferometry. So using above techniques, the flow visualization can be obtained experimentally and can be able to compare with numerical images which is later used to validate the numerical code.

(iii)It may suggest to conduct more research on different diaphragms and to determine their ruptured characteristics

# REFERENCES


[1] Doig, G.C., Barber, T.J., Leonardi, E., Neely, J., Kleine, H., 2008. Methods for investigating supersonic ground effect in a blowdown wind tunnel, Shock Waves, 18: 155-15.

[2] Kobiera, A., Szymczyk, J., Wola'nski, P., Kuhl, A., 2009. Study of the shock-induced acceleration of hexane droplets, Shock Waves, 18: 475-85.

[3] Pianthong, K., Zakrzewski, S., Behnia, M., Milton, B.E., 2002**.** Supersonic liquid jets: Their generation and shock wave characteristics, Shock Waves, 11: 457-66.

[4] Ribner, H. S. 1953, " Convection of a pattern of vorticity through a shock wave." NACA TN-2864, 1953.

[5] Ribner, H. S. 1954, " Shock-turbulence interaction and the generation of noise." NACA TN-3255, 1954.

[6] Ribner, H. S. 1969, " Acoustic energy flux from shock-turbulence interaction." *Journal of Fluid Mechanics* **Vol. 35**, 1969, pp. 299-310.

[7] Kovasznay, L. S. G. 1953, "Turbulence in supersonic flow." *J. Aero. Sci.* **Vol. 20**, pp. 657-682.

[8] Lighthill, M. J. 1953, "On the energy scattered from the interaction of turbulence with sound or shock wave." Proc. Camb. Phil. Soc. 49, 531-551.

[9] Moore, F. K. 1953, "Unsteady oblique interaction of a shock wave with a plane disturbances." NACA TN-2879, 1953.

[10] Kerrebrock, J. L. 1956, " The interaction of flow discontinuities with small disturbances in a compressible fluid." Ph.D. thesis, California Institute of Technology.

[11] Ribner, H. S. 1987, " Spectra of noise and amplified turbulence emanating from shock-turbulence interaction." *AIAA J.* **Vol. 25,** 436-442.

[12] Anyiwo, J. C. & Bushnell, D. M. 1982, "Turbulence amplification in shock-wave boundary-layer interaction." *AIAA J.* **Vol. 20,** 893-899.

[13] Sekundov, A. N. 1974, "Supersonic flow turbulence and interaction with a shock wave." Izv. Akad. Nauk SSR Mekh. Zhidk. Gaza, March-April 1974.

[14] Donsanjh, D. S. & Weeks, T. M. 1964, "Interaction of a starting vortex as well as Karman vortex streets with traveling shock wave." AIAA paper No. 64-425, 1964.

[15] Chu, B. T. & Kovasznay, L. S. G. 1957, "Non-linear interactions in a viscous heat-conducting compressible flow." *Journal of Fluid Mechanics* **Vol. 3**, 1957, pp. 494.

[16] Hesselink, L , Sturtevant, B. 1988; " Propagation of weak shocks through a random medium." *J. Fluid Mechanics* 196: 513-553.

[17] Richtmyer, R. D. 1960, Commun. Pure Appl. Math. **Vol. 13**, 297 (1960).

[18] Meshkov, E. E. 1969, Izv. Akad. Nauk SSSR Mekh. Zhidk. Gaza **Vol. 4**, 151 (1969).

[19] Doig, G.C., Barber, T.J., Leonardi, E., Neely, J., Kleine, H., 2008. Methods for investigating supersonic ground effect in a blowdown wind tunnel, Shock Waves, 18: 155-15.

[20] Craig JE (1977) Shock waves in open ended ducts with complex geometry.Ph D Aeronautics. California Institute of Technology,Pasdene CA,USA.

[21] Szumowski AP (1971) Attenuation of Shockwaves along a perforated tube. In: Stollery JL, Gaydon AG, Wen PR (eds) Shock Tube Research, Proc 8th Int Symp Shock Tubes. Chapman & Hall 14.

[22] Sugimoto N (1992) Propagation of nonlinear acoustic waves in a tunnel with an array of Helmholtz resonators. J Fluid Mech 244: 55-78.

[23] Onodera H, Takayama K (1992) An analysis of shock wave propagation over perforated wall and its discharge coefficient. Trans Jpn Soc Mech Eng B (in Japanese). 58:1408.

[24] Takayama K, Sasoh A, Onodera O, Kaneko R, Matsui Y (1995) Experimental investigation on tunnel sonic boom. Shock Waves 5:127{138}

[25] Ben-Dor, G., Takayama, K.: The phenomena of shock wave reflection—a review of unsolved problems and future research needs. Shock Waves **2**, 211–223 (1992)

[26] Timofeev, E., Voinovich, P., Saito, T., Takayama, K.: Three dimentional unsteady reflection of a planar shock wave from an inclined cylinder. In: Proceedings of International Symposium on Interdisciplinary Shock Wave Research, ISISW, Matsushima Japan, pp. 498–517 (2004). This paper is available in ISWI Proceedings Archive 2007.

[27] Markstein, G.H.: Nonsteady Flame Propagations. Mac-Millan, New York (1964).

[28] Batley, G.A., McIntosh, A.C., Brindley, J., Falle, S.A.E.G.: (1994) A numerical study of the vorticity field generated by the baroclinic effect due to the propagation of a planar pressure wave through a cylindrical premixed laminar flame. J. Fluid Mech. 279, 217–237. doi:10.1017/S0022112094003897

[29] Khokhlov, A.M., Oran, E.S., Chtchelkanova, A.Y., Wheeler, J.C.: (1999) Interaction of a shock with a sinusoidally perturbed flame. Combust Flame 117, 99–116.

[30] Ju, Y., Shimano, A., Inoue, O.: Vorticity generation and flame distortion induced by shock–flame interaction. Proc. Combust Inst. 27, 735–741 (1998)

[31] Gelfand, B.E., Khomik, S.V., Bartenev, A.M., Medvedev, S.P., Groing, H., Olivier, H.: (2000) Detonation and deflagration at the focusing of shockwaves in combustible gaseous mixture. Shock Waves. 10, 197–204. doi:10.1007/s001930050007

[32] Bartenev, A.M., Khomik, S.V., Gelfand, B.E., Gronig, H., Olivier, H.: (2000) Effect of reflection type on detonation initiation at shock-wave focusing. Shock Waves 10, 205–215.

[33] Shinsuke Udagawa·Walter Garen ·Bernd Meyerer. Motion analysis of a diaphragmless driver section for a narrow channel shock tube. Shock Waves (2008) 18:345–351 DOI 10.1007/s00193-008-0171-9

[34] Abdellah Hadjadj · Marcello Onofri . Nozzle flow separation. Shock Waves (2009) 19:163–169. DOI 10.1007/s00193-009-0209-7

[35] Zeitoun, D.E., Burtschel, Y.: Navier–stokes computations in micro shock tubes. Shock Waves 15, 241–246 (2006)

[36] Trimpi, R.L., Cohen, N.B.: A theory for predicting the flow of real gases in shock tubes with experimental verification. Technical Report NACA 3375, National Advisory Committee for Aeronautics 1955)

[37] Emrich, R.J., Wheeler, D.B.:Wall effects in shock tube flow. Phys. Fluids 1, 14–23 (1958)

[38] Mirels, H.: Attenuation in a shock tube due to unsteady-boundary layer action. Technical Report TN 1333, National Advisory Committee for Aeronautics (1957).

[39] Roshko, A.: On flow duration in low-pressure shock tubes. Phys. Fluids 3(6), 835–842 (1960).

[40] Mirels, H.: Correlation fomulas for laminar shock tube boundary layer. Phys. Fluids 9(7), 1265–1272 (1966).

[41] Chen, C.J., Emrich, R.J.: Ivestigation of the shock-tube boundary layer by a tracer method. Phys. Fluids 6(1), 1–9 (1963).

[42] Sun, M., Ogawa, T., Takayama, K.: Shock propagation in narrow channels. In: Proceedings of the 23nd International Symposium on Shock Waves, vol. 2227. Forth worth, Texas (2002).

[43] Toro EF (1999) Riemann solvers and numerical methods for fluid dynamics. 2nd edition, Springer. Berlin, Heidelberg, New York.

[44] Ben-Dor, G.: Shock Wave Reflection Phenomena, 2nd edn. Springer, New York (2007).

[45] Yanchao Shi, Hong Hao and Zhong-Xian Li (2007) Numerical simulation of blast wave interaction with structure columns. Shock Waves Journal, Vol. 17: 113-33.

[46] O. Igra, L. Wang, J. Falcovitz and W. Heilig (1998) Shock wave propagation in a branched duct. Shock Waves Journal, Vol. 8: 375-81.

[47] Lee S, Lele SK, Moin P (1993) Direct numerical simulation of isotropic turbulence interacting with a weak shock wave. Journal of Fluid Mechanics 251: 533-62

[48] Rotman D (1991) Shock wave effects on a turbulent flows. Phys. Fluids A3: 1792-806

[49] Jinnah MA (2005) Numerical and experimental study of Shock/Turbulent flow interaction. Doctor Thesis, Tohoku University.

[50] Numata D., Ohtani K. and Takayama K. (2009) Diffuse holographic interferometric observation of shock wave reflection from a skewed wedge, Shock Waves, 19: 103-112.

[51] Saito T., Takayama K. (1999) Numerical simulations of nozzle starting process, Shock Waves, 9: 73-79.